

UNIVERSITÉ DE MONTRÉAL

AUTOMATIC SPATIOTEMPORAL ANALYSIS OF CARDIAC IMAGE SERIES

MITCHEL BENOVOY
INSTITUT DE GÉNIE BIOMÉDICAL
ÉCOLE POLYTECHNIQUE DE MONTRÉAL

THÈSE PRÉSENTÉE EN VUE DE L'OBTENTION
DU DIPLÔME DE PHILOSOPHIÆ DOCTOR
(GÉNIE BIOMÉDICAL)
AOÛT 2016

UNIVERSITÉ DE MONTRÉAL

ÉCOLE POLYTECHNIQUE DE MONTRÉAL

Cette thèse intitulée :

AUTOMATIC SPATIOTEMPORAL ANALYSIS OF CARDIAC IMAGE SERIES

présentée par : BENOVOY Mitchel

en vue de l'obtention du diplôme de : Philosophiæ Doctor

a été dûment acceptée par le jury d'examen constitué de :

M. SAVARD Pierre, Ph. D., président

Mme CHERIET Farida, Ph. D., membre et directrice de recherche

M. DAHDAH Nagib S., M.D., membre et codirecteur de recherche

M. KADEM Lyes, Ph. D., membre

M. MARTUCCI Giuseppe, M.D., membre externe

DEDICATION

À Juliette et Laurence

ACKNOWLEDGEMENTS

To my co-supervisors, Prof. Farida Cheriet and Dr. Nagib Dahdah, I owe my sincere gratitude for your guidance on both professional and personal levels. Your abiding willingness to see me succeed instilled a deep sense of confidence and positivity in my work. Both your open-door attitudes to meet, brainstorm, and debate have made this doctorate exceedingly intellectually pleasant.

To Dr. Li-Yueh Hsu and Dr. Andrew Arai, who welcomed me to their research group at the National Institutes of Health. Their guidance, resources, and ideas led me to develop a significant portion of the work presented in this thesis.

To my dear Laurence, who has endured much too long of me being a graduate student, but who's always been there to support me.

To Jordan and Aden, my dear friends always there to remind to breath.

To my labmates, who are always willing to engage in constructive discussions. A special thanks to Philippe Debanné who's been fantastically resourceful.

To my brothers Jason and David, who have been, well, brothers.

Finally, to my parents, to whom I owe everything.

RÉSUMÉ

À ce jour, les maladies cardiovasculaires demeurent au premier rang des principales causes de décès en Amérique du Nord. Chez l'adulte et au sein de populations de plus en plus jeunes, la soi-disant épidémie d'obésité entraînée par certaines habitudes de vie tels que la mauvaise alimentation, le manque d'exercice et le tabagisme est lourde de conséquences pour les personnes affectées, mais aussi sur le système de santé. La principale cause de morbidité et de mortalité chez ces patients est l'athérosclérose, une accumulation de plaque à l'intérieur des vaisseaux sanguins à hautes pressions telles que les artères coronaires. Les lésions athérosclérotiques peuvent entraîner l'ischémie en bloquant la circulation sanguine et/ou en provoquant une thrombose. Cela mène souvent à de graves conséquences telles qu'un infarctus. Outre les problèmes liés à la sténose, les parois artérielles des régions criblées de plaque augmentent la rigidité des parois vasculaires, ce qui peut aggraver la condition du patient. Dans la population pédiatrique, la pathologie cardiovasculaire acquise la plus fréquente est la maladie de Kawasaki. Il s'agit d'une vasculite aigüe pouvant affecter l'intégrité structurale des parois des artères coronaires et mener à la formation d'anévrismes. Dans certains cas, ceux-ci entravent l'hémodynamie artérielle en engendrant une perfusion myocardique insuffisante et en activant la formation de thromboses.

Le diagnostic de ces deux maladies coronariennes sont traditionnellement effectués à l'aide d'angiographies par fluoroscopie. Pendant ces examens paracliniques, plusieurs centaines de projections radiographiques sont acquises en séries suite à l'infusion artérielle d'un agent de contraste. Ces images révèlent la lumière des vaisseaux sanguins et la présence de lésions potentiellement pathologiques, s'il y a lieu. Parce que les séries acquises contiennent de l'information très dynamique en termes de mouvement du patient volontaire et involontaire (ex. battements cardiaques, respiration et déplacement d'organes), le clinicien base généralement son interprétation sur une seule image angiographique où des mesures géométriques sont effectuées manuellement ou semi-automatiquement par un technicien en radiologie. Bien que l'angiographie par fluoroscopie soit fréquemment utilisé partout dans le monde et souvent considéré comme l'outil de diagnostic "gold-standard" pour de nombreuses maladies vasculaires, la nature bidimensionnelle de cette modalité d'imagerie est malheureusement très limitante en termes de spécification géométrique des différentes régions pathologiques. En effet, la structure tridimensionnelle des sténoses et des anévrismes ne peut pas être pleinement appréciée en 2D car les caractéristiques observées varient selon la configuration angulaire de l'imageur. De plus, la présence de lésions affectant les artères coronaires peut ne pas refléter la véritable santé du myocarde, car des mécanismes compensatoires naturels (ex. vaisseaux

collatéraux) peuvent estomper la nécessité d’une intervention. Dans cette optique, l’imagerie de perfusion cardiaque par résonance magnétique attire de plus en plus l’attention. Comme avantage, elle offre une évaluation directe de la viabilité des tissus myocardiques à la suite d’un infarctus ou d’une maladie coronarienne soupçonnée. Ce type de modalité est, cependant, susceptible au mouvement, au même titre que l’angiographie par fluoroscopie. Ce problème oblige les cliniciens à faire une intervention manuelle laborieuse pour aligner une à une les structures anatomiques dans les séquences d’images, entravant ainsi l’automatisation des mesures quantitatives des signaux de perfusion.

Les principaux problèmes liés à l’utilisation clinique de ces deux modalités, soit l’angiographie par fluoroscopie et l’imagerie de perfusion par résonance magnétique, en termes d’extraction efficace et objective d’indices cliniques sont liés à la nature spatiotemporelle des données qu’ils produisent. Pour les angiographies, les calculs automatiques et rapides sur les artères coronaires sont possible si elles sont segmentées de manière précise et autonome. Toutefois, cette étape a été historiquement difficile, car la plupart des approches ont abordé la segmentation sur une image de la série angiographique très dynamique et les régions pathologiques étaient rarement considérées. Limiter le domaine de l’analyse sur seule image est d’autant plus problématique, car certaines composantes dynamiques qui peuvent détenir des indices diagnostiques potentiellement intéressants liés à la santé des vaisseaux sont ignorés. Dans l’imagerie de perfusion, les structures anatomiques subissant des déformations non rigides doivent être mises en correspondance d’une image à l’autre pour permettre des estimations de perfusion à la résolution du pixel. En outre, les séries auxiliaires sont de plus en plus utilisées pour améliorer la quantification de la perfusion, mais leur grande variabilité d’apparence et leur temps d’acquisition non-synchrones aux séries standards de perfusions engendre un effort manuel considérable afin d’aligner les régions anatomiques correspondantes.

Ces problématiques conduisent à la principale question de recherche de cette thèse : La gestion de l’information spatiotemporelle présente dans l’imagerie de perfusion et l’angiographie fluoroscopique peut-elle améliorer l’extraction d’indices clinique précis, objectifs et améliorer l’ergonomie opérationnelle ?

Les principaux objectifs du travail présenté dans cette thèse sont la conception de stratégies translationnelles d’atténuation sélective et d’intégration des composantes spatiotemporelles retrouvées dans les séries d’images pour faire face aux problèmes inhérents des modalités mentionnées ci-dessus. Dans l’imagerie de perfusion cardiaque par résonance magnétique, un système de compensation de mouvement a été développé en utilisant une formulation du flux optique pour recaller automatiquement les images à une géométrie anatomique commune. Cette approche jumelle les points de correspondances “histograms of oriented gradients” au

flux optique variationnel pour atteindre une précision sous-pixel de l'estimation des petites et grandes déformations non rigides. Une attention particulière a été accordée pour s'assurer de la fidélité des signaux de perfusion et d'une efficacité opérationnelle en développant une stratégie de calcul parallèle. Ce système a également été utilisé pour recalibrer les séries auxiliaires avec les images de perfusion en utilisant un paradigme de réduction à l'unimodalité qui encode principalement des informations structurelles et apparie les distributions photométriques. L'approche de compensation de mouvement a ensuite été translatée pour les séries angiographiques, où l'alignement uniforme des artères coronaires a permis leur segmentation précise en couplant un traitement par filtres anisotropiques Gaussien avec le suivi de la propagation de l'agent de contraste dans les vaisseaux. La robustesse au niveau des segments pathologiques tels que les anévrismes ou des zones d'ectasie a été réalisée avec une routine de correction automatique. Enfin, la performance quantitative et qualitative du résultat de segmentation a conduit à l'élaboration d'un outil d'évaluation de la distensibilité artérielle en suivant les parois des vaisseaux sur un cycle cardiaque pour extraire leurs variations de diamètre. Des indices relatifs à la rigidité apparente de la paroi ont ensuite été proposées. Cette approche a été testée dans deux études cliniques pour évaluer sa capacité à détecter et à stratifier la rigidité artérielle apparente dans une cohorte de patients atteints de la maladie de Kawasaki par rapport à leur historique anévrisimal ou des lésions des parois détectées avec la tomographie par cohérence optique intravasculaire.

L'approche de compensation de mouvement a été évaluée sur une cohorte de 291 patients adultes ayant subi une imagerie de perfusion cardiaque par résonance magnétique avec une large gamme de paramètres d'acquisition. Le système proposé a montré une amélioration des résultats d'alignement anatomiques par rapport à une solution commerciale courante. Notamment, l'approche a été en mesure de compenser le mouvement pour les patients qui ont été acquis dans un paradigme de respiration libre ou ceux qui avaient échoué l'apnée. En outre, les enregistrements auxiliaires comme les "arterial input functions" et de densité de protons ont été correctement compensés pour le mouvement et ces derniers ont été correctement alignés aux séries de perfusion. L'application de ce système aux séries fluoroscopiques a été testée sur une population de 31 patients pédiatriques. Elle a été bénéfique, car le suivi de l'écoulement de l'agent de contraste à travers l'arbre artériel après compensation de mouvement a aidé la segmentation des vaisseaux. Toutes les régions pathologiques ont été segmentées avec succès et une routine automatique d'extraction de calibre a été utilisée pour démontrer la fidélité géométrique avec des systèmes commerciaux manuels et semi-automatiques. Enfin, ces résultats de segmentation de haute qualité ont été utilisés pour initialiser l'outil d'évaluation de la distensibilité. La première étude clinique a démontré une distensibilité détériorée chez 13 patients Kawasaki par rapport à cinq sujets sains. L'outil a aussi été en mesure de

stratifier les patients avec et sans antécédents de lésions anévrismales. Dans une deuxième étude clinique, des corrélations significatives ont été trouvées entre le nombre de lésions de la paroi artérielle et les mesures de distensibilité calculées sur une cohorte élargie de 27 patients atteints de maladie de Kawasaki. Dans l'ensemble, une tendance à une rigidité accrue évaluée à partir des angiographies a été proportionnelle au nombre de lésions observées de manière invasive.

En conclusion, cette thèse présente une gestion spatiotemporelle en termes de compensation de mouvement pour les séries de perfusion (IRM) et fluoroscopiques (angiographie) et en termes d'intégration en suivant le bolus et les parois des vaisseaux dans les angiographies. Ces développements bénéficient de plus d'objectivité et d'efficacité d'extraction métrique en permettant l'automatisation de la quantification de la perfusion et les calculs statiques et dynamiques des diamètres des vaisseaux. En termes de développement futur, l'évolution naturelle du système de segmentation est l'intégration de multiples vues angiographiques autour du patient pour effectuer la reconstruction 3D du réseau artériel. Suite à cela, les informations du suivi du bolus utilisé pour la segmentation 2D peuvent alors être utilisées pour initialiser et moduler des simulations de la dynamique des fluides à l'intérieur des artères coronaires reconstruites pour fournir une évaluation plus précise fondée largement sur les données du patient. Ces possibilités sont particulièrement intéressantes lorsque des lésions anévrismales complexes sont présentes où certaines conditions rhéologiques peuvent favoriser le développement de thromboses ou d'autres conditions sérieuses. Quant à l'outil d'évaluation de la distensibilité, sa performance encourageante justifie son investigation élargie aux populations d'athérosclérose adultes, où il pourrait aider à élucider les régions de plaque ambiguës ou bien pour étudier l'état des vaisseaux suite à une intervention telle qu'une angioplastie ou un l'installation d'une endoprothèse (stent) biorésorbable.

ABSTRACT

Cardiovascular disease continues to be the leading cause of death in North America. In adult and, alarmingly, ever younger populations, the so-called *obesity epidemic* largely driven by lifestyle factors that include poor diet, lack of exercise and smoking, incurs enormous stresses on the healthcare system. The primary cause of serious morbidity and mortality for these patients is atherosclerosis, the build up of plaque inside high pressure vessels like the coronary arteries. These lesions can lead to ischemic disease and may progress to precarious blood flow blockage or thrombosis, often with infarction or other severe consequences. Besides the stenosis-related outcomes, the arterial walls of plaque-ridden regions manifest increased stiffness, which may exacerbate negative patient prognosis. In pediatric populations, the most prevalent acquired cardiovascular pathology is Kawasaki disease. This acute vasculitis may affect the structural integrity of coronary artery walls and progress to aneurysmal lesions. These can hinder the blood flow's hemodynamics, leading to inadequate downstream perfusion, and may activate thrombus formation which may lead to precarious prognosis.

Diagnosing these two prominent coronary artery diseases is traditionally performed using fluoroscopic angiography. Several hundred serial x-ray projections are acquired during selective arterial infusion of a radiodense contrast agent, which reveals the vessels' luminal area and possible pathological lesions. The acquired series contain highly dynamic information on voluntary and involuntary patient movement: respiration, organ displacement and heartbeat, for example. Current clinical analysis is largely limited to a single angiographic image where geometrical measures will be performed manually or semi-automatically by a radiological technician. Although widely used around the world and generally considered the gold-standard diagnosis tool for many vascular diseases, the two-dimensional nature of this imaging modality is limiting in terms of specifying the geometry of various pathological regions. Indeed, the 3D structures of stenotic or aneurysmal lesions may not be fully appreciated in 2D because their observable features are dependent on the angular configuration of the imaging gantry. Furthermore, the presence of lesions in the coronary arteries may not reflect the true health of the myocardium, as natural compensatory mechanisms may obviate the need for further intervention. In light of this, cardiac magnetic resonance perfusion imaging is increasingly gaining attention and clinical implementation, as it offers a direct assessment of myocardial tissue viability following infarction or suspected coronary artery disease. This type of modality is plagued, however, by motion similar to that present in fluoroscopic imaging. This issue predisposes clinicians to laborious manual intervention in order to align anatomical structures in sequential perfusion frames, thus hindering automation of

quantitative perfusion signal measurements.

The main issues pertinent to the operational efficiency and metric extraction of these two modalities in clinical use are related to the spatiotemporal nature of the data they produce. In fluoroscopic imaging, automatic and fast metric computations from the coronary arteries are feasible, given accurate and autonomous segmentation of the vessels. However, this step has historically been challenging because most past approaches tackled the segmentation on a single frame of the highly dynamic angiographic series and pathological regions were seldom accounted for. Restricting the analysis domain to a single frame is also problematic because some dynamic components that may hold potentially valuable diagnostic clues related to the health of the vessels are discarded. To allow pixel-wise perfusion estimates in cardiac magnetic resonance imaging, anatomical structures undergoing complex nonrigid deformations must be put into strict correspondence from frame to frame. In addition, the registration of auxiliary series are increasingly used to enhance the perfusion quantification, but their often large appearance differences and non-synchronous acquisition times engender considerable manual effort in order to align corresponding anatomical regions.

These problems lead to the main research question of this thesis: Can appropriate management of spatiotemporal information present in perfusion imaging and x-ray angiography ultimately improve the precision, objectivity, and ergonomics of clinical metric extraction?

The main objectives of the work presented in this thesis were thus to devise translatable strategies related to the selective mitigation and integration of the spatiotemporal components found in the series to tackle the concurrent and specific issues associated with the modalities mentioned above. In cardiac magnetic resonance perfusion imaging, a motion compensation framework was implemented using an optical flow formulation to automatically register sequential perfusion frames to a common anatomical geometry. This engine coupled histograms of oriented gradients landmark matching with variational optical flow to achieve subpixel accuracy in estimating both large and small nonrigid deformations. Special attention was given to ensure perfusion signal fidelity and operational efficiency by leveraging multithreaded hardware architectures. This framework was also used to register auxiliary series with perfusion frames using a reduction-to-unimodality paradigm that primarily encoded structural information and matched photometric distributions. The motion compensation approach was then translated to angiographic series, where the consistent alignment of the coronary arteries afforded their precise segmentation through coupling anisotropic Gaussian line filtering with the tracking of the contrast agent’s propagation through the vessels. Robustness to pathological segments such as aneurysms or ectasia was achieved with an automatic post-hoc correction routine. Lastly, the quantitative and qualitative performance of

the segmentation result led to the development of an arterial distensibility assessment tool that tracked selected vessel walls over a cardiac cycle to extract the variations of the vessels' diameters. Metrics related to the apparent wall stiffness were then proposed and the approach was tested in two clinical studies to assess its capacity to detect and stratify arterial stiffness in a cohort of Kawasaki disease patients with respect to their aneurysmal history or to lesions detected with intravascular optical coherence tomography.

The motion compensation approach was evaluated on a population of 291 adult patients who underwent cardiac magnetic resonance imaging under a wide range of acquisition parameters. The proposed system showed improved anatomical alignment scores compared with a state-of-the-art commercial solution. Notably, the approach was able to compensate motion both for those under a free breathing paradigm and for those who had failed apnea and gasped. In addition, auxiliary recordings such as arterial input function series and proton density images were successfully motion-compensated and the latter were well-registered to the perfusion series. The application of this framework to the fluoroscopic series proved beneficial, as the flow of the contrast agent through the arterial tree was successfully isolated and leveraged to segment vessels from a population of 31 pediatric patients. All pathological regions were successfully segmented and an automatic caliber extraction routine was used to demonstrate geometric fidelity with manual and semi-automatic commercial systems. Finally, the high quality segmentation results were used to initialize the distensibility assessment tool. The first clinical study found deteriorated distensibility in 13 Kawasaki patients, compared with the results from five healthy subjects. In addition, the tool was able to stratify between patients with and without a history of aneurysmal lesions. In the second clinical study, significant correlations were found between the number of arterial wall lesions and the computed distensibility metrics in an extended cohort of 27 Kawasaki disease patients. Overall, a trend towards aggravated stiffness assessed from the angiograms was found to be proportional to the number of lesions observed invasively.

In conclusion, this thesis presents spatiotemporal mitigation in terms of motion compensation of both perfusion and fluoroscopic series, and integration in terms of bolus and vessel wall tracking in the angiograms. These developments afforded greater metric extraction objectivity and efficiency by permitting the automation of myocardial perfusion quantification, as well as both static and dynamic vessel diameter extraction. In terms of future development, the natural evolution of the high quality segmentation result is the integration of multiple angiographic views around the patient to perform 3D reconstruction of the arterial network. Following this, the tracked bolus information used in the 2D segmentation result may then be used to initialize and modulate computerized fluid dynamics simulations inside the reconstructed coronary arteries to provide a patient data-driven assessment of blood flow.

These possibilities are particularly interesting when complex aneurysmal lesions are present, as certain rheological conditions may favor the development of thrombus or other worrisome conditions. For the distensibility assessment tool, its encouraging performance warrants its expanded investigation into adult atherosclerosis patients. In this population, it may help elucidate ambiguous plaque regions and analyze the health of vessel sections following interventions such as angioplasty or stenting utilizing newer bioresorbable materials.

TABLE OF CONTENTS

DEDICATION	iii
ACKNOWLEDGEMENTS	iv
RÉSUMÉ	v
ABSTRACT	ix
TABLE OF CONTENTS	xiii
LIST OF TABLES	xvii
LIST OF FIGURES	xviii
LIST OF SYMBOLS AND ABBREVIATIONS	xxii
CHAPTER 1 INTRODUCTION	1
1.1 Summary	4
1.2 Manuscript overview	5
CHAPTER 2 LITERATURE REVIEW	7
2.1 Cardiac physiology	7
2.2 Pathophysiology of prominent coronary artery disease (CAD) in adults and children	9
2.2.1 Vascular distensibility	12
2.3 Medical image registration	13
2.3.1 Transformation models	14
2.3.2 Registration methods	15
2.3.3 Reduction to unimodality	22
2.4 Segmentation of vascular structures	23
2.4.1 Centerline extraction	23
2.4.2 Appearance-based	24
2.4.3 Deformable models	26
2.4.4 Steerable filters	29
CHAPTER 3 RESEARCH HYPOTHESIS AND OBJECTIVES	32

3.1	General problem statement	32
3.1.1	cardiovascular magnetic resonance (CMR) perfusion imaging	32
3.1.2	X-ray angiographic imaging of coronary arteries	34
3.1.3	Coronary artery distensibility assessment via angiographic series	36
3.2	General methodology	37
3.2.1	Phase I - CMR perfusion imaging	37
3.2.2	Phase II - X-ray angiography	38
3.2.3	Phase III - Pilot studies of coronary arteries (CA) distensibility	39
CHAPTER 4 Article 1 : A ROBUST UNIVERSAL NONRIGID MOTION CORREC-		
TION FRAMEWORK FOR FIRST-PASS CARDIAC MAGNETIC RESONANCE		
PERFUSION IMAGING		40
4.1	Abstract	40
4.1.1	Background	40
4.1.2	Methods	40
4.1.3	Results	40
4.1.4	Conclusion	41
4.2	Background	41
4.2.1	Motion compensation requirements	42
4.3	Methods	43
4.3.1	Study Population	43
4.3.2	Image Acquisition	43
4.3.3	Motion Correction Framework	44
4.3.4	Image pre-processing	45
4.3.5	Reference perfusion frame and PD frame detection	45
4.3.6	Large displacement optical flow motion estimation	45
4.3.7	PD-to-perfusion image registration	48
4.3.8	Image post-processing	48
4.3.9	Performance Evaluation	49
4.3.10	Sequential perfusion frame consistency	50
4.3.11	PD-to-perfusion registration	50
4.3.12	LV and myocardial perfusion dynamics	50
4.3.13	LV centroid displacement	51
4.3.14	Statistical analysis	51
4.4	Results	51
4.4.1	Sequential perfusion frame consistency	52

4.4.2	AIF image registration	54
4.4.3	PD-to-perfusion registration	55
4.4.4	LV and myocardial perfusion dynamics	56
4.4.5	LV centroid displacement	58
4.5	Discussion	58
4.6	Conclusion	62
CHAPTER 5	Article 2 : SPATIOTEMPORAL ANALYSIS OF ANGIOGRAPHIC SE-	
	RIES FOR PATHOLOGICAL CORONARY ARTERY SEGMENTATION	63
5.1	Abstract	63
5.2	Introduction	63
5.3	Materials and methods	67
5.3.1	Angiographic data acquisition	67
5.3.2	Motion compensation	68
5.3.3	Image preprocessing	68
5.3.4	Curvilinear structure extraction	69
5.3.5	Spatiotemporal masking	71
5.3.6	Aneurysm region correction	74
5.3.7	Automatic diameter computation	74
5.4	Experimental	74
5.5	Results	75
5.6	Discussion	77
5.7	Conclusions	78
5.8	Acknowledgment	78
CHAPTER 6	MEASURING CORONARY ARTERY DISTENSIBILITY VIA ANGIO-	
	GRAPHIC SERIES	80
6.1	Introduction	80
6.2	Distensibility assessment via segmentation and spatiotemporal tracking . . .	81
6.2.1	Pilot clinical studies	83
6.2.2	Discussion	84
CHAPTER 7	GENERAL DISCUSSION	87
7.0.1	Motion compensation and registration of CMR perfusion series	87
7.0.2	Automatic coronary artery segmentation	89
7.0.3	Coronary artery distensibility assessment via angiographic series . . .	90

CHAPTER 8	CONCLUSION	93
8.1	Future developments	93
8.1.1	Motion compensation and registration	93
8.1.2	Extended distensibility analysis	94
8.1.3	3D reconstruction of the coronary tree	94
8.2	Recommendations and perspectives	96
BIBLIOGRAPHY	97

LIST OF TABLES

Table 4.1	Patient numbers according to acquisition characteristics.	43
-----------	---	----

LIST OF FIGURES

Figure 1.1	Fluoroscopic angiography findings of a) CA stenosis in an adult patient (white arrow, image by Siemens Healthcare Inc.), and b) aneurysms on the left CA of a Kawasaki disease (KD) pediatric patient (image by LIV4D).	2
Figure 1.2	CMR perfusion imaging of the left ventricle (LV). Myocardial perfusion defect apparent at the top-left region of the quantified perfusion pixel map. Image from [101].	3
Figure 1.3	CMR perfusion imaging sequence types. fast imaging with steady-state free precession (FISP) and fast low angle shot (FLASH) sequence types are shown for T1-weighted, Proton density (PD), and arterial input function (AIF) images. The resolution of the AIF images were doubled to allow better visualization.	4
Figure 2.1	Anatomy of the heart : a) structural components including the right and left atria and ventricles ; and b) coronary circulation comprised of the right and left coronary arteries supplying oxygenated blood to the myocardium. Images by Patrick J. Lynch, medical illustrator, used under Creative Commons license.	8
Figure 2.2	CA layers. Histological slice of a healthy CA, where connective tissue are dyed blue (collagen) and black (elastin). Smooth muscles cells are dyed red. Image from Frederick Memorial Hospital, used under Creative Commons license.	9
Figure 2.3	Atherosclerosis progression. Circulating cholesterol accumulates between the intima and media layers of the arterial walls, which progresses to plaque formation and calcification. Image by Mayo Clinic.	10
Figure 2.4	Selective angiograms of a KD patient's left CA. Aneurysms are observed at the proximal location of the branches. Images by LIV4D.	11
Figure 2.5	Image registration pipeline. The source image is aligned to the target image following estimation and optimization of spatial transformation parameters guided by a similarity measure.	14
Figure 2.6	Histograms of oriented gradients : a) The histograms of oriented gradients (HOG) descriptor is formed by sampling nine equidistant points in a 7 x 7 neighbourhood, b) HOG point matches of sequential end-diastolic angiographic frames. The second frame was rotated and rescaled artificially to demonstrate affine matching performance.	17

Figure 2.7	Vessel parametrization via centerline and diameter computation on segmented and binarized coronary arteries. Image by LIV4D.	24
Figure 2.8	Topology-Adaptive Snakes. Merging and branching of multiple snake elements in a retinal fundus frame. Images adapted from [164].	28
Figure 2.9	Generic steerable filtering framework. Adapted from Freeman et al. [73]. .	29
Figure 2.10	Appearance-based vessel extraction showing segment hollowing (red arrow) and tree-discontinuities (yellow arrow) : a) Original image, b) Frangi-based enhancement, c) Results from [251]. Images adapted from [251].	30
Figure 3.1	Development plan stemming from spatiotemporal analysis addressing the issues encountered in CMR perfusion imaging, x-ray angiography, and the application of coronary artery segmentation to static vascular parametrization and distensibility assessment.	37
Figure 4.1	Automatic Nonrigid Motion Correction Framework. Image processing pipeline of our proposed system using a robust large displacement optical flow (LDOF) approach for first-pass CMR perfusion image series and auxiliary series.	44
Figure 4.2	Displacement Flow Fields Computation. Longitudinal (x) and transversal (y) displacement flow fields between pairwise sequential frames are computed using an optical flow (OF) formulation robust to large displacement (LDOF). This approach couples discrete feature point tracking computed from histograms of oriented gradients (HOG) with a continuous variational optical flow step. The discrete HOG matches (red vectors) are displayed and superimposed on the first CMR image of the pair.	46
Figure 4.3	Automatic Flow Field Distortion Correction. Distorted (left) and automatically correction (right) flow field magnitudes are shown for comparison. Automatic correction is performed using statistically-determined threshold (green line).	47
Figure 4.4	PD-to-Perfusion Image Registration. The median PD-weighted image and median T1-weighted perfusion image are computed from the series and processed to enhance gradient information and match photometric profiles. These are used as bridge images for image registration via the LDOF processing engine.	49

Figure 4.5	Comparison of Sequential Perfusion Frame Mean Consistency Curves. Temporal variability of the mean correlation coefficient (R^2 ; top row) and mutual information ($MuInfo$; bottom row) metrics computed across the T1-weighted perfusion series of the entire cohort for both full frame (left column) and heart region (right column).	53
Figure 4.6	Comparison of Sequential Perfusion Frame Consistency. Mean correlation coefficient (R^2 ; top row) and mutual information ($MuInfo$; bottom row) metrics computed across the T1-weighted perfusion series for both full frame (left column) and heart region (right column) of the entire cohort.	54
Figure 4.7	Comparison of Sequential Perfusion Frame Consistency for Breathing Paradigms. Mean correlation coefficient (R^2 ; top row) and mutual information ($MuInfo$; bottom row) metrics computed for free-breathing (left column) and breath-hold (right column) cohorts.	55
Figure 4.8	Comparison of PD-to-Perfusion Image Registration. Top two rows show examples of PD (red) to T1 (green) perfusion image registration with corresponding correlation scores for three different sequence combinations. Bottom row shows the mean correlation coefficient (R^2) computed between the last PD image and the first T1 perfusion image over the entire cohort.	56
Figure 4.9	Comparison of LV and Myocardial Perfusion Dynamics. Top three image rows show the change of contrast dynamic during a stress perfusion series as well as LV and myocardium sectors defined by different regions of interest (ROI). The ROI were traced on motion corrected images (LDOF-MOCO) and then backwarped to the raw perfusion images (Raw-BW) to generate the corresponding sectoral signal intensity (SI) curves as shown. As a comparison, SI curves of the raw perfusion images without ROI backwarping (Raw) were also generated to show the impact of image motion in different myocardial sectors. In contrast to large motion-related signal intensity fluctuations in the raw SI curves (sector 4 and sector 5), LDOF-MOCO and Raw-BW curves are much smoother and are almost indistinguishable from each other.	57
Figure 4.10	Perfusion Dynamics Comparison. Correlation (R^2) and normalized root-mean-square error (NRMSE) comparisons of time signal intensity curves in LDOF-MOCO vs. Raw-backwarped, and Raw vs. Raw-backwarped, image series.	58

Figure 4.11	LV centroid excursions. Frame-to-frame LV centroid positions illustrating the amount of translational motion on three slices of a typical stress perfusion image series. The origin (green) is the LV centroid position measured from the LDOF motion corrected perfusion images.	59
Figure 5.1	Angiogram motion correction : a) Raw end-diastolic sequence, b) Motion-corrected end-diastolic sequence. The mean sequential correlation coefficients are reported in this example as a measure of frame-to-frame alignment.	69
Figure 5.2	Angiographic frame processing : a) Raw, b) DT-CWT filtered, c) Homomorphic filtered, d) Anisotropic curve extracted & rectified, e) Connectivity pruned & tortuosity normalized. Arrows indicate remaining non-vessel structures.	69
Figure 5.3	Optical flow analysis and motion mask creation : a) Curve-extracted sequence (top) and motion map sequence (bottom, color-graded to velocity magnitude), b) kPCA-computed flow map, c) Binary motion mask, d) Masked peak vessel frame.	73
Figure 5.4	Aneurysm detection : a) Raw frame aneurysm, b) Curve-extracted frame, c) Detected aneurysm area (cyan), d) Aneurysm-corrected segmentation.	75
Figure 5.5	Segmentation performance : a) Mean diameter difference (\pm s.d.) between automatic and manually measured vessel diameters, b) Linear regression between automatic and manual diameter measures, c) Enlarged distal regions of raw (top row) and segmented (bottom row) vessels.	76
Figure 5.6	Automatic segmentation results. Raw angiographic frames with segmented result pairs. First and second columns : healthy arteries. Third and fourth columns : pathological arteries (Kawasaki disease patients).	79
Figure 6.1	Distensibility assessment pipeline. Segmented CA wall pixels are tracked over the angiographic series, producing the caliber vs. time curve $C(t)$ shown at right.	81
Figure 6.2	Caliber variations and pressure dynamics : a) the measured caliber vs. time curve produced by the proposed distensibility assessment framework on a proximal segment of a KD patient ; b) the prototypical pressure dynamics of the heart and surrounding vasculature during systolic and diastolic phases.	82
Figure 6.3	Distensibility metrics of healthy (CTL) and KD patients with (KDAN+) and without (KDAN-) history of aneurysmal lesions.	85
Figure 6.4	Distensibility metrics of KD patients according to their OCT score indicating the cumulative presence of observed arterial wall lesions.	86

LIST OF SYMBOLS AND ABBREVIATIONS

AIF	arterial input functions
APV	average peak velocity
ASIFT	affine-SIFT
CA	coronary arteries
CAD	coronary artery disease
CFD	computational fluid dynamics
CFV	coronary flow volume
CMR	cardiovascular magnetic resonance
CT	computerized tomography
CVD	cardiovascular disease
CVR	coronary vessel resistance
DOG	difference of gaussians
ECG	electrocardiogram
FFD	free-form deformation
FISP	fast imaging with steady-state free precession
FLASH	fast low angle shot
GLOH	gradient location and orientation histogram
GPU	graphical processing units
HOG	histograms of oriented gradients
ICA	independant component analysis
IVUS	intravascular ultrasound
KD	Kawasaki disease
LA	left atrium
LCA	left coronary arteries
LDL	low-density lipoprotein
LDOF	large displacement optical flow
LV	left ventricle
MOCO	motion compensation
MR	magnetic resonance
MRI	magnetic resonance imaging
MSD	mean squarred differences
MuInfo	mutual information
NMuInfo	normalized mutual information

OCT	optical coherence tomography
OF	optical flow
PASHA	pair and smooth hybrid algorithm
PCA	principal component analysis
PCA-SIFT	principal component analysis-scale invariant feature transform
PD	proton density
PET	positron emission tomography
RA	right atrium
RBF	radial basis functions
RCA	right coronary arteries
RMuInfo	regional mutual information
RNA	ribonucleic acid
ROI	region of interest
RV	right ventricle
SFS	Shape from Silhouette
SIFT	scale invariant feature transform
SNR	signal-to-noise ratio
SPECT	single photon emission computed tomographic
SSD	sum of squared differences
SURF	speeded up robust features
US	ultrasound

CHAPTER 1 INTRODUCTION

Globally, cardiovascular disease (CVD) is implicated in more than 17 million deaths per year, which corresponds to a staggering 30% of all deaths combined [268] and is projected to remain the leading cause of mortality by 2030 [161]. Within CVD, coronary artery disease (CAD) alone is responsible for 46% of deaths in men and 38% in women [166]. Injuries or lesions of the coronary arteries (CA) will affect the irrigation of the myocardial tissue responsible for pumping blood to and from the lungs and the rest of the body. Myocardial injury related to CAD is primarily manifested in the form of angina and may progress to infarction, which are consequences of ischemia related to insufficient oxygenation of the muscular cells comprising the myocardium.

Diagnosing CAD has traditionally involved imaging the vessels with fluoroscopic (x-ray) angiography [46]. The procedure involves inserting a catheter through the femoral artery in the patient's hip area, guiding it in the aorta, and eventually positioning it to the CA tree's ostium. A contrast agent is then pumped in the catheter and released in the arterial network while a series of x-ray images are acquired at a relatively fast sampling rate (15 to 30 Hz). The radiodense contrast agent's propagation through the vessels' lumen produces a visualization of the arteries and possible pathological lesions in the form of stenosis or aneurysms are thus revealed, as shown in Figure 1.1. The length of the acquired series typically reaches around 200 frames per angular configuration, showing not only the arteries, but a large portion of the thoracic region undergoing movement related to the patient's respiration and heartbeats, in addition to the occasional clinician adjustment of the imaging gantry and patient position. The radiodense structures (arteries, bones, organs, instruments) thus present large and complex nonlinear motion throughout the acquired series. These spatiotemporal components are significantly more pronounced in pediatric patients as they are naturally less cooperative and their basal heart rate is higher than adults [237, 125].

In addition to the visual information contained in the angiograms, the operator will select a single frame showing a large portion of the CA tree and collect quantitative metrics to stratify the severity of the patient's lesions. The primary clinical measure is the vessels' diameters (also-known-as calibers) from which an obstruction percentage or dilation index can be computed by taking the ratio of the vessels size in the pathological region and the adjacent normal looking areas. These measures are typically performed manually by a radiological technician and will guide the clinician's evaluation and subsequent treatment course [51, 224]. Following diagnosis, fluoroscopic angiography is also used during interventional therapy such

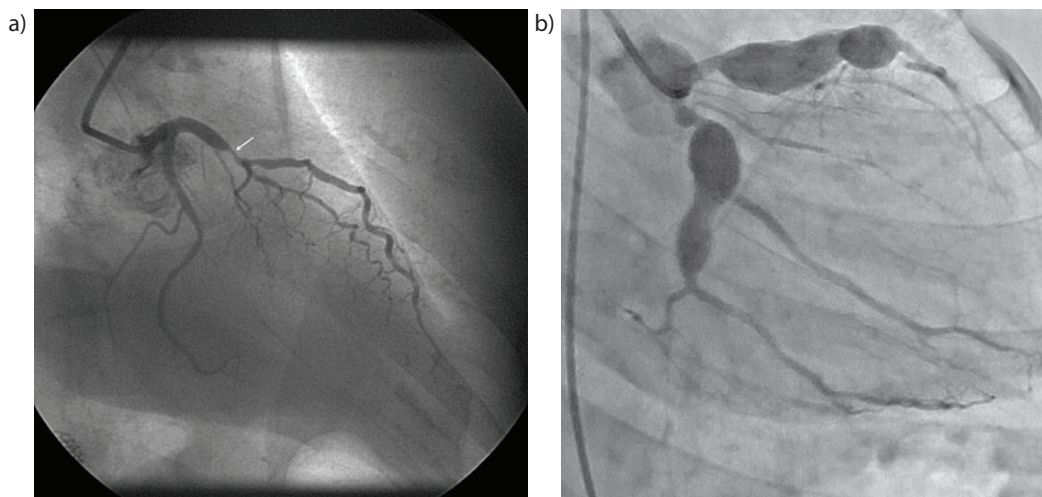


Figure 1.1 Fluoroscopic angiography findings of a) CA stenosis in an adult patient (white arrow, image by Siemens Healthcare Inc.), and b) aneurysms on the left CA of a KD pediatric patient (image by LIV4D).

as angioplasty, stenting, ablation, and patient follow-up.

The two-dimensional nature of x-ray angiography can, however, be limiting as the angle of the imaging gantry may affect the appearance of potentially pathological arterial segments. As such, lesions may be missed or misdiagnosed. Furthermore, in the case of stenotic regions, apparent narrowing may not entirely reflect the health of the heart's tissue as collateral vessel formation, which is the body's response to decreased blood flow from the primary CA, may compensate and re-establish appropriate myocardial oxygenation. Also noteworthy is the cumulative radiological exposure induced by this modality and its associated genotoxic effects [6, 69], which are naturally more worrisome for children due to their young development age [3, 5]. In light of this, a relatively newer imaging modality used to diagnose CAD, cardiovascular magnetic resonance (CMR) perfusion imaging [7], is increasingly gaining clinical implementation as it offers a non-invasive and non-ionizing assessment of cardiac disease, compared to x-ray angiography, single photon emission computed tomographic (SPECT) or positron emission tomography (PET). Whereas x-ray angiography is used to evaluate directly the CA, perfusion imaging is used to detect the downstream capillary blood flow within the myocardial tissue [80]. This modality uses various T1-weighted sequence types to record the transit of an intravenously delivered gadolinium-based contrast agent [25] through the cardiac chambers. The injected bolus will eventually perfuse through the extravascular regions of the myocardium, which is where qualitative and quantitative information will be analyzed to assess the health of the patient's heart following myocardial infarction or suspected CA narrowing. In the former case, the goal is to precisely estimate the size of the deficient micro-

vascular perfusion within the myocardium [149]. Compromised areas are known as *perfusion defects* and will appear darker compared to healthy, adequately perfused tissue. These regions can be inspected manually through expert observation and subsequently drawn by hand or detected fully automatically using quantitative pixel-maps [101], as seen in Figure 1.2. These geometrical or quantitative perfusion measurements are then used in treatment planning and patient prognosis. To investigate suspected CAD, the key metric is a noticeably compromised perfusion rate resulting from the drop in coronary pressure downstream of the stenotic region in patients with significant coronary obstruction. In normal non-ischemic myocardiums, the magnitude of the perfusion will increase without changes in myocardial blood flow [107].

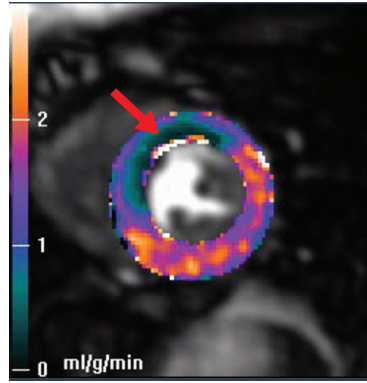


Figure 1.2 CMR perfusion imaging of the LV. Myocardial perfusion defect apparent at the top-left region of the quantified perfusion pixel map. Image from [101].

Cost and expertise factors will determine the type of magnetic resonance (MR) sequence used and thus varies from clinical site, but typically include either fast low angle shot (FLASH) or fast imaging with steady-state free precession (FISP) configurations acquired in 1.5T or 3.0T magnetic field strengths. These configurations each produce inherently different appearances of the imaged anatomical structures. Auxiliary images are also increasingly recorded in CMR imaging to enhance quantitative analysis. For example, AIF images are a class of series specifically designed to maintain linearity of pixel intensity variations in the LV during bolus transit and are used to accurately estimate blood flow [79]. Their dynamic range is larger than the standard T1-weighted images, but as a tradeoff, present lower image resolution and signal-to-noise ratio (SNR). Examples of different sequence types are shown in Figure 1.3.

Proton density (PD) weighted images are another type of auxiliary series used in a pre-processing step to enhance perfusion quantification precision by normalizing myocardial pixel intensity inhomogeneities related to the magnetic field's nonlinear distribution [100, 174]. As with the AIF series, their appearance is different from perfusion T1-weighted images and may be acquired using mismatched sequence types. They are typically recorded prior to perfusion

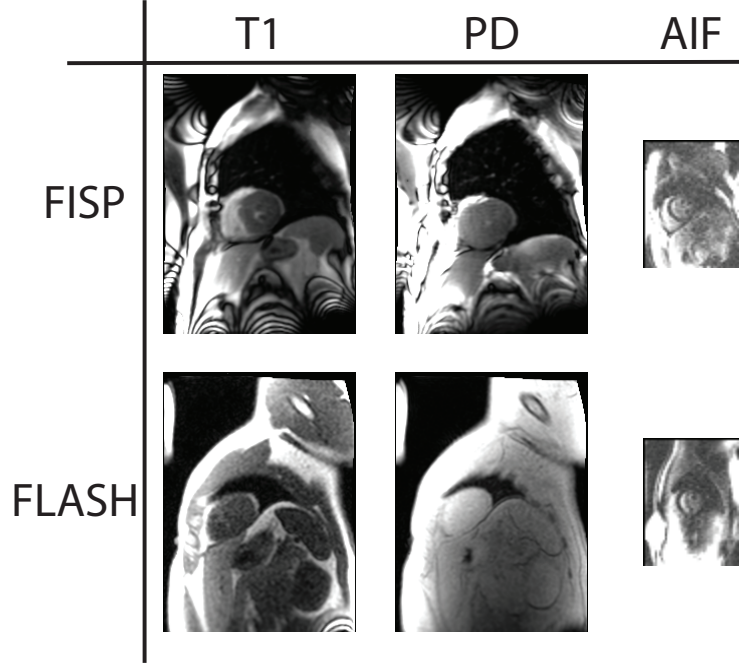


Figure 1.3 CMR perfusion imaging sequence types. FISP and FLASH sequence types are shown for T1-weighted, PD, and AIF images. The resolution of the AIF images were doubled to allow better visualization.

imaging and the resulting anatomical structures may thus be misaligned to their T1-weighted counterparts.

Despite the development and optimization of acquisition techniques and parameters, many studies are still hindered by spatiotemporal deformations of the heart and surrounding tissue during the acquisition period [215]. As perfusion analyses increasingly target pixel and sub-pixel resolutions, the necessity of high quality frame-to-frame anatomical correspondence becomes critical and is typically performed by labor-intensive and subjective operator interaction [264, 88, 283].

1.1 Summary

The recurring issues exposed in this chapter are related to the insufficient use or management of the recorded spatiotemporal information and the manual, subjective, and laborious nature of the metrics collected from pervasive cardiac imaging modalities critical to diagnosing CAD.

In x-ray angiography, the dynamic nature of the recorded series have caused researchers and clinicians to shy away from the spatiotemporal information they contain and thus largely focus their analysis on a single frame. We thus argued that this modality is under-exploited

as the temporal tracking of the contrast agent and CA themselves can potentially enhance image analysis algorithms and provide complimentary and decisive diagnostic clues. Further, the use of manually measured vessel metrics is problematic in terms intra and inter operator variability and time management. However, precluding automatic metric extraction from this modality implies the precise and efficient segmentation of the CA, but as it will be shown in the following chapters, this procedure presents engineering challenges in terms of spatiotemporal information management that must be addressed appropriately before clinical consideration.

CMR perfusion imaging is also plagued by manual intervention due in large part to the series' dynamics in terms of anatomical movement and temporal voxel intensity fluctuations while identifying possible pathological myocardial regions. Indeed, the high-precision perfusion information afforded by quantified pixel maps requires substantial operator labor in terms of aligning the anatomical structures undergoing nonrigid deformations throughout the perfusion series. Automatic motion compensation (MOCO) within the series would thus be a welcomed addition to the perfusion analysis pipeline. An extension of this issue is found in the integration of auxiliary series used to enhance perfusion estimates. These either have to be corrected for motion intrinsically or registered to the standard perfusion series, despite their wildly varying appearance characteristics.

This thesis aims to address the problems highlighted above by resolving the specific and potentially high impact issues related to 1) the automatic nonrigid motion compensation and registration of CMR perfusion series; 2) the automatic segmentation of CA from x-ray angiographic series using spatiotemporal integration and subsequent metric extraction; and 3) the automatic assessment of CA distensibility via the spatiotemporal tracking of the arterial walls using the CA segmentation result.

1.2 Manuscript overview

The thesis is organized as follows : Chapter 2 reviews cardiac physiology, prevalent CAD in adults and children, CA distensibility, and the background art related to medical image registration and vessel segmentation techniques. Chapter 3 details the specific research hypothesis and objectives, highlighting the general approach used to remedy the issues outlined above.

The first article is presented in Chapter 4, where a universal nonrigid CMR perfusion MOCO and registration framework is proposed. Part of this work was subsequently translated in the second article proposed in Chapter 5, where the MOCO framework was employed to

enhance the precision of an automatic segmentation method of healthy and pathological CA using spatiotemporal integration. The third contribution is detailed in Chapter 6, where the segmentation framework is used in conjunction with spatiotemporal tracking to compute CA distensibility from x-ray angiographic series. Multiple stiffness-related metrics are proposed and two preliminary clinical studies of Kawasaki disease (KD) patients using these measures are presented with encouraging results.

Chapter 7 offers a global synthesis of the work, including the limitations of the proposed approaches and Chapter 8 concludes with future development endeavors, recommendations, and perspectives.

CHAPTER 2 LITERATURE REVIEW

This chapter first examines cardiac physiology and prevalent CAD in adults and children with an added focus on their consequences on vascular stiffness. This is followed by the background art related to general medical image registration techniques and a review of vascular structure segmentation – the precursory step to automatic clinical metric extraction – closes the chapter.

2.1 Cardiac physiology

The human heart is a hollow muscular organ that pumps blood to maintain circulation throughout the body. It is located at the center of the mediastinum and is cone-shaped with the dimensions of an adult-sized fist (approximately 12 cm x 8 cm x 6 cm) at maturity [178]. The heart is divided into the left and right sides, each comprised of two chambers : an atrium and a ventricle, as illustrated in Figure 2.1a. The atria receive blood before transferring it to the ventricles during the cardiac cycle, which is summarized below :

1. *Right atrium diastole* : Deoxygenated blood enters the right atrium (RA) from the venae cavae.
2. *Right atrium systole* : The contraction of the RA pumps blood to the relaxed right ventricle (RV) through the tricuspid valve.
3. *Right ventricle systole* : The RV contracts and pushes blood to the lungs through the pulmonary valve and pulmonary artery. Gaseous exchange oxygenates the blood in the lungs.
4. *Left atrium diastole* : The oxygenated blood returns to the heart via the pulmonary veins and into the left atrium (LA).
5. *Left atrium systole* : LA contraction, coupled with the expansion of the LV displaces the oxygenated blood to the LV.
6. *Left ventricle systole* : The contraction of the LV ejects the oxygenated blood through the aorta, where is it circulated throughout the body.

The left and right side of the heart operate simultaneously with synchronicity of the cardiac muscles during contraction (systole) and relaxation (diastole). The contractions are initiated in the upper chambers (RA and LA) by electrical activation and propagate by conduction to the lower chambers (RV and LV). The familiar double beat *lub-dub* sound of the heart

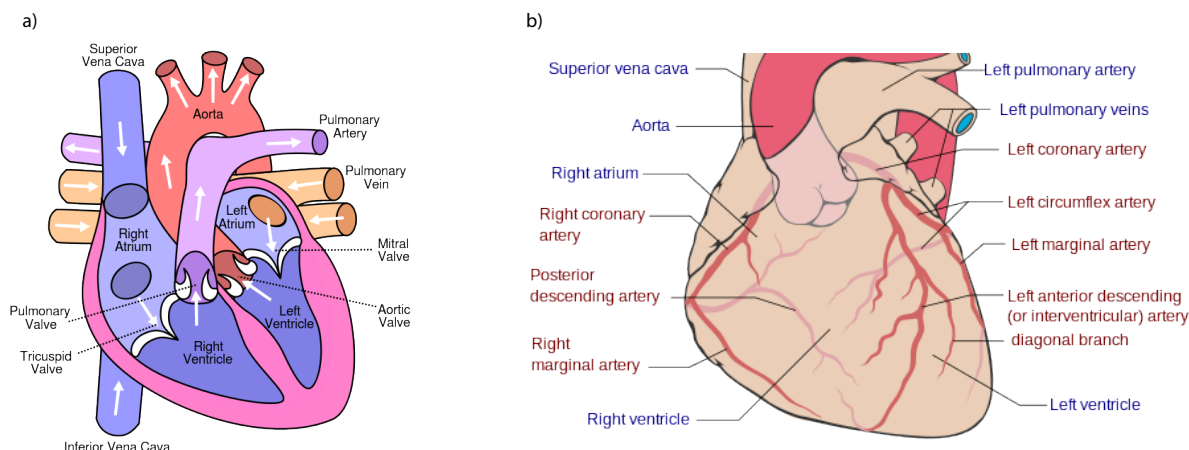


Figure 2.1 Anatomy of the heart : a) structural components including the right and left atria and ventricles ; and b) coronary circulation comprised of the right and left coronary arteries supplying oxygenated blood to the myocardium. Images by Patrick J. Lynch, medical illustrator, used under Creative Commons license.

is produced by the blood colliding with closed valves. The closure of the tricuspid and mitral valves cause the *lub* noise, followed by the closure of the pulmonary and aortic valves, producing the *dub* sound.

The myocardium is composed of striated involuntary muscles called cardiomyocytes and is oxygenated through circulation via the left coronary arteries (LCA) and right coronary arteries (RCA). These vessels run on the surface of the heart, as illustrated in Figure 2.1b, and are classified as *end circulation* as they are the sole blood supply to the heart tissue. Pathology of these vessels is thus of critical concern. The LCA supplies blood to the LA, LV, and the interventricular septum, whereas the RCA irrigates the RA, portions of both ventricles, and the heart's conduction system.

The wall of the CA is composed of three layers (also-known-as tunica) : the adventitia (outer), media (middle), and intima (inner), as shown in Figure 2.2. The intima is composed of connective tissue (collagen and elastin), and a layer of elastic tissue (known as the internal elastic lamina). The luminal surface of the intima is covered with endothelial cells, which control artery growth and mediate blood pressure and flow through chemical signaling to the smooth muscle cells of the media layer. These will contract and relax to, respectively, constrict and dilate the luminal area of the artery. Lastly, the adventitia's primary function is structural support and is thus largely composed of connective and supporting tissue.

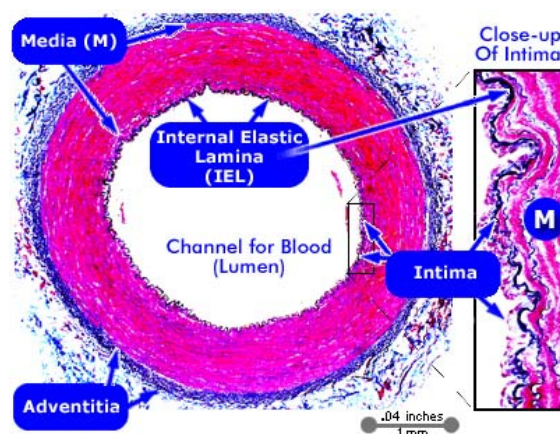


Figure 2.2 CA layers. Histological slice of a healthy CA, where connective tissue are dyed blue (collagen) and black (elastin). Smooth muscles cells are dyed red. Image from Frederick Memorial Hospital, used under Creative Commons license.

2.2 Pathophysiology of prominent CAD in adults and children

The most prevalent ischemic disease in adults is atherosclerosis, which is the result of plaque buildup inside the walls of, preferentially, high pressure vessels such as the coronary, femoral, cerebral, and carotid arteries. As illustrated in Figure 2.3, the gradual accumulation of plaque will narrow the vessels' lumen and can eventually harden and lead to partial or complete blockage of the vessels (also-known-as stenosis), which can progress to severe complications, notably when the plaque is located inside the CA. Atherosclerosis begins where the endothelium is damaged by factors such as high blood pressure, smoking, or high cholesterol diets. The damaged areas allow low-density lipoprotein (LDL), the so-called “bad” cholesterol, to migrate behind the arteries' endothelial lining. This triggers white blood cells to accumulate and neutralize the LDL, creating the plaque. Over time, it will grow and will be constituted of inflammation-causing active white blood cells, remnants of dead cells, and fatty material that eventually calcify and crystallize into other material. Understandably, plaque-ridden areas will increase the arteries' stiffness. Besides the blood flow obstruction caused by atherosclerosis, vulnerable plaques may abruptly rupture and release a thrombus that will migrate downstream to narrower vessels and can suddenly compromise or completely block blood flow, often with catastrophic outcomes.

In pediatric populations of developed countries, the leading cause of acquired CAD is Kawasaki disease (KD) [188]. In Japan alone, 1% of children between the ages of three months to five years will develop this self-limited acute vasculitis [180]. The etiology of KD is still unknown, but some evidence points to a ribonucleic acid (RNA) virus infection in the lungs

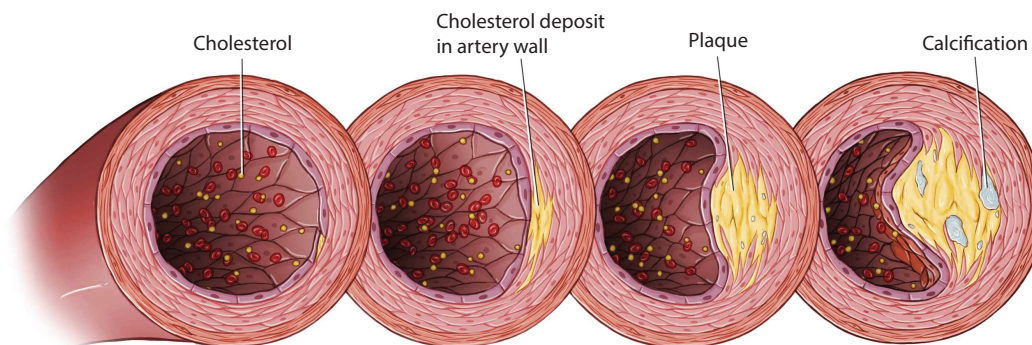


Figure 2.3 Atherosclerosis progression. Circulating cholesterol accumulates between the intima and media layers of the arterial walls, which progresses to plaque formation and calcification. Image by Mayo Clinic.

triggering a cascade of events leading to a systemic inflammatory response in children with a certain genetic predisposition to the disease [204, 205]. Others have found strong and consistent correlations between seasonable shifts in the winds and regional flareups of the disease. This puts the viral association into question as the incubation period of such infectious agents is too long compared to the first manifestation of symptoms following the exposure to what is carried in the wind, as argued by [202]. Indeed, that study pointed to a fungal toxin related to the candida family that was found in tropospheric winds during high incidence periods.

Of critical interest, the inflammatory response will affect medium-sized, extraparenchymal muscular arteries such as the CA [57] and may quickly lead to their deterioration. Histological findings have demonstrated thinning and destruction of the tunica media [185], the loss of endothelial cells, and the degradation of the vascular smooth muscles cells and elastic fibers into hyalinized connective tissue [256]. These factors contribute to the loss of supportive vessel wall structures and will lead to CA aneurysms in 10% – 25% of the patients during the acute phase of the disease. This type vessel lesion is characterized physiologically by localized dilations of the CA, as shown in the angiographic projections of Figure 2.4 and is defined by its shape as either saccular, fusiform, or ectasic. Its sizing is based on the ratio of their maximum diameter and adjacent normal looking vessel : small (1.5x increase), medium (1.5x-4.0x), large ($> 4.0x$), according to the classification of the Kawasaki Disease Research Committee of the Japanese Ministry of Health and Welfare [135]. An aneurysm can also be considered giant if its maximum diameter exceeds eight millimeters. Newer guidelines, however, encourage the use of the z-score computed using patient's height, weight, and vessel caliber measurements, which has been shown to be a robust marker and good predictor of risk factors during the evolution of the disease [56, 162]. As eluded above, x-ray angiography

is the gold-standard diagnostic tool, where presence of aneurysmal regions on the CA is considered the definitive indicator of KD. However, as is the case in adult CAD assessment, analysis of the angiograms are currently performed using manual measurements.

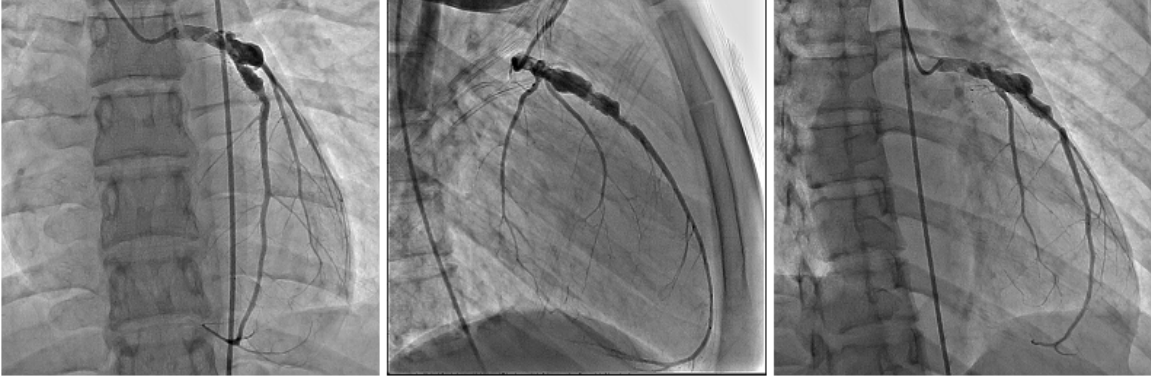


Figure 2.4 Selective angiograms of a KD patient's left CA. Aneurysms are observed at the proximal location of the branches. Images by LIV4D.

Aneurysms may lead to ischemic heart disease in 5% of the KD cases [113, 115] and can deteriorate to infarction [207, 233, 275, 114, 74]. Autopsy findings have shown that ischemia is likely the outcome of thrombosis formation on the aneurysms' wall [238]. Rheological analyses also point to precarious hemodynamic factors inside these lesions. Using invasive pressure gage and velocity measurements by Doppler flow, [135] showed that there is a decrease in both the average peak velocity (APV) and shear index inside aneurysms. These measures were also negatively correlated with the size of the lesions. For patients with giant aneurysms, the APV decreases at the proximal position and accelerates at the outset of the aneurysm. This finding is concerning as it has previously been shown that thrombus formation increases at low flow velocity and reaches maximum production as the flow rate subsequently accelerates quickly [16, 194]. It is also known that recirculative flow patterns can form inside aneurysms and can cause a pronounced drop in sheer stress magnitude, which also activates the platelets [21]. These results suggest that the fluid mechanical conditions found inside aneurysms are an ideal breeding ground for thrombosis.

Patients presenting with CA aneurysms can also suffer from non-obstructive ischemic events caused by the deficient flow characteristics in these pathological segments [134]. Angiographically, the fluid dynamics inside aneurysms are visually cued by the stasis of dye, segmental back flow, swirling, and a *striking* slow flow pattern [133, 200, 236]. These are indicators of an increase coronary vessel resistance (CVR) and possible inadequate modulation of the coronary flow volume (CFV). Indeed, [134] showed that the alterations of the flow dynamics

likely result in inadequate perfusion of the myocardium and can lead to exercise-induced infarction. Quantitatively, they found an increase in CVR and concurrent decrease in CFV under cardiac pacing in patients with coronary aneurysms and reported episodes of angina pectoris. These studies further solidify the correlation between hemodynamic factors and the propensity of pathological conditions and outcomes. Despite these findings, however, clinical decisions still largely rely on manual geometrical-based measurements on static frames.

Treatment of KD patients typically involves a pharmaceutical plan consisting of intravenous immunoglobulin, which is shown to reduce the risk of aneurysm formation by a factor of five if administered early in the presentation of the disease [183]. The American Heart Institute guidelines for the long-term management of patients with KD [184] are based on *Level of Evidence C* (expert opinion, case studies, or standard of care). For patient with giant aneurysms, systemic anticoagulation therapy is shown to reduce morbidity and mortality [209], but there is no consensus for patients with smaller aneurysms. Furthermore, even in patients where aneurysms have regressed, there is concerning evidence of sustained functional sequelae of the vascular wall despite patent angiographic findings [103].

2.2.1 Vascular distensibility

Pathological investigations have found that regressed aneurysm sites are marked by endothelium injury and the thickening of the intima primarily caused by the proliferation of smooth muscle cells during the acute phase of KD, but can nonetheless present with normal lumen diameters [210]. Naturally, one would hypothesize that these findings will have an effect on the functional properties of the vessels, and intravascular ultrasound (IVUS) was thus used by [103] to assess the vasomotion response of the arteries following infusion of a vasodilating agent (acetylcholine). Impaired vasomotion at regressed aneurysm sites was observed by the paradoxical constriction of the vessels after dilator administration, which is an indication of endothelium dysfunction [154]. Of particular concern, these findings were shown to persist over long-term follow-up (over 10 years after disease onset).

For adult patients with CAD, a similar trend is observed. In atherosclerosis, vascular wall stiffness is directly related to the atheromatous changes of the CA [35], but as reported in [223], even in the absence of angiographically significant stenosis, the distensibility properties of the arteries measured manually on magnified angiographic series were found to be impaired. These results were corroborated with IVUS by [181], who found reduced distensibility without signs of luminal abnormalities. Quantitative vessel distensibility assessment may thus be an alternative way to determine the extent of atherosclerosis, especially at the early stages of the disease.

These findings of impaired vascular distensibility show a concerning reality for patients with CAD : the gold-standard diagnostic tool for their disease, namely x-ray angiography, is largely under-utilized by selecting a single static image where manual calipers at only one point in time are measured. Disconcertingly, this image may show normal vessels despite vascular dysfunction. In a hypothetical clinical situation where multiple frames would be used to assess distensibility, the manual nature of the task may compound measurement errors related to the natural subjectivity of the human operator and would largely increase measurement time. The alternatives, IVUS, or more recently optical coherence tomography (OCT), are seldom used in practice and their invasive nature may not be advisable for certain patients, especially for those at pediatric ages. A less invasive, automatic assessment of vascular distensibility using data that is already routinely collected would thus be a welcomed clinical tool.

2.3 Medical image registration

This section reviews medical image registration at a global level. As such, approaches specifically related to MOCO are presented in Chapter 4.

Medical image registration has occupied the computer vision field for more than four decades [98], where the primary area of research was historically focused on registration of relatively stable brain images acquired on different modalities. In broad terms, image registration is the spatial alignment of corresponding structural components between a target and source image by estimating a suitable geometric transformation and applying it under a strict measure of congruence. This is a crucial preprocessing step as in many clinical protocols, multiple image modalities such as computerized tomography (CT), magnetic resonance imaging (MRI), ultrasound (US), and x-ray may be acquired. Each offers different qualitative and quantitative information instrumental to the clinician for diagnosis, treatment planning, disease monitoring, inter-patient comparisons, and image-guided surgery or intervention. In other situations, the same modality may be acquired at different temporal points spaced by days, weeks, or years to track disease response to treatment. Lastly, certain medical imaging modalities acquire near real-time timeseries data, in which the dynamic nature of the images provide functional information of the structure under investigation. Registration in these scenarios are often related to MOCO, where the series of images are registered to a reference frame to compensate for external and internal motion. Indeed, misalignment is inevitable. Whether tied to the different spatial domains in multimodal situations, to the anatomical changes due to disease evolution in unimodal cases, or to basic patient movement and functional organ displacement during temporal data acquisition, deformations are prevalent and at worst obviate interpretation and at best reduce analysis precision if left uncompensated.

A prototypical image registration pipeline, illustrated in Figure 2.5, is typically composed of three components : 1) the transformation model between the source and target images, 2) a similarity metric (also-known-as a cost function) that quantifies the alignment quality between the source and target images to guide the 3) optimization procedure used to compute the optimal transformation parameters between the source and target images.

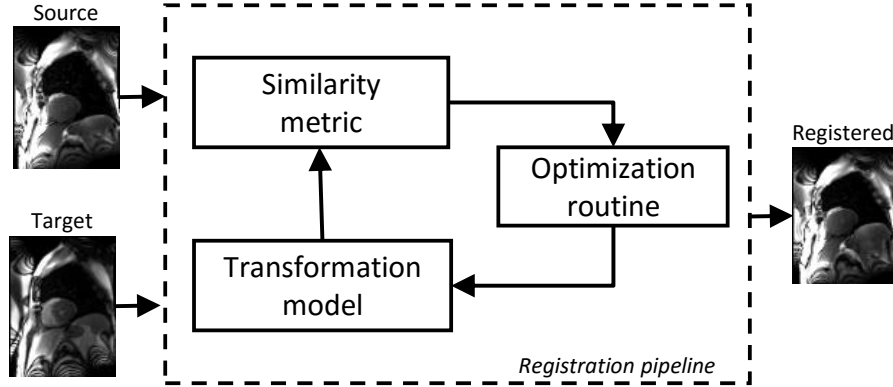


Figure 2.5 Image registration pipeline. The source image is aligned to the target image following estimation and optimization of spatial transformation parameters guided by a similarity measure.

2.3.1 Transformation models

Earlier applications typically considered rigid transformations, where translation, rotation, scale, and shear parameters were estimated [255, 263]. Although useful for correcting calibration differences between modalities or coarse geometrical transformations [158], this type of transformation model fails to handle the complex deformation profiles of biological tissue. Indeed, the human body does not abide to rigid displacements or even approximate affine deformations [98]. The field has thus evolved to nonrigid/nonlinear approaches, which are inherently more complex due to the high degrees of freedom and smoothness constraints of the deformation estimates. In nonrigid approaches, the anatomical context must be considered, as one would not expect the heart, brain, or liver to undergo the same type of displacement. The clinical setting (real-time interventional imaging vs. offline analysis) in which the system is to be used must also be taken into account as the computation times of nonrigid techniques are inherently prohibitive. This is a substantial drawback in terms of clinical applicability [253], but nonetheless offers interesting engineering problems [253].

Elastic models were some of the first used in nonrigid applications [11]. The source image is considered an elastic object that is deformed following the Navier-Cauchy partial differential equations and guided with an image similarity measure. The image is deformed until an equilibrium of the forces is reached. Their basic formulation is biased towards local deformation modeling, so they are typically used after a global initialization step, commonly referred as the *plastic* model.

Radial basis functions (RBF) constitute some of the most popular families of nonrigid interpolation techniques used primarily in conjunction with landmark-based approaches (explored in Section 2.3.2). The basis functions are tied exclusively to the distance between corresponding points of the images and the final transformation is usually a weighted average of these, which can include Gaussian, quadratic, or splines, to name a few. In spline models, matched landmarks positions between source and target are considered control points and are used in a function to define correspondences away from these points. Thin-plate splines [22, 206] have been investigated extensively, but are hindered by the fact that each control point has a global influence on the transformation and may thus perturb all other points in the transformed image. These may not be suitable to model small, localized deformations. B-splines, however, are defined exclusively in the proximity of the control points and thus afford generalized applicability and computational efficiency. They are often used as weighted basis functions in the free-form deformation (FFD) model [216], which interpolates any position on a curve from control points that influence its shape. Although the FFD affords smooth local deformation, preservation of topology is not guaranteed and its modeling complexity requiring high computational power may be a roadblock in certain situations [102].

2.3.2 Registration methods

Registration techniques are classified as either extrinsic or intrinsic. In the former, physical objects are attached to the structure undergoing imaging, such as markers glued to the skin [70] or screw-mounted tags [142, 77]. Although useful in certain medical contexts such as brain or orthopedic surgery, their intrusive nature heavily constrains their use. The large body of work of medical image registration is thus focused on intrinsic, data-driven methods, where the information contained in the recorded images such as : 1) geometrical landmarks ; 2) the pixel/voxel intensities ; or 3) a combination of both are used to infer the deformation between target and source.

Landmark-based approaches

Landmark-based correspondences are typically high-level descriptors of specific geometrical points [58, 4], contours [145], surfaces [8], or curves [34, 269] at salient image points such as line terminations, gravity centers of closed surfaces, and *meaningful* physiological components. They are generally useful when anatomical structure appearance remains relatively consistent but image intensity information is compromised, as is the case, for example, in certain pathologies encountered in retinal registration applications [228]. Locating reliable features between the images is an open problem and an active field of research [284] as its performance can be sensitive to the magnitude of the geometric distortion between the images, noise, blurring, photometric variability, and the textural coherence between the images [279]. Nonetheless, the use of geometrical/structural point matches maintains biological validity and affords straightforward interpretation of the transformation in terms of physiology or anatomy. We describe here popular landmark detectors capable of finding corresponding locations in the presence of large deformations or displacements of anatomical components between the source and target images.

The Harris detector [92] can be used to efficiently identify corner landmarks in images by computing their structure tensor S and thresholding $R = \det(S) - k(\text{trace}(S))^2$, where k is determined empirically. With the aim to attain certain geometrical invariance, many extensions of the Harris detector have been proposed [212, 177] and have proven to be robust to affine transformations [250, 172].

The wildly popular scale invariant feature transform (SIFT) [153], which is also robust to affine deformations is often cited. SIFT uses the difference of gaussians (DOG) to create a scale-space representation of the images where points of interest are detected at local extrema across varying scales. The SIFT descriptor at these points of interest is then formulated as gradient histograms of eight orientations, which forms vectors of 128 elements. These are then normalized to unit length to increase robustness against illumination variability. Many variants of SIFT such as PCA-SIFT [116], speeded up robust features (SURF) [15], affine-SIFT [179] and gradient location and orientation histogram (GLOH) [173] were subsequently proposed and the reader is encouraged to consult [110] for a comprehensive comparisons between them.

A fast alternative to SIFT are the histograms of oriented gradients (HOG) [55], which consider 15 orientations sampled at nine positions in a 7×7 neighborhood (Figure 2.6a). HOG descriptors are 135 elements long and can be efficiently computed using integral images. As with SIFT, these descriptors are typically robust to affine displacements, as shown in Figure 2.6b. The multi-layer, convolution approach by [261] extends the formulation to nonrigid es-

timations by using a hierarchical, bottom-up approach modeling locally rigid transformations at small local patches that are aggregated into nonrigid deformations at higher levels of a multi-scale decomposition of the images. The patch-based formulation of this technique also allows it to handle image regions with weak or sparse textural information.

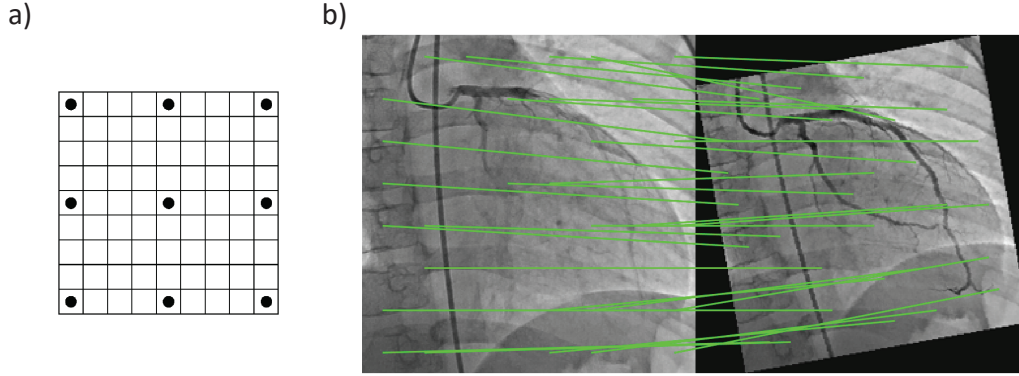


Figure 2.6 Histograms of oriented gradients : a) The HOG descriptor is formed by sampling nine equidistant points in a 7 x 7 neighbourhood, b) HOG point matches of sequential end-diastolic angiographic frames. The second frame was rotated and rescaled artificially to demonstrate affine matching performance.

Matching the detected landmarks between the images is performed by a measure the similarity of their descriptor vectors and/or by considering geometric constraints [42]. In the former case, the Euclidean distance between the vectors is often used to rank matching candidates, where different thresholding schemes are then applied to filter weak matches [173]. These strategies are simple and efficient to compute, but may intuitively be enhanced by also considering geometric constraints. Graph matching is thus used to incorporate structural relationships, where matches preserve pairwise geometry [143, 19, 249].

As matches between the images are established to a satisfactory descriptor *closeness* and/or geometrical constraint, nonrigid transformation maps can be computed using an interpolation strategy such as splines [203, 128], RBF [281, 278], or FFD [136, 102], to name a few. Although well suited in certain applications, these interpolation schemes present a major caveat of landmark-based registration : the sparsity of matches, which is often found in practice. This leads to poor interpolation quality inside the interstitial space between matches as it decreases proportionally to the distance between landmarks.

Intensity-based approaches

Matching intensity patterns between the source and target images commonly define a similarity measure using a mathematical or statistical metric such as mean squared differences (MSD), sum of squared differences (SSD), or correlation. This class of registration expects that these metrics will be optimal when alignment converges. Intensity-based schemes thus assume a certain dependency between the gray values of the target and source images. These metrics are defined between corresponding pixels and as such, do not take into account spatial dependencies. Further, they are sensitive to non-stationary pixel values and thus tend to decrease in precision in multimodal situations, timeseries data where intensity fluctuations can occur, or in situations where the images are corrupted by intensity distortions (e.g. the spatially varying bias field caused by surface coils in MRI image [174]). Compared to landmark-based approaches, intensity-based methods are also generally more prone to converge in local extrema and are thus better suited to tackle smaller deformation tasks. To mitigate these issues, [222] broke down the images in local segmented areas where so-called *geometrical moment invariants* were computed at difference spatial scales. The assumption was that metrics computed on regions of the images, as opposed to individual pixels, would be more robust to noise. Indeed fewer local minima were encountered in the optimization step and better accuracy was achieved. Whereas that method necessitates an explicit segmentation step, [273] use Daubechies wavelets to capture local spatial information, which obviates the need for an explicit segmentation preprocessing stage. Similarly, Gabor filters [86] may be used to capture local, spatial-frequency information of the images and have been shown to be robust in both unimodal and multimodal applications [191, 150]. For example, an optimized framework of the Gabor filters used to define *mutual saliency* was proposed by [146], and reliable locations were automatically identified to drive registration.

Entropy-based approaches using mutual information (MuInfo) [262, 255, 45, 156] as a similarity metric were found to be better suited for multimodal registration tasks [196]. The benefit of MuInfo in this context lies in its generalization and robustness to pixel intensity fluctuations. However, it is not overlap invariant, which may produce maxima despite misalignment. Normalized mutual information (NMuInfo) was thus introduced to address this shortcoming [229]. As with the linear metrics, information theoretic measures are based on single pixel joint probability models and may fail in certain situations, notably when shading artefacts are present in the images. As such, regional patches may be used to alleviate this problem. [43] thus introduced the regional mutual information (RMuInfo) metric using a weighted sum of local computations of MuInfo. [231] followed a similar approach by first decomposing the images into homogeneous regions, where MuInfo was then used.

Optical flow (OF) [192, 12, 159] may also be used in image registration schemes. Spatial registration and OF estimation are closely related problems. OF is typically used to estimate spatial deformations over a series of images at different time points, but used diminutively between only two images, the paradigm is similar to the approaches presented so far. Using OF as an image registration task is advantageous as it leverages more than two decades of refinement of this nonrigid displacement estimator. Notable contributions include the approach by [197], who upgraded the classical variational Horn & Schunck OF model [99] to allow discontinuities in the displacement field and to add robustness to changes in pixel intensity with their *total variation* regularization data term. [276] devised an OF formulation including a so-called *inversion consistency* procedure to ensure stable alignment quality, as argued in [41]. The idea was to symmetrically deform each image into one another until both match their counterparts original appearance.

Variational OF approaches utilize local optimizations and are initialized to a zero-motion flow field. This leads to accurate description of fine motion, but will inherently under estimate large deformations. On the other hand, the coarse-to-fine warping scheme proposed by [29] is an important innovation to the variational OF model as it initializes motion estimates at coarser resolutions, which captures the large deformation profiles present between the images and is then sequentially refined by accumulating the estimates at progressively finer scales. This technique is suitable when the deformation of small structures are similar to the large ones, but fails when the relative motion of a small structure is larger than its own scale. In these situations, the displacement estimate is biased towards large deformations. This approach was successfully applied to register CT lung volumes [65], where the anatomical structures imaged (the lung cavities) were relatively large and coarse.

There is thus a conundrum related to OF methods : whereas variational approaches are biased towards fine scale displacement estimates, they fail to accurately capture large deformations. Conversely, coarse-to-fine warping schemes are well suited to compute large displacements, but they are not appropriate when small structural motion estimates are required. A hybrid solution to this problem was thus proposed in the form of large displacement optical flow (LDOF) [28] and is presented in the following section.

Hybrid approaches

Intuitively, combining landmark and intensity information for the registration process may lead to better robustness in situations where large and small deformations are present. The two approaches can be used serially, where landmark-based registration initializes an intensity-based refinement step. Such is the case in [40], where anatomical landmarks were

used to correct large deformations and an intensity-based fluid registration scheme was then applied to finalize the alignment. The authors thus leveraged the coarse registration power of the landmark approach and the fine tuning capabilities of the nonrigid intensity-based scheme. Some methods combine both types of approaches into a single similarity measure. For example, a metric was constructed using the difference of MuInfo computed between intensity information and the pairwise distance between matching landmarks [208]. The pair and smooth hybrid algorithm (PASHA) algorithm [32] enhances this formulation by introducing a global smoothness term to mitigate the risk of local extrema in both landmark and intensity sub-metrics. In [95], landmarks were used as spatial constraints in parallel to an intensity-driven nonrigid registration scheme.

Hybridizing OF can be achieved by incorporating the large displacement estimation capabilities of landmark correspondences into the precise, dense deformations flow fields produced by the variational model. In essence this can be regarded as a combination of discrete optimization for the landmark matches coupled with continuous optimization to provide subpixel displacement accuracy. The integration of landmark information can also be beneficial in situations where structural contrast is low. In these cases, the use of variational OF alone may fail as gradients are weak, but are well managed when point matches are introduced as these guide the variational model during displacement estimation [28]. Evidently, robust point matching algorithms must be used so SIFT or HOG descriptors are obvious candidates. However, HOG landmark matching has the advantage of greater computational efficiency and is less prone to produce false matches. The LDOF process is described below :

Given two images to be aligned $I_1, I_2 : (\omega \subset \mathbb{R}^2)$ and a point in the image domain $\omega : \mathbf{x} := (x, y)^T$, the optical flow field $\mathbf{w} := (u, v)^T$ is given by the energy :

$$E_{color}(\mathbf{w}) = \int_{\omega} \psi(|I_2(\mathbf{x} + \mathbf{w}(\mathbf{x})) - I_1(\mathbf{x})|^2) d\mathbf{x} \quad (2.1)$$

where $\psi(s^2) = \sqrt{s^2 + \epsilon^2}$ is a robust function to mitigate occlusions. Equation 2.1 penalizes deviations from the assumption that corresponding points should have the same intensity, but this is seldom encountered in practice so a gradient constrain invariant to additive illumination is defined :

$$E_{grad}(\mathbf{w}) = \int_{\omega} \psi(|\nabla I_2(\mathbf{x} + \mathbf{w}(\mathbf{x})) - \nabla I_1(\mathbf{x})|^2) d\mathbf{x} \quad (2.2)$$

Equations 2.1 and 2.2 match relatively weak features (intensity and gradient), and may result in non-unique solutions. A regularization term applied to the computed flow fields can thus

be introduced :

$$E_{smooth}(\mathbf{w}) = \int_{\omega} \psi(|\nabla u(\mathbf{x})|^2 + |\nabla v(\mathbf{x})|^2) d\mathbf{x} \quad (2.3)$$

The variational optical flow model is thus given by :

$$E(\mathbf{w}) = E_{color} + \gamma E_{grad} + \alpha E_{smooth} \quad (2.4)$$

where γ, α are tuning parameters. The hybridization of this model is achieved by adding a landmark correspondences energy term :

$$E_{match}(\mathbf{w}) = \int \delta(\mathbf{x}) \rho(\mathbf{x}) \psi(|\mathbf{w}(\mathbf{x}) - \mathbf{w}_1(\mathbf{x})|) d\mathbf{x} \quad (2.5)$$

where $\mathbf{w}_1(\mathbf{x})$ is a correspondence vector constructed by landmark matching at a given point \mathbf{x} , $\delta(\mathbf{x})$ is a binary variable indicating the presence of a descriptor match, and ρ is a matching score related to the distance between matched landmark descriptor vectors. The task of discrete descriptor matching can be formulated in a continuous approach to make it compatible with the variational model :

$$E_{desc}(\mathbf{w}) = \int \delta(\mathbf{x}) |\mathbf{f}_2(\mathbf{x} + \mathbf{w}_1(\mathbf{x})) - \mathbf{f}_1(\mathbf{x})|^2 d\mathbf{x} \quad (2.6)$$

where $\mathbf{f}_1(\mathbf{x}), \mathbf{f}_2(\mathbf{x})$ are the fields of feature vectors in I_1, I_2 . The full LDOF model can thus be represented as :

$$E(\mathbf{w}) = E_{color}(\mathbf{w}) + \gamma E_{grad}(\mathbf{w}) + \alpha E_{smooth}(\mathbf{w}) + \beta E_{match}(\mathbf{w}, \mathbf{w}_1) + E_{desc}(\mathbf{w}_1) \quad (2.7)$$

The properties of LDOF are particularly interesting for medical image registration as the issues this model addresses are often found in multimodal registration problems or in dynamic sequences where both large and small motion between the frames are expected, variations in pixels intensities due to contrast agent transit is observed, and reasonable global differences in appearance are encountered. As such, this technique was thoroughly explored in Chapter 4 as the basis for a MOCO framework.

2.3.3 Reduction to unimodality

When substantial textural differences between the images are present, as is often the case for multimodal applications, a reduction to unimodality may be advised. The general idea is to map both images to a third domain that reduces diverging information between the images and thus allows *easier* deformation estimations.

A common approach is to exploit the image gradients as anatomical borders typically correspond to regions of intensity changes, regardless of the modality. [89] used this approach to register T1 and T2 weighted brain scans by mapping the images to an intermediate domain of normalized intensity gradient fields, which mitigates possible gradient intensity variability between modalities and theoretically encodes only geometrical information. Similarly, [30] defined an *edgeness operator* to map the images to a common domain by encoding local edge variance. A multi-scale genetic optimization scheme was then used to drive an affine registration step. The local and texture information encoded by Gabor filters have also been used to transform the images. [150] used the local phase gradient of the most responsive Gabor filter output to a mapping domain robust to local edge strength and contrast variance between the images. Extensions to this approach were performed by [108], who used local frequency maps, and [191], who represented the images by a rich Gabor feature descriptor vector and minimized the distance between the vectors of both images. [93] also used descriptor vector matching by encoding similarities between neighboring patches.

Information theory was used by [257] to derive an intermediate structural representation of the images, where local entropy of a patch region around each voxel was used to assign a new intensity value. They also experimented with manifold learning using Laplacian eigenmaps to extract structural information from the images. This representation produced good registration performance, at the cost of higher computational complexity, whereas the entropy-based method was simple to compute but produced slightly poorer alignment.

Finally, supervised learning techniques have been used to learn similarity between the images and discriminate between high and low scoring values [141]. This technique was used by [27] to map the images to a Hamming metric space encoding corresponding and non-corresponding locations and was subsequently extended to 3D deformation tasks [170].

The plethora of medical image registration techniques reflect its caveat of data-dependence. Approaches are often tied to the modality, image characteristics (SNR, domain, information sparsity), and anatomical structure under consideration. The type of deformation (rigid vs. nonrigid, large vs. small) is also a determining factor in choosing the appropriate technique. However, the hybrid approach paradigm discussed above shows promise as its coverage of

a wide range of nonlinear motion make it particularly interesting to investigate for highly dynamic regions, given that adequate image preprocessing steps in the form of filtering, enhancement, or reduction to unimodality are applied.

2.4 Segmentation of vascular structures

The driving force behind the proliferation of vascular segmentation algorithms is due in part to their potential as a decisive clinical diagnostic tool. The enhanced visualization and parametrization of the vessels play an important role to assess various pathologies. Markers such as tortuosity, reflectivity, abnormal branching, and geometrical vessel statistics can be efficiently inspected and quantified from segmented regions. A step beyond the promising clinical applications of segmenting two-dimensional vascular images is the full three-dimensional reconstruction of the vasculature. This is particularly valuable for surgery planning and instrument guidance during invasive interventions. In accordance with strict clinical requirements, the 3D reconstruction requires the precise, noise-free precursory segmentation of the 2D vessels and is thus another important factor pushing the development of the field. This section reviews general vasculature segmentation, but approaches specifically related to CA segmentation are presented in Chapter 5.

Framed in general terms, the objective is to isolate tube-like curvilinear structures from medical images. This has been a challenging area of research for the medical imaging community as issues related to segmenting vasculature are their dynamic nature (notably in the thoracic region) and the variability in vessel appearance between and within patients, where prominent factors contributing to the non-uniform characterization of vessels are intra-image illumination variations, radiographic noise, overlapping bones and organs, heterogeneous vessel contrast, and abnormal regions related to pathology.

The taxonomy of vessel segmentation approaches includes centerline extraction, appearance-based, deformable models, and steerable filters. However, this classification is difficult to clearly formulate as hybrid techniques that blend components of these different paradigms together are often introduced [122, 60]. Nonetheless, the following sections review the prominent contributions to vasculature segmentation.

2.4.1 Centerline extraction

Centerline-based techniques (also-known-as *skeletonization*) constitute an important portion of vessel segmentation approaches at both research and commercial levels. They aim to represent the vessels as a maximally thin curve equidistant from the structure’s boundaries.

Under the assumption that vessels are tubular shapes, the diameters of the segments at centerline vertices are typically computed by growing a normal vector until it reaches the vessel wall. As shown in Figure 2.7, centerline extraction affords a parametric description of the vessel comprised of centerline position (red vertex) and associated calibers (green lines).

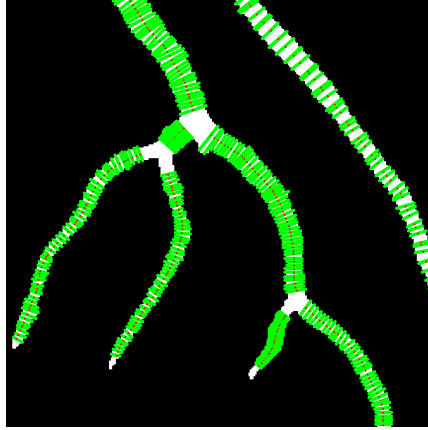


Figure 2.7 Vessel parametrization via centerline and diameter computation on segmented and binarized coronary arteries. Image by LIV4D.

Centerlines can be drawn manually by an expert [167, 9], but this inefficient process – although still used in some clinical environments – was replaced by semi-automatic methods [230, 10, 271] to reduce human interaction by requiring only the input of a segment’s start and/or end points (typically at easily identifiable landmarks such as bifurcations). Variants leveraging Markov object processes [137, 138] or coherence enhanced diffusion and Hessian vesselness [146] are notable contributions, but are hindered by erroneous cyclic centerline structures for larger-caliber vessels, low-contrast regions due to pathology, and their limitation to small curvatures.

2.4.2 Appearance-based

Of the appearance-based techniques, where a preprocessing stage is typically used to enhance vessel-like structures, digital subtraction angiography (DSA) is used as a preprocessing step in some of the more classical commercially available solutions to extract vasculature by subtracting pre (mask) and post (contrast) injected images [26, 39]. For certain anatomical regions, such as the thoracic area, spatial correspondence between the mask and contrast frames must be taken into consideration as movement will miss-align the background structures targeted for suppression. DSA-based techniques are also susceptible to sever branches that overlap radiodense structures present in both mask and contrast images. Image regis-

tration between the pre and post frames has thus been used in conjunction with independent component analysis (ICA) and region-growing [239].

Many appearance-based approaches rely on the modes of variation of the Hessian matrix [151, 211, 72] to enhance vessel-like structures [139, 259, 213, 118, 52, 235].

The Hessian $\mathbf{H}_\sigma(x, y)$ is a symmetric positive-semidefinite matrix of the second-order derivatives of the image $f(x, y)$ pre-filtered with a zero-mean, σ -variance Gaussian function $g_\sigma(x, y)$:

$$L_\sigma(x, y) = g_\sigma(x, y) * f(x, y) \quad (2.8)$$

$$\mathbf{H}_\sigma(x, y) = \begin{bmatrix} L_{\sigma,xx} & L_{\sigma,xy} \\ L_{\sigma,yx} & L_{\sigma,yy} \end{bmatrix} \quad (2.9)$$

The Hessian's eigen-analysis describes local structural information such as the principal direction of the second order image intensity variation around (x, y) , given by the three eigenvectors of \mathbf{H}_σ . The corresponding eigenvalues λ_i give the modulus of the variations in the main directions and are used to quantify a *vesselness* measure in the image.

[151] first proposed a vesselness term given by the three eigenvalues first ordered by absolute magnitude $|\lambda_1| < |\lambda_2| < |\lambda_3|$:

$$V_L = \frac{|\lambda_3| + \lambda_2}{2\lambda_1} \quad (2.10)$$

where homogeneous image areas can be thresholded out as V approaches infinity when the first eigenvalue λ_1 tends to zero.

[211] proposed a slightly more robust measure where the eigenvalues are sorted by signed value $\lambda_1 > \lambda_2 > \lambda_3$:

$$V_S = \begin{cases} \exp\left(-\frac{\lambda_1^2}{2(\alpha_1\lambda_2)^2}\right) & \lambda_2 \neq 0, \lambda_1 \leq 0 \\ \exp\left(-\frac{\lambda_1^2}{2(\alpha_2\lambda_2)^2}\right) & \lambda_2 \neq 0, \lambda_1 > 0 \\ 0 & \lambda_2 = 0 \end{cases}$$

where α_1 and α_2 are user-defined parameters adjusting for the local vessel curvature affinity (e.g. near stenotic segments).

Finally, [72] devised what was to become the standard usage methodology for Hessian-based

approaches. First, they proposed two measures corresponding to flat and blob-like structures, and a second-order *structureness* term defined respectively as follows :

$$\mathcal{S}_{flat} = \frac{|\lambda_1|}{\sqrt{\lambda_2 \lambda_3}} \quad (2.11)$$

$$\mathcal{S}_{blob} = \frac{|\lambda_2|}{|\lambda_3|} \quad (2.12)$$

$$\mathcal{S}_{struc} = \sqrt{\lambda_1^2 + \lambda_2^2 + \lambda_3^2} \quad (2.13)$$

Their vesselness measure is thus :

$$V_F = \begin{cases} 0 & \lambda_2 > 0 \text{ or } \lambda_3 > 0 \\ (1 - \exp(-\frac{\mathcal{S}_{flat}^2}{2\alpha^2}))(\exp(-\frac{\mathcal{S}_{blob}^2}{2\beta^2}))(1 - \exp(-\frac{\mathcal{S}_{struc}^2}{2\gamma^2})) & \text{otherwise} \end{cases}$$

where α , β , and γ are user-defined parameters. This formulation is more sensitive than Sato's for medium to large vessels at the cost of losing discrimination of smaller curvilinear structures. By varying the σ parameter of the Gaussian filter used in (2.8), vessels of different diameters are enhanced, but require further processing as tubular background structures and noise will also be highlighted and require post-processing [71].

Hessian-based methods tend to create discontinuities by suppressing branching or overlapping vessel points as these resemble flat areas (Figure 2.10b). Other recurring issues with these types of techniques include vessel shrinking and sensitivity to parameter selection [259].

2.4.3 Deformable models

A broad view of deformable models applied to medical imaging applications is presented in surveys by [163] and [270], but highlighted herein are the notable and widely used approaches.

The popular *snakes* formulation of deformable models are based on parametric curve elements named *snaxels* that evolve under the influences of an internal elastic force term and an external edge based force to minimize an energy criterion [112]. The external forces act as attractors to pull the curve to a targeted image feature (in the case of vessels, the boundaries are the attractors), while the internal forces constrain the curve contours' smoothness and regularity. The snakes framework is based on a Lagrangian formulation of contour evolution, which make their execution computationally efficient. Parametrically, they're represented by a set of n points : $v_i(s) = (x_i(s), y_i(s))$, where $i = 0 \dots n - 1$, $s \in [0, 1]$ and $x(s)$, $y(s)$ are

coordinate functions. The snake's energy is given by :

$$E_{snake} = \int_0^1 E_{snake}(v(s))ds \quad (2.14)$$

and can be minimized during the evolutionary phase. Equation (2.14) can be approximated by using the discrete vertices on the snake as :

$$E_{snake} \approx \sum_1^n E_{snake}(\bar{v}_i(s)) \quad (2.15)$$

Taking the derivative on both sides :

$$\nabla E_{snake} \approx \sum_1^n \nabla E_{snake}(\bar{v}_i(s)) \quad (2.16)$$

the point vector $v_i(s)$ can be iteratively adjusted by gradient descent minimization (simulated annealing can also be used as a more robust optimization technique less prone to fall into local minima) :

$$\bar{v}_i(s) \leftarrow \bar{v}_i(s) - \nabla E_{snake}(\bar{v}_i(s)) \quad (2.17)$$

The self-adapting nature of snakes make them appealing for biological structure segmentation as a priori modeling of the target region is not explicitly required. They can also be adapted to varying image scales by adding a Gaussian smoothing term in the image energy function. However, as they are governed by the energy over their entire path, they can fail to properly adapt to small contours elements representing diagnostically-relevant information. Conversely, this same property makes them robust to noise.

Applied to vessel segmentation, *Topology-Adaptive Snakes* [164] modify the original framework to allow merging and contour splitting of the evolving foreground region by a explicit re-parameterizing scheme (Figure 2.8). This proved essential to function on the tree-like structure of vasculature as distal branching and thin vessels were better handled.

[124] use piecewise cubic B-splines as their snakes' basis elements as they adapt naturally to vessel contours. This piecewise description of the splines is well suited for dynamic programming optimization, where algorithmic complexity drops from $O(n^N)$ to $O(n^4N)$ for N total control points and n possible positions. The external attractors to guide the snakes to the vessel boundaries are the responses of the so-called *stretched-Gabor* filters [94] tuned to typical vessel dimensions. Their system affords semi-automatic coronary artery segmentation and

demonstrated accurate results on select regions of proximal vessels to assess stenosis. No results were reported on branching regions or smaller, more complex vessels.

The eigen-snakes formulation by [247] first extract vessel orientations by principal component analysis of the distribution of gradient vectors. The energy term was adapted to use this information to guide the growing process. Exploiting the principal directional information lowers the false positive rate as the risk of locking on non-border elements is diminished. However, the lack of merging and branching handling proved problematic as distal segments were ignored.

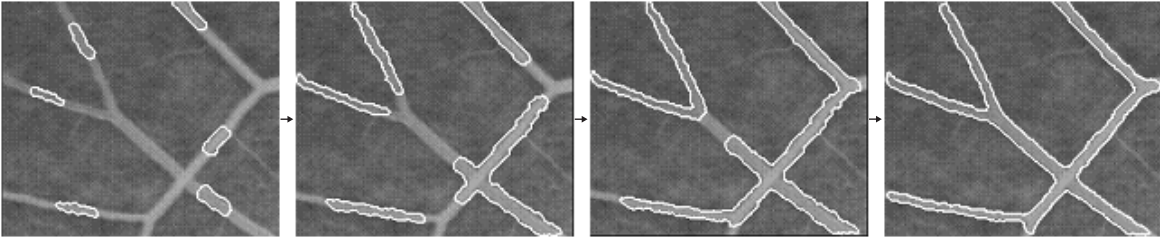


Figure 2.8 Topology-Adaptive Snakes. Merging and branching of multiple snake elements in a retinal fundus frame. Images adapted from [164].

The level-set framework [221] has arguably become the standard approach in the deformable model family of methods. They're an implicit, Eulerian formulation of active contours that evolve through partial derivative equations after seed initialization (typically performed manually). Level sets represent propagating curve fronts at a baseline, zero-level set that captures a higher dimensional function. They can thus capture and adapt to complex structures such as sharp corners during its evolution. Other advantages include their straightforward extension to higher dimensional spaces (e.g. 3D, 3D+t), and the Eulerian coordinate system lends itself well to discrete gridding and numerical approximation methods to increase operational efficiency. Variants of level-set methods have found success in segmenting vasculature.

The *Curves* method by [152] was adapted specifically for vessel segmentation by evolving a 1D curve on a 3D domain and integrating a geodesic active contour formulation [36]. They use a smoothing term that constrains the lowest curvature of the 3D domain, rather than the total curvature, which results in smoothing in only their longitudinal axes. Their edge-based formulation also implies seed initialization close to the targeted boundaries.

Based on the *Curves* approach, [252] added a explicit, region-based image term using Gaussian intensity models to segment 3D vessels of varying widths from MR angiography. Their results demonstrated an impressive level of detail in maximum intensity projection data. However, the Gaussian intensity model is intrinsically tied to contrast, which is commonly

non-homogeneous. This might predispose the wave propagation to prematurely stop at tortuous vessel regions.

Finally, a notable method by [201] proposed new geometric constraints on the contours to represent highly variable, complex structures. Their method performed well on synthetic curve patterns resembling vasculature and satellite data to segment roads from complex, natural backgrounds.

2.4.4 Steerable filters

Steerable filters allow selective control of the orientations and widths of the vessels to be extracted [73]. As illustrated in Figure 2.9, the prototypical architecture of steerable filtering involves convolving the input image with a set of rotated filters kernels known as the *basis bank* (the derivative of isotropic Gaussian kernel is typically used). The resulting line-image is then computed as the linear combination of all the filter responses. This framework can be expanded to extract lines of different widths by selecting a range of the kernel variances.

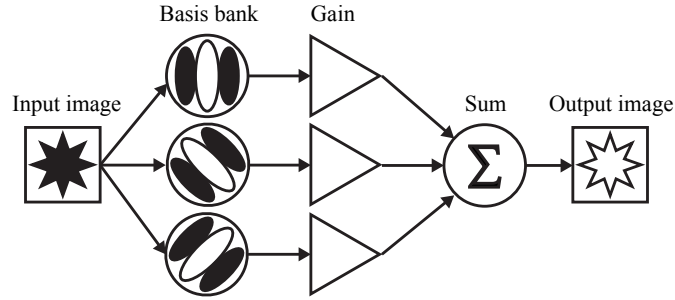


Figure 2.9 Generic steerable filtering framework. Adapted from Freeman et al. [73].

[251] used a priori directional information to enhance vessels in x-ray angiographic and retinal data. Instead of computing the Hessian's eigenvalues globally to extract curve-like structures, they first decomposed the image into oriented components using a *decimation-free directional filter bank* [13]. The directional images were then processed to remove non-uniform illumination using homomorphic filtering [265]. Applying these filters at this stage had the advantage of lowering the footprint of noisy components as they were only filtered in the directed orientation and were thus of smaller magnitude. Vessel-like structure were enhanced on each directional image using Hessian eigen-analysis and subsequently combined additively. The method produced superior results compared to the Frangi algorithm with noticeably less noise amplification, continuity conservation at junction points, and an improved amount of small-caliber vessel preservation. However, the area inside the proximal (largest) vessels were hollowed-out (Figure 2.10c), which is characteristic of Hessian-based line extraction schemes

as these regions do not manifest a curvy-linear appearance and are thus *viewed* as flat surfaces. One can thus expect that this technique would fail to correctly segment aneurysms or ectasia.

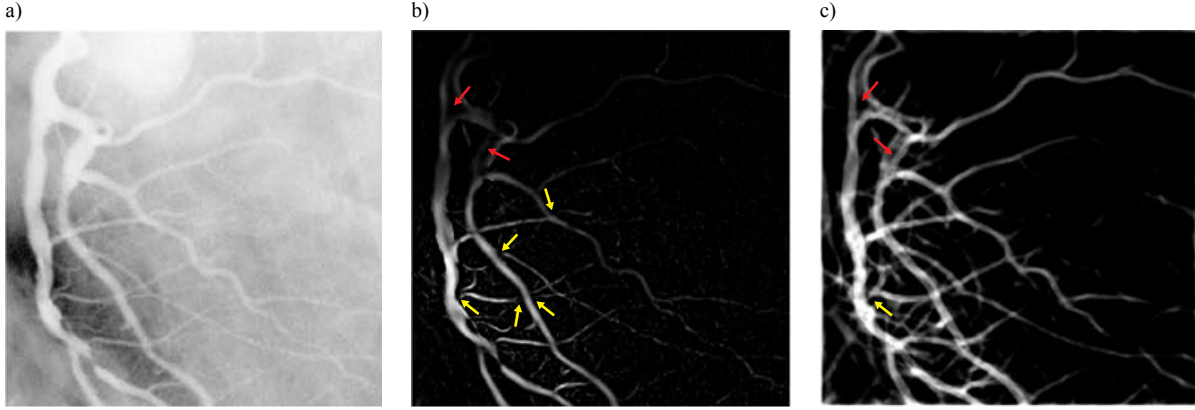


Figure 2.10 Appearance-based vessel extraction showing segment hollowing (red arrow) and tree-discontinuities (yellow arrow) : a) Original image, b) Frangi-based enhancement, c) Results from [251]. Images adapted from [251].

The use of isotropic bases can be problematic, however, when line structures cross each other or run close together, as is often the case for x-ray angiographic projections. Isotropic filtering causes close parallel lines to be smoothed together and the marginal orientation selectivity of the Gaussian kernels attenuate overlapping regions [193]. It is thus advisable to employ anisotropic Gaussian bases defined by two variance parameters [127], which are less sensitive to distorting features outside the vessels, while favoring intra-vessel information along its orientation.

Applied to vessel extraction, variants of anisotropic steerable filtering have been studied across different imaging modalities [132, 189, 53, 54, 37, 68, 67]. [131] proposed a multi-directional flux-based anisotropic diffusion applied to 3D vessel segmentation in CT liver data. Using a 3D basis composed of unit vectors in the direction of the local image gradient, and of the maximal and minimal curvatures, smoothing is enhanced preferentially in the direction of the vessel axis rather than in its cross-section. This has the effect of enhancing elongated structures such as blood vessels. Maximum intensity projection views and iso-surface renderings of the liver's vasculature were clearly enhanced as the vessel intensities were amplified and the overall noise in the surrounding tissues was attenuated. However, small vessels with poor contrast were poorly managed and were shown disconnected in the resulting images. Moreover, the algorithm requires the input of several parameters and its computational requirements are ostensibly high due to its unbounded iterative process.

The prior art illustrates the open-ended nature of the vessel segmentation problem. Most of the current methods present results on small datasets containing largely healthy vessels, and the use of statistical analysis is alarmingly scarce. Even with manual intervention, none of the approaches demonstrated satisfactory results in terms of segmentation quality and operational efficiency. Importantly, it is apparent that pathological vessel segments in the form of stenosis, aneurysms or ectasia hinders the performance of these techniques. However, anisotropic Gaussian kernels applied in a steerable filtering framework is a good candidate for vessel extraction using x-ray angiographic images. Qualitatively, they do not degrade the line edges, are not affected by overlapping segments, and are implementable in computationally efficient constructs. They are, however, sensitive to areas of wildly divergent curvilinear appearance, so a mitigated approach using post hoc correction of the ill-segmented areas is necessary and investigated in Chapter 5.

CHAPTER 3 RESEARCH HYPOTHESIS AND OBJECTIVES

3.1 General problem statement

Improving our understanding of the heart's anatomical and functional characteristics affected by certain pathology is critical to better diagnosis and treatment planing. Broadly stated, medical imaging plays a crucial role by providing tools to enhance the raw data captured from increasingly sophisticated imaging modalities. However, these systems present a number of caveats and engineering challenges. The imaging modalities described in Chapter 1, namely CMR perfusion imaging and x-ray angiography are not immune from considerable complications affecting their usability and the interpretation of the data they produce.

The main issue this thesis addresses is related to management of the spatiotemporal information present in the two modalities. In both contexts, anatomical motion is a hindererance to automatic analysis, but not all spatiotemporal information is problematic. We argue that with appropriate handling, some components of the dynamic information can be used advantageously. All things considered, we thus postulate our general research question :

General research question : *Can appropriate management of spatiotemporal information present in CMR perfusion imaging and x-ray angiography ultimately improve clinical metric extraction in terms of precision, objectivity, and ergonomics ?*

3.1.1 CMR perfusion imaging

In the case of CMR perfusion imaging, the use of high precision pixel-wise quantification of myocardial perfusion requires a stringent alignment of the anatomical structures present throughout the recorded series. Motion is partially mitigated by patient breath hold for the duration of the recording period (typically lasting 60 seconds per series). However, apnea can be taxing for myocardial infarct patients, especially in those with co-morbidities such as dyspnea, arrhythmia, or atrial fibrillation [195]. Breath-holding is thus often incomplete and can result in respiratory gasps, which induce large, striking displacement events in the acquired images. Conversely, while free-breathing protocols improves patient comfort, they introduce pseudo-periodic thoracic movement throughout the acquired series. Electrocardiogram gating is also used during acquisition to synchronize the geometrical phase, but may present errors, especially under stress conditions or in patients with certain pacing pathologies. This results in small residual myocardial motion, but is nonetheless detrimental for precise quantification.

Other than the motion issues in CMR perfusion imaging, the varying appearance of the images it produces as different sequence configurations and magnetic field strengths are used is also a challenging issue that must be taken into consideration. Likewise, the use of auxiliary series, as beneficial as they are for enhancing quantification when they are aligned to the perfusion images, are inherently different in terms of photometric, resolution, and SNR characteristics.

Both the large and subtle nonlinear deformations found in CMR perfusion and auxiliary series, in addition to the requirement of compatibility to the range of sequence types, each with unique appearances, point to the use of a hybrid registration techniques, as explained in Section 2.3.2. The application of landmark matching can potentially handle the large displacements caused primarily by patient gasping, breathing, and guttural movement. Coupled with the fine scale registration capabilities of an intensity-based registration scheme to manage the residual nonrigid deformations of the myocardial tissue, it would seem appropriate that the LDOF formulation be further investigated and adapted to CMR perfusion imaging. As such, we postulate our first hypothesis :

Hypothesis 1 : *CMR perfusion quantification can be enhanced using an adaptation of large displacement optical flow as the engine of a processing pipeline to compensate for motion and register different types of sequences together.*

Objective 1.1 : Devise an appropriate preprocessing procedure to normalize textural variability while enhancing structural information between the T1-weighted perfusion and AIF sequence types for universal applicability of the LDOF engine.

Objective 1.2 : Establish a processing order strategy amenable to multithreaded architectures.

Objective 1.3 : Determine the optimal intra-series reference image to which the rest of the frames will be aligned to. Automate this process.

Objective 1.4 : Implement the LDOF formulation to compute deformations between sequential frames of T1, AIF, and PD series.

The registration of the inherently different PD images to the T1-weighted frames can arguably be considered multi-modal in practice. Although the landmark-matching component of the LDOF formulation may find suitable correspondences between the two types of sequences,

the variational component will likely be hindered by photometric and textural incongruencies. Hence, in order to use an LDOF-based approach, a reduction to unimodality is proposed, where surrogate images used to lower the appearance divergences between the images can help the LDOF engine during registration.

Objective 1.5 : Formulate bridge images for both PD and T1-weighted images that primarily encode their respective structural components, matches their photometric properties and minimizes intrinsic textural information.

Objective 1.6 : Devise a strategy for the LDOF engine to register the PD and T1-weighted images through their bridge surrogates.

3.1.2 X-ray angiographic imaging of coronary arteries

The traditional gold-standard diagnostic protocol for CAD involves selective angiographic recordings. The clinician’s goal is to identify and characterize anomalous vessel regions by taking multiple views of the arterial tree around the patient. However, the complex structure of abnormal CA segments is difficult to interpret from the two-dimensional x-ray angiographic projections. This problem is highlighted while stratifying stenosis or thrombogenesis risk in aneurysms and ectasia, where blood flow is affected by the pathology’s impact on vessel geometry [59, 217]. Current clinical operating procedures call for manually measured vessel statistics by technicians, but this time-consuming, routine practice is susceptible to human and procedural variability [97, 182, 66], which can lead to erroneous diagnosis, misguided treatment planning, and stresses hospital resources in terms of staff time and data management.

Automatic CA segmentation from x-ray angiographic series can be used as a powerful pre-diagnostic step as it affords an objective parametric description of the vessels. However, the segmentation problem is open ended. As explained in Section 5.2, the issues complicating high quality vessel extraction originate from the variability in vessel appearance between and within patients. The main factors contributing to the non-uniform characterization of vessels are intra-image illumination variations, radiographic noise, overlapping bones and organs, heterogeneous vessel contrast, and abnormal vascular regions related to pathology. Indeed pathological vessel segments in the form of stenosis, aneurysms or ectasia hinder the performance of current segmentation techniques.

The dynamic nature of the thoracic and heart regions often labels them the most difficult anatomical structures to tackle from a segmentation point of view. As such, most segmenta-

tion systems only consider a single static frame for processing. However, we believe not all of the dynamic information is obtrusive. Indeed, the spatiotemporal information produced by the propagation of the contrast agent through the arterial tree contains features seldom used for delimiting the vessels. However, the large displacements caused by patient breathing and myocardial motion incurs nonrigid deformations of the arteries while bolus is transiting and will render this type of analysis imprecise. As such, we postulate our second hypothesis :

Hypothesis 2 : *Motion compensation of the angiographic series coupled with the spatio-temporal tracking of the radiodense contrast agent transiting through the arterial tree can be used to eliminate background information and further isolate the targeted vascular structure.*

Objective 2.1 : Implement filters adapted to tackle the specific statistical distribution of radiographic noise, while retaining anatomical structure fidelity.

Objective 2.2 : Normalize intra-frame illumination variability to mitigate large superposition artefacts causing shadowing, while retaining adequate contrast in the vessel regions.

Given adequately filtered and normalized angiographic images, the vessel extraction scheme must be adaptable to various recording conditions, be computationally efficient, and importantly, must preserve the appearance of vessels of varying widths. As such, the anisotropic Gaussian class of steerable filters offers desirable properties such as orientation and scale selectivity in addition to their separable nature, which can significantly lower computational complexity. However, their robustness to pathological areas such as aneurysms must be improved.

Objective 2.3 : Implement a separable anisotropic filtering scheme with adjustable scale and orientation tuning parameters.

Objective 2.4 : Implement an automatic post-hoc pathological region correction routine to compensate for the filter's deterioration of lesions such as aneurysms or ectasia.

Objective 2.5 : Adapt the LDOF motion compensation framework described in Chapter 4 to angiographic sequences.

Objective 2.6 : Track the spatiotemporal propagation of the contrast bolus through the arterial tree of the motion corrected angiographic images.

Objective 2.7 : Delimit the principal bolus propagation zones and use this information to mask non-vessel structures.

Objective 2.8 : Implement a routine to automatically compute CA calibers from the segmentation result.

3.1.3 Coronary artery distensibility assessment via angiographic series

As mentioned earlier, automatic segmentation affords the objective quantification of vessels, where their diameters are the primary metric used for clinical decision making. However, these are most often measured on a single frame, thus discarding the wealth of dynamic information contained in the angiographic series. In addition, normal appearance and measures of vessels on angiographic images may not show underlying wall pathologies. Vessel distensibility, however, may be used as a potentially valuable metric to assess early disease onset and long term vascular sequelae. In the spirit of the previous hypothesis, we believe the spatiotemporal information contained in the angiographic series may again be used to ultimately extract clinically meaningful information. As such, we postulate our third and final hypothesis :

Hypothesis 3 : *The temporal tracking of the coronary artery calibers may be used to estimate apparent vessel wall distensibility.*

Objective 3.1 : Create a user interface where the operator is presented with the angiographic frame containing the most apparent amount of contrast agent and is able to draw a region of interest (ROI) on a target vessel segment.

Objective 3.2 : Use the segmentation result of the arterial tree to identify vessel wall pixels.

Objective 3.3 : Implement a pixel tracking scheme using the HOG framework to identify corresponding vessel wall pixels from one frame to another over a complete cardiac cycle.

Objective 3.4 : Compute the vessel segment diameters at each tracked frame, producing a *caliber vs. time* curve.

Objective 3.5 : Extract distensibility-related metrics from the computed *caliber vs. time* curve.

3.2 General methodology

To reach the objectives and verify the hypotheses presented above, we propose a methodology presented in Chapters 4, 5, 6 to address concurrent and specific issues related to both CMR perfusion and x-ray angiography imaging. At a high level, the development process followed the workflow depicted in Figure 3.1.

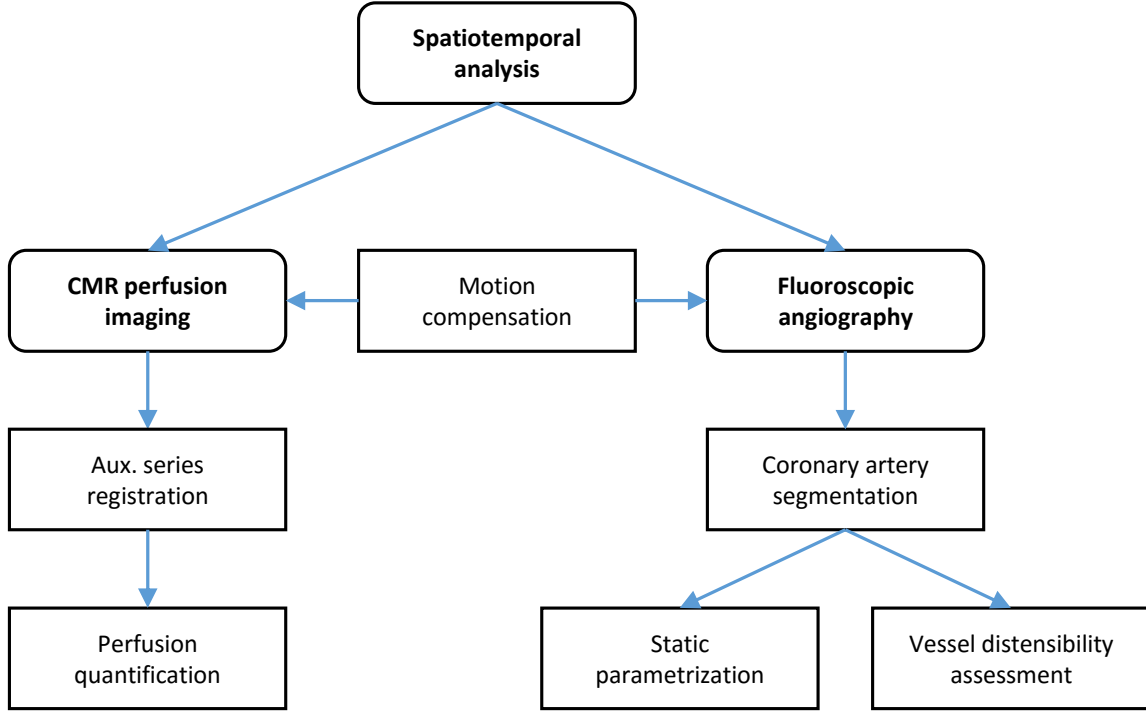


Figure 3.1 Development plan stemming from spatiotemporal analysis addressing the issues encountered in CMR perfusion imaging, x-ray angiography, and the application of coronary artery segmentation to static vascular parametrization and distensibility assessment.

3.2.1 Phase I - CMR perfusion imaging

High precision perfusion quantification requires stringent anatomical alignment of the T1-weighted series and registration of the auxiliary images. Chapter 4 presents how we have

adapted the LDOF formulation into a universal CMR perfusion motion correction and registration process by specifically addressing the appearance, photometric, and structural variability encountered within and between the sequence types and field strengths commonly used in clinical settings. First, the intra-series appearance of T1-weighted, PD, and AIF series were normalized by compressing the dynamic range and textural information prone to noise and MRI artefacts, which resulted in increasing the underlying anatomical information undergoing movement. The LDOF engine was then tuned to take advantage of the enhanced structural regions by balancing the HOG landmark matching term robust to large displacements with the variational smoothness and gradient constancy terms to address the fine-scale elastic deformations of the myocardium. This process was designed into a parallel processing framework that can scale favorably in multithreaded CPU architectures. Importantly, global post-hoc photometric correction ensured that the perfusion quantification does not diverge from manually measured signals. This general approach was tested using two similarity metrics, namely Pearson’s correlation and mutual information computed on full resolution and myocardial region crops of sequential frames.

The registration of the PD auxiliary series to the T1-weighted perfusion series followed a reduction to unimodality paradigm. Bridge images were used as proxies of both types of series that primarily encoded structural and photometric properties within and between the image types. The landmark matching term was positively biased under the assumption that structural saliency was of critical importances. Quantitative tests then evaluated the alignment improvement after registration for each type of PD-T1 configurations using the same similarity metrics mentioned above.

The proposed system was tested on cohort of 291 clinical subjects encompassing a wide range of pathological severity under routine clinical protocols and recording conditions encountered throughout North America and abroad.

3.2.2 Phase II - X-ray angiography

The diagnosis of CAD in both adult and pediatric populations calls for enhanced visualization and objective quantification of the CA acquired using the current gold standard of x-ray angiography. Automatic and efficient segmentation of the CA can address this by offloading the operator task of measuring vessel diameters manually. In Chapter 5, we propose a coronary artery segmentation approach leveraging the spatiotemporal propagation of the radiodense contrast agent through the arterial tree. Prior to tracking this propagation using an optical flow formulation, the motion of the anatomical structures between the cardiac-gated frames was compensated using the MOCO system developed in Phase I. Adequate noise filtering

using dual-tree complex wavelet transforms and photometric normalization were then used to preprocess the images to enhance curvilinear structure extraction using anisotropic Gaussian filtering. The primary radiodense propagation regions were used to construct a *motion mask* to isolate the arterial tree from background elements. A post-hoc aneurysm detection routine then corrected for ill-segmented regions. Finally, an automatic diameter measuring scheme applied to the segmented vessels was implemented to parameterize the arterial tree.

The evaluation of this proposed approach was conducted on 62 angiographic sequences of 31 pediatric patients with healthy vessels and KD-related arterial lesions such as aneurysms and ectasia. The primary performance evaluation was vessel caliber fidelity assessed by comparing the automatically measured values with those produced by manual and semi-automatic commercial platforms operated by independent specialists.

3.2.3 Phase III - Pilot studies of CA distensibility

The final phase of this thesis presents, in Chapter 6, preliminary results of two clinical studies evaluating CA wall health by measuring its distensibility over a complete cardiac cycle. To do so, the automatic coronary artery segmentation pipeline developed in Phase II was used to identify vessel wall pixels in an operator-selected region. These features were automatically tracked from frame-to-frame and the average caliber of the segment was extracted. Various metrics computed from temporal variability of the calibers over the cardiac cycle were then used as a measure of apparent arterial distensibility.

As a pilot study, the distensibility characteristics of healthy and KD patients were compared. The KD patients were classified in terms of their history of aneurysmal lesions to their CA. Statistical tests were then performed to evaluate coronary health differences between the groups using the distensibility metrics. In a follow-up study, distensibility metrics were regressed according to a score formulated using invasive OCT observations on an extended cohort of KD patients. The noted lesions included the presence of hyperplasia, media destruction, fibrosis, and calcification.

CHAPTER 4 Article 1 : A ROBUST UNIVERSAL NONRIGID MOTION CORRECTION FRAMEWORK FOR FIRST-PASS CARDIAC MAGNETIC RESONANCE PERFUSION IMAGING

Mitchel Benovoy^{1,2}, Matthew Jacobs^{1,4}, Farida Cheriet², Nagib Dahdah³, Andrew E. Arai¹,
Li-Yueh Hsu¹

1 : National Heart, Lung and Blood Institute, National Institutes of Health, Bethesda, USA.

2 : Department of Biomedical Engineering, Polytechnique Montreal, Montreal, Canada.

3 : Sainte-Justine University Hospital Research Center, Montreal, Canada.

4 : Department of Electrical Engineering and Computer Science, Catholic University of America, Washington DC, USA.

4.1 Abstract

4.1.1 Background

The goal of quantifying first-pass dynamic contrast-enhanced cardiac magnetic resonance (CMR) imaging at the pixel level calls for greater precision of nonrigid motion correction methods. Variability of acquisition parameters such as sequence types, field strengths, breathing paradigms, pixel resolutions and dynamic image contrast changes must be taken into consideration.

4.1.2 Methods

We propose an automatic nonrigid image registration framework to correct motion in CMR perfusion series acquired under a wide range of conditions. Our method combines discrete feature matching for large displacement estimation with a dense variational optical flow formulation in a multithreaded architecture to significantly reduce motion and computational time. This framework can be applied to standard dynamic contrast myocardial T1-weighted images, low resolution arterial input function (AIF) images, and proton density (PD) weighted images to facilitate perfusion quantification.

4.1.3 Results

Our evaluation on a diverse cohort of 291 clinical subjects shows the proposed framework outperforming a commercial system in terms of frame-to-frame appearance consistency, ex-

pressed in Pearson’s squared correlation coefficient ($R^2 = 0.996 \pm 3.735e-3$ vs. $0.990 \pm 8.555e-3$, $p < 0.0001$) and mutual information ($MuInfo = 3.823 \pm 4.098e-1$ vs. $3.084 \pm 4.026e-1$, $p < 0.0001$). The framework is robust to both breath hold and free breathing paradigms as well multiple imaging sequence types. The presented system is capable of registering PD frames to perfusion T1 images to improve surface coil inhomogeneity normalization and also effectively corrects motion in dedicated low resolution perfusion image series for AIF measurement. In myocardial time signal intensity comparisons, the proposed framework preserves perfusion contrast dynamics in the motion corrected images compared to the raw series ($R^2 = 0.995 \pm 6.420e-3$).

4.1.4 Conclusion

The critical step of motion correction prior to high resolution pixel-wise CMR perfusion quantification can be performed with the proposed universal system. Its robustness in processing a wide range of perfusion series and auxiliary images with different sequence parameters and contrast settings promotes its further application in routine clinical workflows.

4.2 Background

First-pass contrast-enhanced cardiac magnetic resonance (CMR) imaging is an increasingly reliable and useful diagnostic tool for diagnosing coronary artery disease [44] as its non-invasive and non-radioactive nature lends it clinical appeal. Some techniques are now able to generate pixel-wise myocardial blood flow maps for high resolution qualitative and quantitative analysis capable of differentiating transmural perfusion gradients in patients with varying severities of ischemia [101, 282]. However, despite the development and optimization of acquisition techniques and parameters, many studies are still hindered by motion of the heart and surrounding tissue during the acquisition period [215]. As perfusion analyses increasingly target individual pixel resolutions, the necessity of frame-to-frame anatomical correspondence becomes critical and has historically been performed by labor-intensive and subjective operator interaction [264, 88, 283].

The physical sources of cardiac motion are respiration, voluntary patient displacement, involuntary thoracic organ movement (typically from guttural muscle or diaphragm contraction), and the pumping action of the heart’s four chambers [215]. Of interest to perfusion cardiac imaging, the left ventricle (LV) and right ventricle (RV) present inherent motion patterns characterized by longitudinal shortening, radial contractions, and rotations. Coupled with the concomitant sources of movement surrounding the heart, cardiac motion is thus composed of

inconsistent, patient-specific rigid displacements and complex nonrigid elastic deformations. Uncompensated residual myocardial motion is detrimental to high resolution perfusion quantification. Electrocardiogram (ECG) gating is thus widely used during acquisition to synchronize the cardiac phase during perfusion imaging. Nonetheless, gating may introduce errors, especially under stress conditions or due to arrhythmias. At the acquisition stage, motion can also be partially mitigated by instructing the patient to hold their breath for the duration of the recording period (typically lasting 60 heartbeats). However, breath holding can be taxing for sicker patients [195]. Breath holds are thus often incomplete and can result in respiratory gasps, which induce strikingly large motion events in the perfusion image series. Conversely, while free breathing acquisition paradigms lower patient and clinician constraints, they introduce quasi-periodic thoracic movement throughout the acquired series which must be taken into consideration at the analysis stage. Retrospective image-based motion correction (MOCO) is therefore a critical step in the quantitative CMR perfusion analysis pipeline.

4.2.1 Motion compensation requirements

For practical clinical considerations, an ideal MOCO system must be capable of handling CMR images produced from different magnetic field strengths and sequence types which may have different signal-to-noise ratios (SNR), spatial resolutions, and contrast characteristics. As CMR perfusion series are typically acquired at three different short-axis slice locations (basal, mid-ventricular, and apical) under both rest and stress conditions, the MOCO algorithm must also be robust to diverse anatomical appearances and pacing conditions, respectively. Moreover, the compatibility with perfusion images acquired under a free breathing paradigm would be an interesting asset in terms of augmenting patient comfort and clinical applicability.

The use of auxiliary images is an increasingly important aspect for CMR perfusion image diagnosis and quantification. These include proton density (PD) weighted images, which are used to normalize myocardial intensity inhomogeneities to enhance perfusion quantification precision [100, 174]. Their appearance is inherently distinct from perfusion T1-weighted images and may be acquired using different sequence types. For example, PD-T1-weighted image configurations may include : FISP-FISP, FLASH-FISP, or FLASH-FLASH [186]. For optimal bias field normalization, intra-PD MOCO followed by PD-to-T1 perfusion series registration is required to align the anatomical structures - particularly the myocardial region - between the two types of images.

Arterial input function images are another class of auxiliary series specifically designed to maintain the linearity of the LV signal intensity during contrast bolus passage and are used

to calculate myocardial blood flow [79]. Despite their interleaved acquisition with the main perfusion images, they are differentiated by an optimized dynamic range of contrast information in the LV cavity at the cost of a significantly lower spatial resolution and lower SNR in the myocardium. These characteristics must be handled adequately by the MOCO system in order to extract the arterial input function.

This paper presents a universal nonrigid motion correction and registration scheme dedicated to CMR perfusion imaging and quantification that addresses each of the aforementioned requirements. The proposed framework is evaluated in diverse clinical perfusion studies scanned with different imaging sequences, parameters, and contrast settings. The performance of the presented approach is also compared with a commercial CMR perfusion image motion correction system.

4.3 Methods

4.3.1 Study Population

First-pass CMR perfusion images of 291 clinical subjects were evaluated in this study. All studies were performed under procedures and protocols approved by the institutional review board of the National Heart, Lung and Blood Institute (NHLBI), and all subjects gave written informed consent.

4.3.2 Image Acquisition

CMR imaging was conducted on 1.5 and 3.0 Tesla scanners (Siemens Healthcare, Erlangen, Germany) with a saturation recovery dual-sequence technique [79] based on a FISP or FLASH perfusion sequence. Perfusion studies were obtained by administering a 0.05 mmol/kg bolus of gadolinium-based contrast agent (Magnevist ; Berlex Laboratories, Wayne, NJ, USA) followed

Table 4.1 Patient numbers according to acquisition characteristics.

	Total number of patients (291)		
Perfusion Image Sequence Type	FISP (255)	FLASH (36)	
AIF Image Sequence Type	FLASH (291)		
PD-Perfusion Image Configuration	FISP-FISP (100)	FLASH-FISP (155)	FLASH-FLASH (36)
Magnetic Field Strength	1.5T (201)	3.0T (90)	
Breathing Paradigm	Breath Hold (100)	Free Breathing (191)	
Pacing Condition	Rest (291)	Stress (291)	
Slice Location	Basal (291)	Mid-Ventricular (291)	Apical (291)

by a saline flush.

Stress and rest studies were performed at three short-axis slice positions of the LV (basal, mid-ventricular, and apical) during either breath hold or free breathing for 60 heartbeats. Typical imaging parameters for perfusion imaging included : 90° composite saturation preparation pulse, 50° readout pulse, 90 ms saturation recovery time, 2.3 ms repetition time, 1.2 ms echo time, 360×270 mm field of view, 128×80 to 192×144 acquisition matrix, 192×128 to 256×192 image matrix after interpolation, 2.8×3.4 to 1.9×1.9 mm raw pixel resolution, 8 mm slice thickness, and parallel imaging factor of 2 to 3.

The low resolution AIF series were acquired at the beginning of each RR cycle at the basal location with the same field of view but a reduced acquisition matrix of 48×64 using a FLASH readout [79]. Additionally, two or three PD-weighted images were acquired prior to perfusion imaging for each slice location using either FISP or FLASH protocols with no saturation preparation pulse.

4.3.3 Motion Correction Framework

The schematic diagram of the proposed motion correction framework is shown in Figure 4.1. Briefly summarized, the system employs post-hoc warping following nonrigid displacement estimation using an optical flow formulation specifically amenable to perfusion series dynamics. The novelty of this framework lies in its robustness to process image series with varying characteristics and its ability to facilitate fully quantitative CMR perfusion analysis by its processing of auxiliary series such as PD images and independent AIF acquisitions. The implementation also features automatic reference frame and PD image detection, autonomous flow field distortion correction, and a multithreaded architecture to improve processing speed.

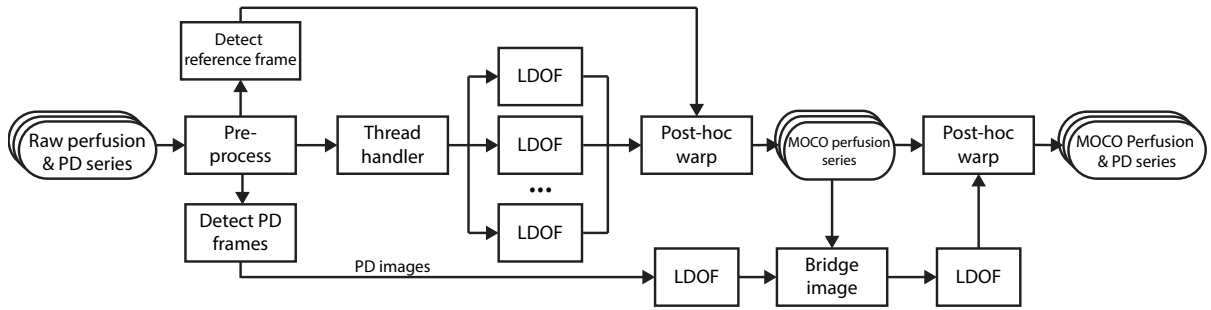


Figure 4.1 Automatic Nonrigid Motion Correction Framework. Image processing pipeline of our proposed system using a robust large displacement optical flow (LDOF) approach for first-pass CMR perfusion image series and auxiliary series.

4.3.4 Image pre-processing

A proxy copy of the raw image series was used to estimate the motion, while the full-resolution raw series is used exclusively at the later registration stages during geometrical transformations. To standardize processing parameters and optimize computation time, the proxy images are first rescaled to a default size (long dimension = 128 pixels for perfusion images, 96 pixels for AIF frames) and quantized to a lower dynamic range (8 bits per pixel). This range compression attenuates noise-prone textural information while retaining the underlying structures ostensibly corresponding to the anatomical components prone to movement. An added advantage of image dimension and intensity range reduction is the ability to use intrinsic central processing unit (CPU) primitives [23] yielding significant computational gains for the motion estimation. As the image warping after motion estimation uses the original raw frame, there is no reduction in image quality besides the natural smoothing caused by the interpolation.

4.3.5 Reference perfusion frame and PD frame detection

A reference frame is used as a template to which all other images will be registered. The optimal reference image was identified as the baseline frame immediately preceding contrast arrival in the RV. This image depicts contrast-free anatomical structures compared to the later stages, where frame-to-frame pixel fluctuations are higher and large respiration events are prone to occur under a breath hold paradigm. This frame ρ is automatically detected by first denoising the proxy series using principle component analysis (PCA) decomposition with 85% variance retention to reduce transient magnetic resonance (MR) artifacts and noise, in addition to smoothing out structural movement across the time series. Sequential neighbors of the PCA-reduced series are then cross-correlated together until a large correlation coefficient drop is detected with differential analysis, which ostensibly corresponds to the onset of contrast arrival in the RV. The PD frames preceding the perfusion T1 series are automatically detected in a similar way by identifying the abrupt correlation variation corresponding to the PD-to-T1 image transition.

4.3.6 Large displacement optical flow motion estimation

Nonrigid deformation maps between pairwise sequential frames are computed in the CMR perfusion series using an optical flow (OF) formulation robust to large displacement (LDOF) [28]. This characteristic is essential to accommodate the wide range of motion found in the perfusion series and the fast ventricular bolus arrivals without causing motion estimation

artifacts. As illustrated in Figure 4.2, the LDOF formulation couples discrete feature points tracking computed from histograms of oriented gradients (HOG) [55] with a continuous variational optical flow step [99] in a coarse-to-fine optimization scheme [29]. The HOG tracking component handles large displacements of arbitrarily moving anatomical structures, while the variational module estimates dense flow fields to measure relatively subtle deformations such as the elastic motion of the myocardial wall at sub-pixel accuracy. Both of these components are capable of estimating nonrigid motion. The LDOF engine is controlled with three primary parameters : α , the smoothness of the flow fields ; β , the weight of the HOG descriptor matching term ; and γ , the weight of the gradient consistency term. These parameters are set to aggressive default values (small α , large β and γ) automatically learned from a small subset of patients using a grid-search approach [226].

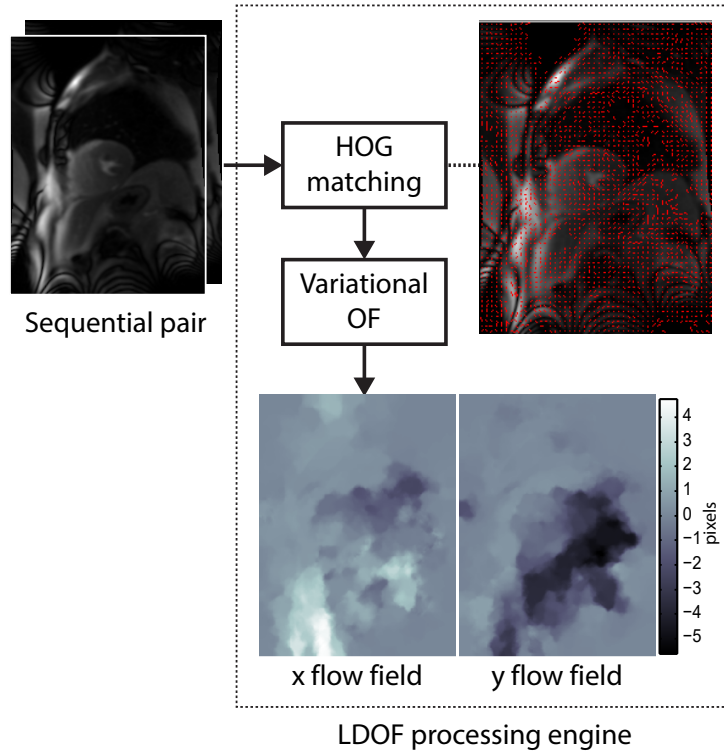


Figure 4.2 Displacement Flow Fields Computation. Longitudinal (x) and transversal (y) displacement flow fields between pairwise sequential frames are computed using an optical flow (OF) formulation robust to large displacement (LDOF). This approach couples discrete feature point tracking computed from histograms of oriented gradients (HOG) with a continuous variational optical flow step. The discrete HOG matches (red vectors) are displayed and superimposed on the first CMR image of the pair.

Instead of immediately registering the current frame before computing the subsequent motion, the stepwise x, y deformation fields $[f^x, f^y]$ of each image pair are saved for warping at a

later stage. Compared to methods that immediately register all images to a single reference frame or to consecutively registered images [272, 87, 96], this post-hoc approach has the advantage of avoiding successive smoothing caused by sequential frame-to-frame interpolation and improving the displacement estimation as the motion and appearance between adjacent frames are typically smaller and consistent. This technique is particularly well suited for perfusion CMR series that have large motion events due to incomplete patient breath holding or high tissue contrast changes during perfusion. Furthermore, as the estimation of a given flow field does not depend on pre-registered frames, the MOCO pipeline is designed as a parallel processing architecture where groups of neighboring image pairs are handled by multiple LDOF processing engines utilizing the CPU thread pool.

Despite the precautions outlined above to minimize flow field estimation errors, transient signal intensity changes from MR imaging artifacts may induce false motion estimates and distort the signal intensity and appearance of the registered frames. These flow field distortions are generally characterized by large, focal variations in the Laplacian of the $[f^x, f^y]$ fields computed from the displacement magnitudes (Figure 4.3). The system handles these disruptive errors by automatically relaxing the α and γ parameters for the contentious pair of frames when anomalies are detected using a statistical threshold. This inline correction stage minimizes possible distortion artifacts in the flow field estimation, which can severely impact the quality of motion corrected images.

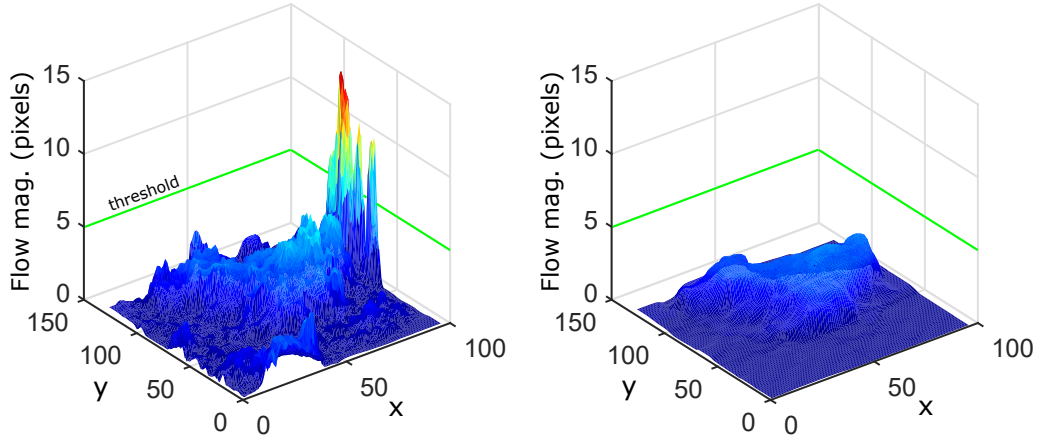


Figure 4.3 Automatic Flow Field Distortion Correction. Distorted (left) and automatically correction (right) flow field magnitudes are shown for comparison. Automatic correction is performed using statistically-determined threshold (green line).

Following the completion of motion estimation on every sequential image pair, all raw perfusion images are registered to the reference frame ρ using 2D bicubic interpolation warping

with the cumulative displacements computed from the stepwise estimates. This procedure fully resolves the pixel-wise $[x, y]$ excursions from ρ to a given image frame t :

$$[\mathbf{F}_t^x, \mathbf{F}_t^y] = \begin{cases} \sum_{i=\rho}^{t-1} [\mathbf{f}_i^x, \mathbf{f}_i^y] & t > \rho \\ \sum_{i=t}^{\rho-1} [\mathbf{f}_i^x, \mathbf{f}_i^y] & t < \rho \end{cases}$$

4.3.7 PD-to-perfusion image registration

Once motion correction for the T1-weighted perfusion images is completed, the PD-weighted images are motion corrected with respect to the last PD frame. These images are then registered to the perfusion series via two bridge images of the PD and T1 frames to match their photometric properties and increase their structural information, as shown in Figure 4.4. The T1 bridge image (I_{brT1}) is constructed by first taking the median (I_{T1}) of the motion-corrected baseline T1 frames leading up to the reference frame ρ as these are not influenced by ventricular contrast dynamics. An edge-enhanced image (I_{edgeT1}) of the I_{T1} is computed using a weighted combination of its gradient image obtained with the Sobel operator. Similarly, the PD bridge image (I_{brPD}) is constructed with the median (I_{PD}) and edge-enhanced (I_{edgePD}) images. Next, histogram equalization and unsharp masking are performed on the I_{edgeT1} and I_{edgePD} images to further enhance the anatomical boundary gradients. This is followed by exact histogram specification [47] to form the final bridge image pair. The flow field mapping I_{brPD} to I_{brT1} is computed with the LDOF process outlined above using a high gradient consistency parameter γ and a large descriptor matching weight β to emphasize the discrete HOG feature correspondence component. The resulting deformation estimation is finally applied to the motion-corrected PD images to re-register them with the motion-corrected perfusion T1 series.

4.3.8 Image post-processing

Post-processing of the PD and perfusion T1 motion-corrected images is limited to matching their photometric profiles with their corresponding raw frames using exact histogram specification [47]. This recovers the original signal intensity distributions that have invariably been altered during the 2D interpolation warping stage.

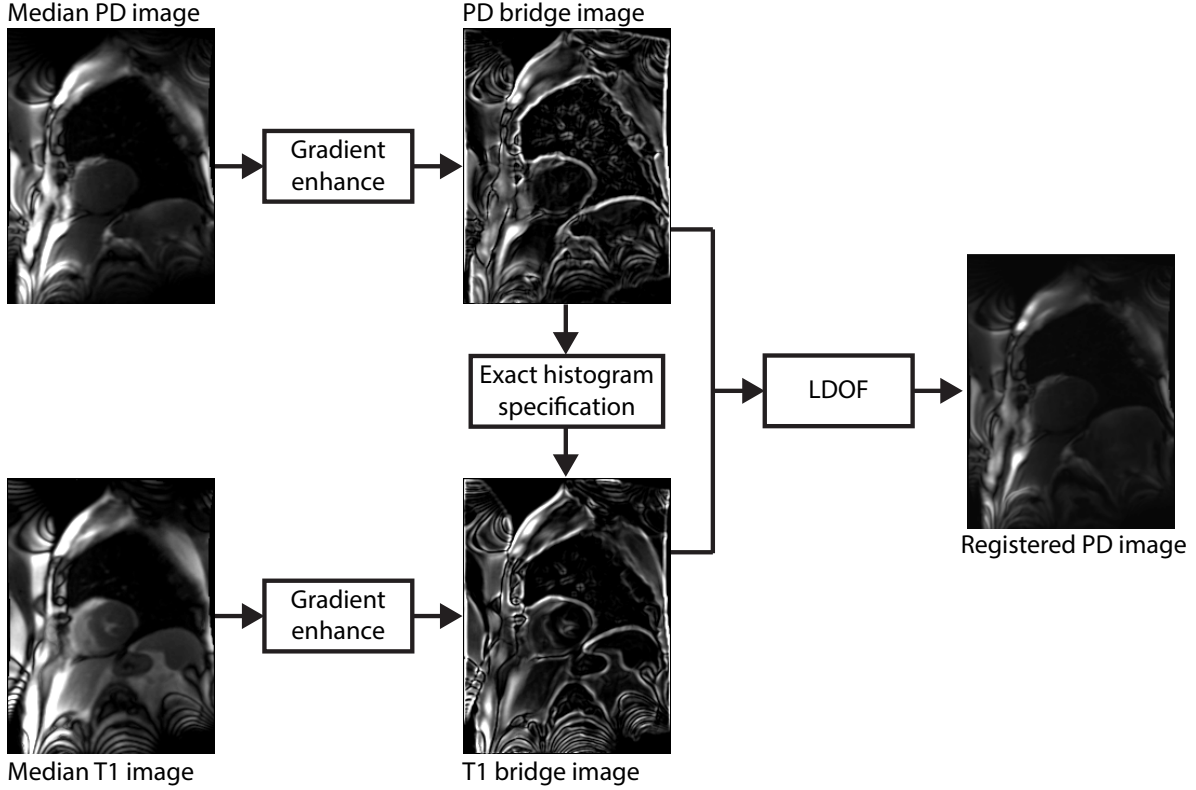


Figure 4.4 PD-to-Perfusion Image Registration. The median PD-weighted image and median T1-weighted perfusion image are computed from the series and processed to enhance gradient information and match photometric profiles. These are used as bridge images for image registration via the LDOF processing engine.

4.3.9 Performance Evaluation

The LDOF motion estimation framework was implemented in the C/C++ programming language with Intel’s (Santa Clara, U.S.A.) Math Kernel Library under Windows 7 64-bit operation system. The results of the proposed approach are labeled “LDOF-MOCO”, whereas those of the motion correction software implemented in dedicated commercial Siemens systems (Siemens Medical Solutions Inc., Malvern, U.S.A.) are termed “Siemens-MOCO”, and series without motion compensation are designated “raw”.

The comparative analyses were carried out on the full frame images as well as a square region of interest encompassing the RV, LV and myocardium (henceforth labelled “heart region”) that is automatically delimited using an autonomous heart ventricle finder [106]. For the AIF perfusion series and PD-to-perfusion image registration, only LDOF-MOCO and raw image series were compared as the Siemens-MOCO software does not support them.

4.3.10 Sequential perfusion frame consistency

As a measure of frame-to-frame appearance consistency and structural alignment, Pearson's squared correlation coefficients (R^2) and mutual information ($MuInfo$) were computed on sequential image pairs of the perfusion T1 images across the full cohort of patient studies. Mutual information stems from information theory and compares the statistical dependence between two images [156]. Whereas the classical R^2 is useful in comparing both photometric and geometrical similarity between images, $MuInfo$ is typically considered as a robust similarity metric as it is less sensitive to illumination than geometrical structural changes.

The effect of breathing paradigm on the MOCO performance was also investigated. The robustness of the MOCO algorithms with respect to breath hold (BH) and free breathing (FB) was evaluated using a difference ratio (DR) term given by :

$$DR = \frac{\mu_{BHmoco} - \mu_{FBmoco}}{\mu_{BHraw} - \mu_{FBraw}} \quad (4.1)$$

where μ is either the R^2 or $MuInfo$ metric value. A smaller difference ratio represents a higher degree of robustness against a change in breathing paradigms.

4.3.11 PD-to-perfusion registration

The R^2 between the last PD frame and the first perfusion T1 frame were used as a measure of registration quality for the three PD-T1 combinations outlined in Table 4.1.

4.3.12 LV and myocardial perfusion dynamics

To study whether the MOCO process distorts the pixel intensity profile of the highly dynamic signal changes in the myocardial regions undergoing perfusion, stress and rest time-intensity curves of the LV and myocardium were measured on all three slices of the LDOF-MOCO and raw perfusion series in a subset of 17 healthy subjects. On the MOCO series, the myocardial region of interest (ROI) was manually drawn on the epicardium and endocardium walls by a CMR-trained expert. The anterior septal insertion point (ASI) of the RV was also positioned and the myocardium was divided into six equiangular sectors. The mean intensities of the pixels encompassed by the endocardial and sector boundaries at each frame were then computed to produce the LV and myocardium perfusion time signal intensity curves, respectively.

To extract the intensity dynamics of the corresponding myocardial regions from the raw series, the myocardial borders and ASI delimited above were automatically backwarped from the

MOCO series throughout the raw series using the flow fields computed from the LDOF engine. The corresponding myocardial pixels in both MOCO and raw series are thus included in the corresponding sectoral ROIs for comparison of time-intensity curves. This method allows a non-linear tracking of the ROI boundaries from the MOCO series onto the raw series and the measurement of the signal intensity dynamics from the native image pixels. Correlation and normalized root-mean-squared-error (NRMSE) was then used to measure the LV and sectoral perfusion dynamic similarities between the LDOF-MOCO and raw series.

4.3.13 LV centroid displacement

Finally, translational motion correction was evaluated locally in the heart region by computing the LV centroid displacement on the three slices of the subset cohort series that underwent ROI backwarping, as explained above. This analysis measures the amount of translational movement in the heart region present in the raw series that was subsequently corrected by our method. Because the Siemens-MOCO system does not provide the flow fields necessary for backwarping, we could not include their corrected series for this analysis.

4.3.14 Statistical analysis

The mean and standard deviation (mean \pm SD) were reported unless stated otherwise for the evaluation metrics used throughout the analysis. Non-parametric Mann-Whitney U-tests were carried-out to compare different test groups. A p-value < 0.05 was considered statistically significant.

4.4 Results

As summarized in Table 4.1, all stress and rest perfusion studies from 291 clinical subjects were processed with the proposed motion correction framework without exclusion. A total of 1746 myocardial perfusion series (three stress and three rest perfusion slices per patient) and 582 AIF series (one stress and one rest slice per patient) were processed using the same LDOF parameter settings. The computation time to process a 60 frame standard perfusion series including PD-to-perfusion registration averaged 27.33 ± 2.12 seconds and 16.71 ± 3.12 seconds for the AIF series on an Intel Core i7 4770 quad-core CPU.

To qualitatively evaluate the performance of the proposed system, supplementary video files are provided in the appendix to compare the pre- and post-motion corrected CMR perfusion images. The results shown in the movies indicate that our approach works effectively to

compensate cardiac and respiratory motions in both breath-hold and free-breathing series for the AIF, PD and perfusion images.

4.4.1 Sequential perfusion frame consistency

For quantitative evaluation, Figure 4.5 shows the mean consecutive correlation coefficient (R^2) and mutual information ($MuInfo$) curves of the raw, LDOF-MOCO, and Siemens-MOCO perfusion series across the entire cohort. All correlation curves show a drop around frames five-to-eight which corresponds to high signal intensity changes in the ventricles due to the contrast bolus arrival. For the full frame comparison, the (R^2) curves of the LDOF-MOCO present higher scores than the Siemens-MOCO and raw throughout the whole series and also exhibit noticeably less jitter. These fluctuations seen in the raw curves and to a lesser degree in Siemens-MOCO curves after frame 30 – perhaps due to diaphragm movement from tidal breathing or respiration gasps – is noticeably improved in the LDOF-MOCO curves. In the automatically delimited heart region encompassing the RV, LV, and myocardium, the improvement is further pronounced and shows a similar trend with an increased (R^2) and reduced jitter for the LDOF-MOCO over the entire range.

As previously mentioned, the ($MuInfo$) is less sensitive to photometric changes, thus these curves do not exhibit a drop during bolus arrival as in the (R^2) curves. Rather, $MuInfo$ monotonically increases during baseline and early perfusion until reaching a plateau near peak myocardial enhancement. This reflects the structural enhancement in the ventricles and myocardium during the arrival of the contrast media, which improves the similarity between adjacent frames. This trend is more pronounced in the heart region than in the full frame comparisons. Similar to the (R^2) curves, the LDOF-MOCO shows higher ($MuInfo$) scores than in Siemens-MOCO and raw.

For group statistics depicted in Figure 4.6, the mean correlation coefficient shows improved frame-to-frame consistency in LDOF-MOCO and Siemens-MOCO perfusion series vs. raw on the full frame series (both $p < 0.0001$). Our approach scored (R^2) = $0.996 \pm 3.735e-3$, Siemens-MOCO obtained (R^2) = $0.990 \pm 8.555e-3$, and raw followed with (R^2) = $0.978 \pm 2.024e-2$ in the full frame comparison. In the heart region LDOF-MOCO obtained (R^2) = $0.985 \pm 1.459e-2$, Siemens-MOCO scored (R^2) = $0.973 \pm 2.651e-2$, and raw trailed with (R^2) = $0.933 \pm 5.205e-2$. Of clinical interest, the heart region is well corrected by both MOCO systems, but shows a generally lower (R^2) score compared to full frame as this area undergoes large intensity fluctuations during perfusion. In all cases, the proposed LDOF-MOCO algorithm outperforms the Siemens-MOCO ($p < 0.0001$) with noticeable improvements in the heart region. The $MuInfo$ shows a similar trend for both MOCO algorithms vs. raw, but our

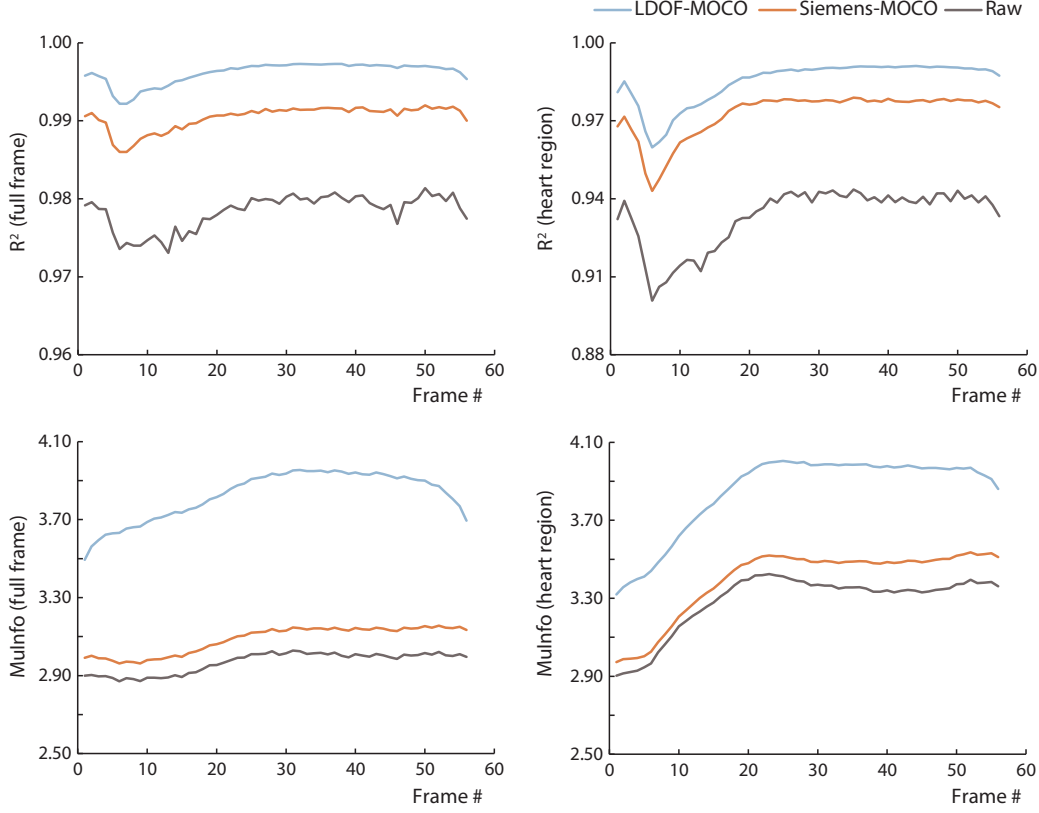


Figure 4.5 Comparison of Sequential Perfusion Frame Mean Consistency Curves. Temporal variability of the mean correlation coefficient (R^2 ; top row) and mutual information ($MuInfo$; bottom row) metrics computed across the T1-weighted perfusion series of the entire cohort for both full frame (left column) and heart region (right column).

approach is largely favored by this metric with an increase of 28.89% in full frame $MuInfo$ compared to 3.97% for Siemens-MOCO, and similarly 17.25% vs. 3.39% in the heart region.

The breathing paradigm chosen during acquisition has a modest, but statistically significant effect on the performance of the MOCO systems (Figure 4.7). In breath hold series, the proposed LDOF-MOCO approach has a $2.764\text{e-}3$ higher full frame (R^2) than in free breathing, whereas (R^2) in the Siemens-MOCO shows a larger $1.082\text{e-}2$ increase during breath holding. A more pronounced trend is observed in the heart region comparison, where the Siemens-MOCO shows greater sensitivity to breathing, as is reflected by a $2.415\text{e-}2$ increase of (R^2) in breath hold, whereas the LDOF-MOCO increases only by $8.480\text{e-}3$. Indeed, the LDOF-MOCO exhibits higher robustness to breathing in both cases, as its difference ratio of the (R^2) metric given by equation 4.1 is only 0.124 vs. 0.485 for the Siemens-MOCO in the full frame series and 0.175 vs. 0.497 in the heart region comparison. The full frame difference ratios of $MuInfo$ between LDOF-MOCO and Siemens-MOCO are similar with 1.101 and

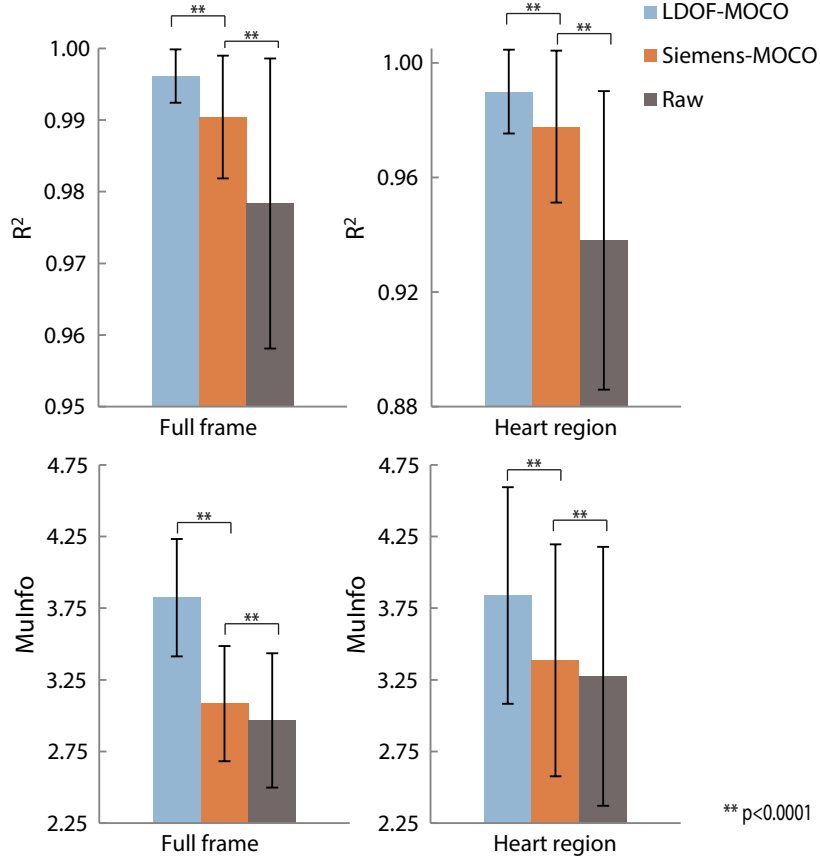


Figure 4.6 Comparison of Sequential Perfusion Frame Consistency. Mean correlation coefficient (R^2 ; top row) and mutual information ($MuInfo$; bottom row) metrics computed across the T1-weighted perfusion series for both full frame (left column) and heart region (right column) of the entire cohort.

1.132, respectively. However, for the heart region cases, the $MuInfo$ difference ratios indicate a detrimental sensitivity to breathing for the Siemens-MOCO with a score of 0.878 vs. 0.140 for our approach. Overall, LDOF-MOCO exhibits superior intra and inter-paradigm performance.

4.4.2 AIF image registration

The image motion in the AIF series was also well managed by our approach. The average full frame R^2 scores were improved to $0.987 \pm 1.180e-2$ after LDOF-MOCO vs. $0.964 \pm 3.860e-2$ for the raw, whereas the $MuInfo$ scores increased by 18.54% from $2.325 \pm 9.663e-1$ to $2.756 \pm 8.798e-1$ (both $p < 0.0001$). Likewise, (R^2) scores in the heart region reached $0.974 \pm 2.310e-2$ after LDOF-MOCO compared to $0.944 \pm 5.240e-2$ for the raw, and the $MuInfo$ increased to $3.349 \pm 8.907e-1$ from $3.051 \pm 9.730e-1$ (both $p < 0.0001$). As the Siemens-MOCO

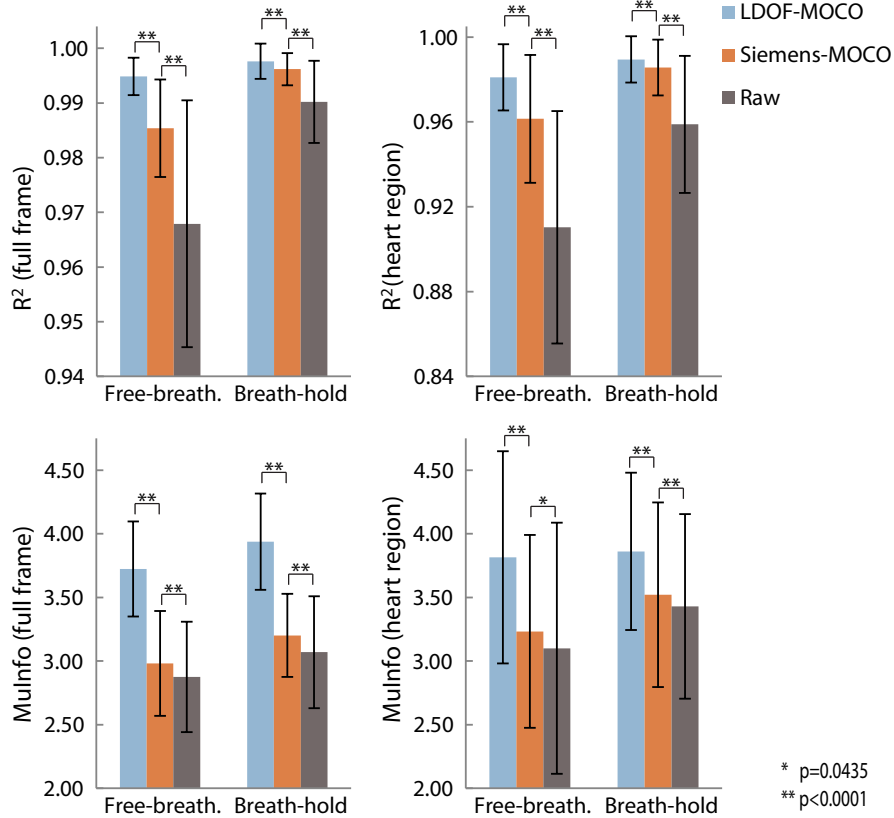


Figure 4.7 Comparison of Sequential Perfusion Frame Consistency for Breathing Paradigms. Mean correlation coefficient (R^2 ; top row) and mutual information ($MuInfo$; bottom row) metrics computed for free-breathing (left column) and breath-hold (right column) cohorts.

does not process AIF images, evaluation was not performed.

4.4.3 PD-to-perfusion registration

For the automatic PD-to-perfusion registration, the R^2 scores computed between the last PD frame to the first perfusion T1 image are significantly improved in all three PD-T1 sequence combinations (Figure 4.8). The correlation score increase is generally higher in the heart region and shows the largest gains in the FLASH-to-FISP configuration with a 9.70% increase compared to no registration ($p = 0.0005$). This improvement is followed by FLASH-to-FLASH (3.76%, $p = 0.0472$) and FISP-to-FISP (1.44%, $p = 0.0497$). Likely due to the large textural differences between PD and perfusion images, none of the $MuInfo$ scores were significantly different. Siemens-MOCO does not process PD-to-perfusion image registration so it was not evaluated.

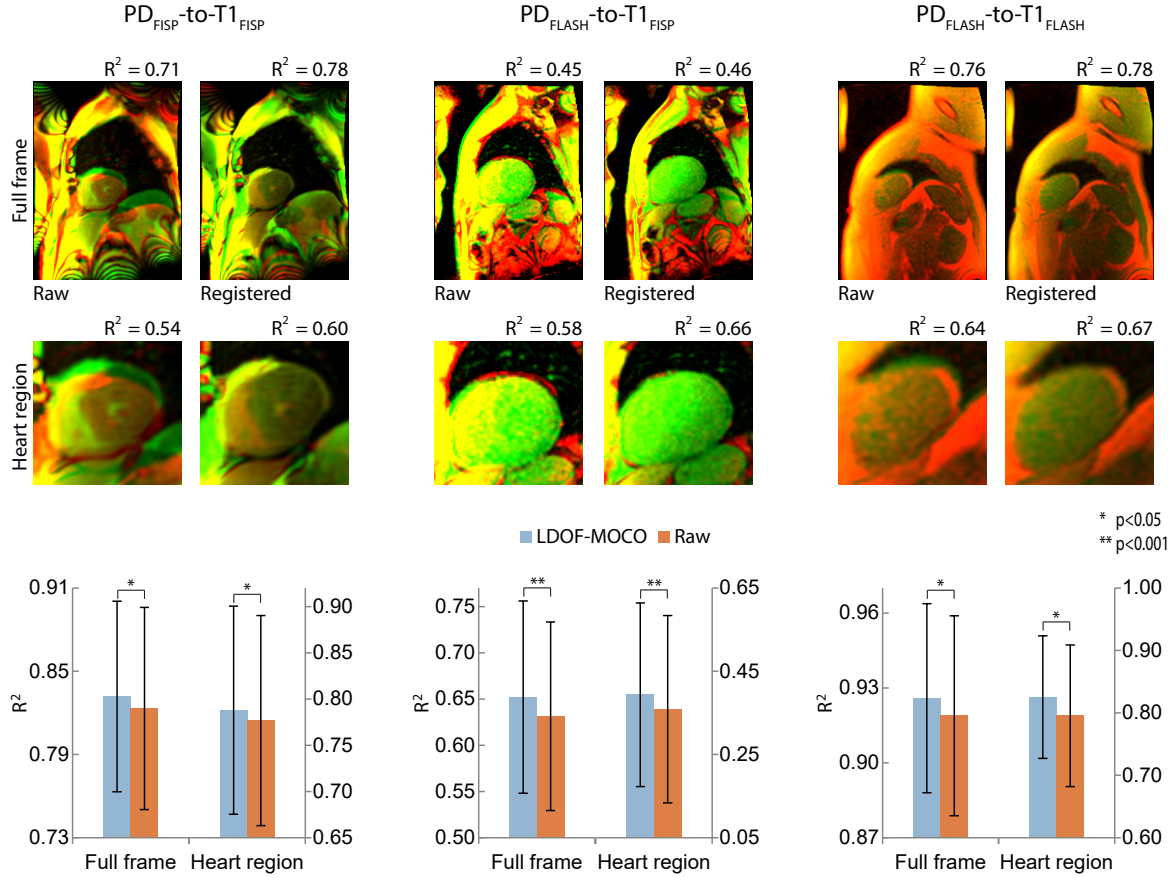


Figure 4.8 Comparison of PD-to-Perfusion Image Registration. Top two rows show examples of PD (red) to T1 (green) perfusion image registration with corresponding correlation scores for three different sequence combinations. Bottom row shows the mean correlation coefficient (R^2) computed between the last PD image and the first T1 perfusion image over the entire cohort.

4.4.4 LV and myocardial perfusion dynamics

The MOCO series produced by our approach conserves the signal intensity dynamics incurred by the contrast agent transit and subsequent myocardial tissue perfusion. Such outcomes are illustrated in Figure 4.9 for a stress perfusion series where the effects of motion on the time signal intensity curves are evident for the raw series, but well-controlled after LDOF-MOCO. Across our test cohort, as shown in Figure 4.10, the correlation between the time signal intensity curves of the LDOF-MOCO and the raw-backwarped series shows excellent agreement with (R^2) values of $0.999 \pm 5.070\text{e-}4$ in the LV cavity and $0.995 \pm 6.420\text{e-}3$ for all myocardial sectors combined. In the comparison that would be expected to result in worse correlations, the average correlation between the raw vs. raw-backwarped series was $0.997 \pm 2.811\text{e-}3$ in the LV and only $0.894 \pm 1.501\text{e-}1$ in the myocardium.

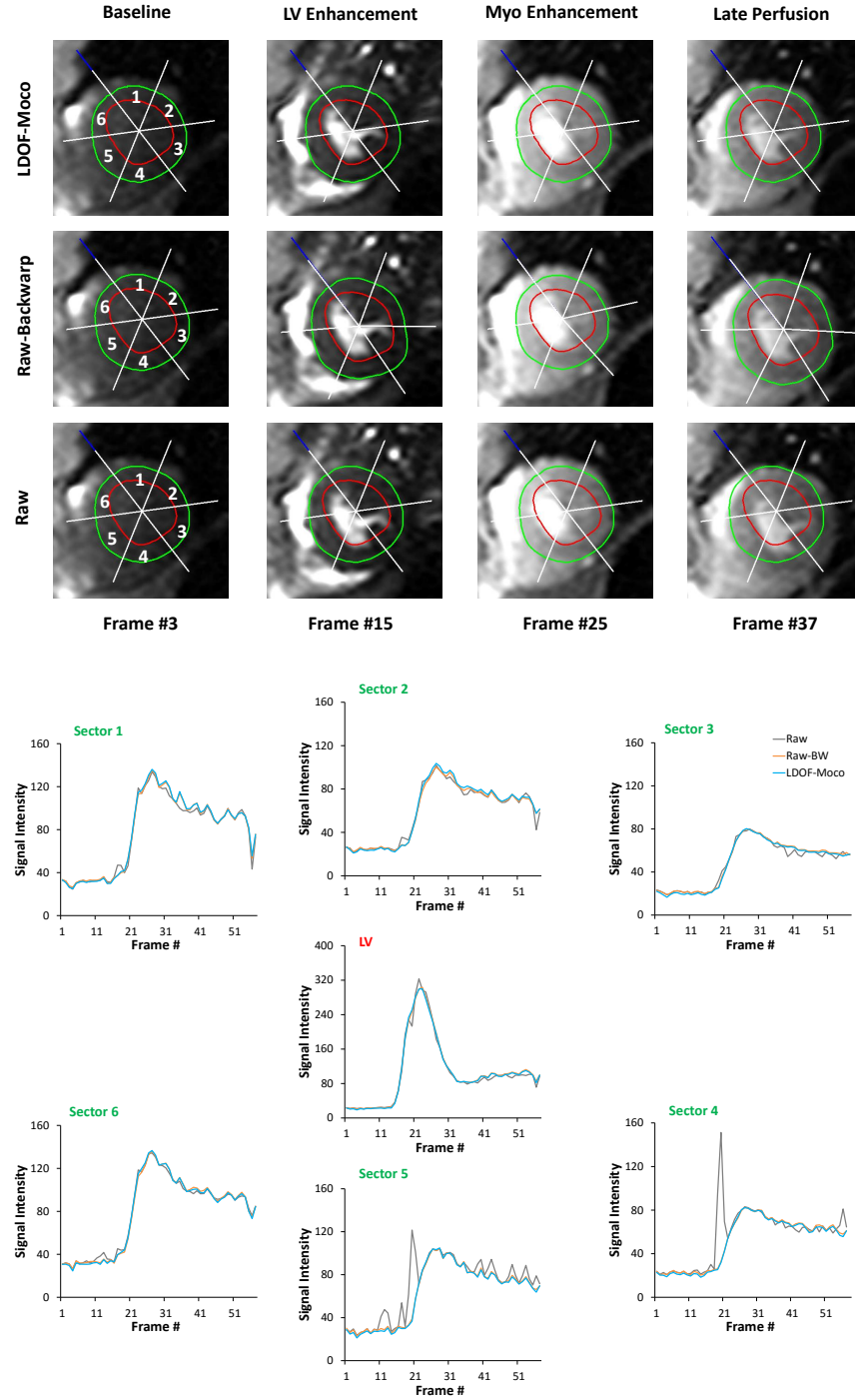


Figure 4.9 Comparison of LV and Myocardial Perfusion Dynamics. Top three image rows show the change of contrast dynamic during a stress perfusion series as well as LV and myocardium sectors defined by different regions of interest (ROI). The ROI were traced on motion corrected images (LDOF-MOCO) and then backwarped to the raw perfusion images (Raw-BW) to generate the corresponding sectoral signal intensity (SI) curves as shown. As a comparison, SI curves of the raw perfusion images without ROI backwarping (Raw) were also generated to show the impact of image motion in different myocardial sectors. In contrast to large motion-related signal intensity fluctuations in the raw SI curves (sector 4 and sector 5), LDOF-MOCO and Raw-BW curves are much smoother and are almost indistinguishable from each other.

Normalized RMSE (NRMSE) of the LDOF-MOCO and the raw-backwarped signal intensity curves is also well managed with a mean value of $7.580\text{e-}3 \pm 3.906\text{e-}3$ for the LV signal and $5.245\text{e-}2 \pm 2.139\text{e-}2$ in the myocardial sectors. Comparatively, the average NRMSE is significantly higher between raw vs. raw-backwarped series, whilst the ROIs remain statically positioned on the raw series. The mean NRMSE increases by 34.40% for the LV signal and up to 51.04% in the myocardial sectors (both $p < 0.0001$). This analysis was not performed for Siemens-MOCO since the displacement fields were not available for backwarping.

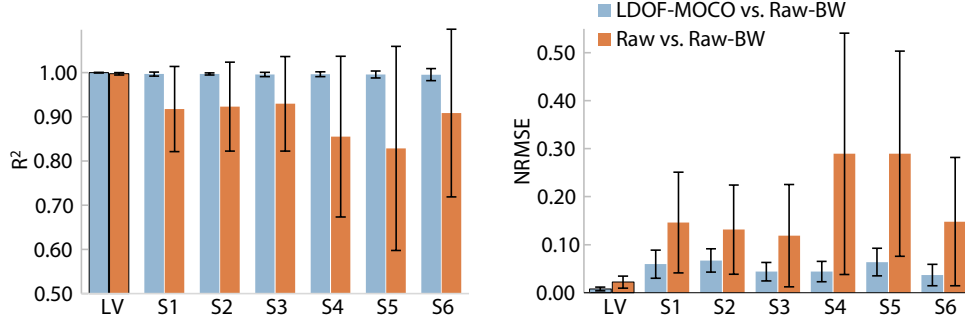


Figure 4.10 Perfusion Dynamics Comparison. Correlation (R^2) and normalized root-mean-square error (NRMSE) comparisons of time signal intensity curves in LDOF-MOCO vs. Raw-backwarped, and Raw vs. Raw-backwarped, image series.

4.4.5 LV centroid displacement

Translational movement of the LV region, which is the major detrimental factor for CMR perfusion analysis, is largely corrected by the proposed method. Figure 4.11 illustrates the LV centroid excursion on the three slices of a stress-condition series, which remains static in the LDOF-MOCO series. The raw mid-ventricular and apical slices show progressively more motion compared to the basal slice, particularly in the y direction due to chest wall movement. In the test cohort, the mean cumulative Euclidean displacement of the LV region corrected by the LDOF-MOCO is 59.11 ± 34.21 mm in the basal slices; 62.26 ± 33.89 mm in the mid-ventricular slices; and 66.03 ± 33.00 mm in the apical slices.

4.5 Discussion

The work presented in the study addresses several important requirements for a robust non-rigid motion correction scheme in CMR perfusion series. Although our approach uses an optical-flow based algorithm as the core non-linear motion estimator which is similar to the previous work by [272], this work advances the technique in many aspects. The novel contributions of the proposed system are five-fold :

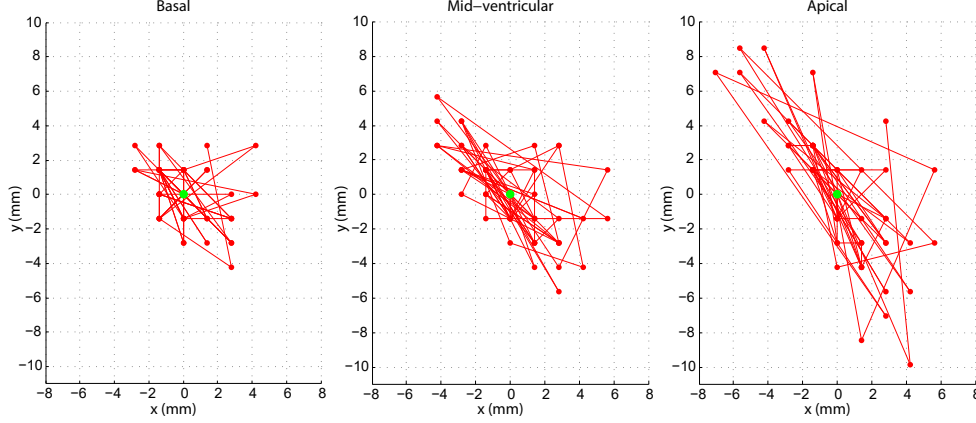


Figure 4.11 LV centroid excursions. Frame-to-frame LV centroid positions illustrating the amount of translational motion on three slices of a typical stress perfusion image series. The origin (green) is the LV centroid position measured from the LDOF motion corrected perfusion images.

- Robustness to multiple imaging sequence configurations (FISP, FLASH, AIF) and magnetic field strengths (1.5T and 3.0T);
- Multi-contrast PD-weighted to T1-weighted perfusion image registration, including various PD-T1 configurations;
- Robustness to both free breathing and breath hold paradigms;
- Explicit post-MOCO photometric specification to preserve perfusion dynamics;
- Multithreaded architecture designed to increase computational efficiency.

Various image registration schemes have been developed to compensate for myocardial motion in CMR perfusion imaging [88]. As a significant portion of motion in the series is composed of in-plane translational and rotational movement, a large body of the earlier work was focused on rigid registration [91, 267, 2, 20, 24, 49, 64, 1, 175]. Although these techniques improve qualitative and some aspects of quantitative analysis, they fail in precisely aligning the epicardium and endocardium tissue undergoing elastic deformations, which is needed for high-resolution pixel-wise myocardial perfusion analysis. Nonrigid registration techniques have thus garnered recent research interest.

Notable contributions include techniques that build a motion-free synthetic reference series to which the perfusion frames are registered. [266] devised a multi-pass scheme that uses independent component analysis and quasi-periodic breathing patterns to identify motion components throughout the series. Motion-free synthetic images were then created by removing the major independent components related to movement. The perfusion frames were finally non-linearly registered to the corresponding synthetic images with a B-spline transformation model [206] optimizing a normalized gradient field similarity metric. Likewise,

[144] constructed a pseudo ground-truth synthetic series in the heart region that was free of translational motion, image noise, and conserved pairwise image intensity profiles by using a spatiotemporal smoothness constraint to ostensibly help the registration stage. Following semi-automatic segmentation of the LV and RV using a multistage level set approach, elastic myocardium deformations were then corrected by aligning the real and synthetic image sequences together.

Conversely, some techniques use a unique reference frame to which all other images are registered. [119] employed this paradigm by first performing rigid registration followed by nonrigid motion correction. They started by manually delineating the LV walls to linearly align the segments to a single reference image. This was followed by two stages of nonrigid registration where a B-spline transformation model incorporating the 1st and 2nd order normalized mutual information similarity metric was used to register non-linear motion between the target and reference myocardial walls. A refinement step was then performed by matching the iso-contours of the walls formed using the Laplace-potential approach [120]. [240] also non-linearly registered the myocardial walls using a semi-automatic approach requiring manual LV seed point placement. Following automatic reference frame detection, the cavity (including the papillary muscles) was segmented using a region-based level set approach integrating local noise patterns to aide in delimiting the endocardium. The epicardium was then detected using an edge-based level-set formulation [220]. The combination of a correlation-based rigid motion estimation followed by boundary refinement of the level-set model was finally used to register the frames to the reference target.

[241] used the middle frame of the image series as a reference image with a method inspired by the Morphons algorithm [126]. As opposed to using anatomical landmarks learned from a manually labeled training set [227], they used local phase as intensity-insensitive features to represent image edges and lines. These features were coupled with the so-called Demons algorithm [246] in a dyadic coarse-to-fine scale-space approach to perform non-rigid registration. Finally, as mentioned above, [272] used a variational optical-flow based approach to consecutively register neighboring images to an automatically determined key frame. However, unlike our approach, this technique and others that perform serial or sequential registration [87, 96] tend to accumulate alignment errors and may result in large motion estimation artifacts for frames temporally distant from the reference.

The issues complicating motion correction compiled from this body of work originate from the patient specific displacement and deformation of different anatomical structures during dynamic contrast enhancement. It is thus difficult to devise population-based statistical models or rely on anatomical assumptions. The dramatic contrast variations observed in the CMR

perfusion series during LV and RV contrast bolus passages, and subsequent tissue perfusion must also be taken into account to achieve robust performance by any motion correction systems. Furthermore, we note the scarcity of methods tested with varying sequence types, under both traditional breath hold and free breathing paradigms, and correcting motion within/between auxiliary/perfusion images used to improve perfusion quantification. Consideration for ergonomic computational times, which is required for clinical adoption, is also seldom discussed.

In our quantitative evaluation over a large and diverse cohort, we showed the performance of the proposed approach consistently surpasses the currently available commercial system for motion correction in CMR perfusion series. Both R^2 and *MuInfo* testing metrics showed superior full frame correction, but notable improvements were measured in the heart region, which may indicate finer myocardial wall motion estimation aided by our inline automatic flow field distortion correction step, which permits aggressive variational optical flow settings.

Temporal analysis of the MOCO performance of our approach showed smoother frame-to-frame appearance consistency and noticeably less jitter caused by late breathing gasps. Increased robustness to respiration was measured in our results compared to the Siemens-MOCO. This highlights the strength of the discrete feature matching component of the LDOF engine as large chest wall and diaphragm displacements caused by breath hold failure or free breathing were effectively corrected.

The motion in the low resolution AIF series was also significantly corrected by the LDOF-MOCO. Despite the lower SNR of the imaged anatomical structures, similar improvement in R^2 scores to the higher resolution perfusion T1 series was shown in full frame and particularly in the heart region, which may facilitate the automation of the LV signal intensity measurements used for perfusion quantification and signal calibration [106].

Our LDOF approach was successfully generalized for PD-to-T1 image registration. The HOG feature matching component was shown to be robust to the varying appearances of the PD-T1 combinations, which concurs with previous uses of HOG matching in multimodal registration applications [248, 160, 111]. However, despite statistically significant quantitative improvements in R^2 in all the PD-T1 configurations for both full-frame and heart region comparisons, the metric used to assess the quality of the registration is hindered by the large photometric and textural differences of these two types of images. To illustrate this, Figure 4.8 shows real-world examples of PD-to-perfusion registration with their corresponding correlation scores. As evident in these series, the R^2 scores show modest gains in all comparisons, which in our opinion may not adequately reflect the drastic improvement in myocardial alignment between PD and T1 series as shown in the accompanied qualitative comparison.

In terms of clinical applicability, our approach preserves tissue perfusion dynamics as measured in the LV cavity and the myocardium. Using the ROI backwarping approach, precise pixel-to-pixel mapping was carried out between the MOCO and raw image series, and excellent agreement of perfusion dynamics was found in the LV and myocardial region between the two series. With regards to clinical workflow, a mean processing time of 27.33 sec per standard perfusion series was measured on a standard quad-core processor desktop computer. This processing time will likely improve as our multithreaded pipeline will scale favorably with increasingly sophisticated processor architectures and parallel computing implementations.

Lastly, the amount of translational motion corrected by our approach was illustrated by tracking the LV cavity centroid across the perfusion T1 series. The large displacement of the LV cavity subsequently corrected highlights the benefits of automatic motion correction and its necessity for pixel-wise perfusion quantification applications.

4.6 Conclusion

This paper describes an automatic and universal nonrigid motion correction system for first-pass CMR perfusion series. It was shown to be robust to varying acquisition parameters including sequence type, breathing paradigm, SNR, and image resolution. It was also demonstrated to successfully register proton density weighted images to T1-weighted perfusion images in varying sequence types. Importantly, our approach was shown to preserve the signal intensity dynamics crucial for qualitative and quantitative diagnosis. The proposed system outperformed a commercial motion correction system using a large cohort of clinical patients. Finally, its multi-threaded post-hoc warping configurations, coupled with automatic flow field distortion correction are other notable contributions. Designed around strict operational requirements, the system’s quantitative and qualitative performance, combined with its reasonable per-series processing time promotes its integration in routine CMR perfusion analysis protocols.

CHAPTER 5 Article 2 : SPATIOTEMPORAL ANALYSIS OF ANGIOGRAPHIC SERIES FOR PATHOLOGICAL CORONARY ARTERY SEGMENTATION

Mitchel Benovoy^{1,2}, Nagib S. Dahdah², Farida Cheriet^{1,2}

1 : Institute of Biomedical Engineering, Polytechnique Montreal, Montreal, Canada.

2 : Sainte-Justine University Hospital Research Center, Montreal, Canada.

5.1 Abstract

An automatic and efficient coronary artery segmentation framework of pathologically dilated vessels is presented. The system employs a combination of dual-tree complex wavelet transform and homomorphic filtering stages to improve the photometric quality of x-ray angiographic series, which are motion-compensated and processed with a recursive, steerable anisotropic Gaussian curvilinear line extraction module. The spatiotemporal analysis of the propagation of the radiopaque contrast agent within the angiographic sequences is then used to construct motion masks that isolate the segmented arterial tree from non-vessel background structures. Finally, a posteriori detection of pathological vessel regions such as aneurysms or ectasia corrects and enhances the segmentation result. The system's performance was evaluated on 62 angiographic recordings from 31 patients and demonstrated excellent agreement between its automatically measured diameters and commercial manual and semi-automatic analysis platforms. In a clinical context, this approach affords enhanced visual inspection, objective measurements, and the detection of anomalous vessel physiology.

5.2 Introduction

The standard diagnostic protocol for coronary artery disease calls for selective cardiac catheterization using x-ray fluoroscopy [33]. This procedure involves the injection of a radiopaque contrast agent producing a dynamic, two-dimensional angiographic sequence of a targeted and potentially pathological vascular network. As the prevalence of cardiac disease remains high [82], this routine practice yields large amounts of data traditionally analyzed manually and is thus susceptible to operator and procedural variability [97, 66, 182]. Current practices incur considerable stress on hospital resources in terms of diagnosis efficiency, staff time,

and data management. For diagnostic purposes, the complex structure of the coronary artery tree is difficult to interpret from the two-dimensional angiographic projections. This problem is highlighted while stratifying thrombogenesis risk in abnormal vessel regions such as aneurysms and ectasia, where blood flow is affected by a given pathology's impact on vessel geometry [217, 59]. Automated, computerized visualization enhancement of the vessels by segmentation and objective coronary diagnostic metric extraction are therefore welcomed clinical tools.

Vessel segmentation approaches can be divided (although non-exhaustively) between centerline extraction, appearance-based, and model-based. The reader is guided to comprehensive reviews of vessel segmentation approaches [122, 60], but notable contributions specifically applied to coronary artery extraction from x-ray angiographic sequences are presented here to highlight their clinical limitations.

In their simplest form, centerlines are drawn manually [167, 9]. This operation is naturally prone to observer variability, which motivated the development of semi-automatic methods to reduce human interaction by requiring only the input of a segment's start and/or end points (typically at bifurcations). [271] proposed a sequential tracking-based method set to improve well-known semi-automatic techniques [230, 10] using a self-adaptive *look-ahead* scheme. Although the results demonstrated good management of areas of high curvature and inflection, the centerlines at regions of vessel shrinking showed divergences from ground truth and some segments were disjointed at bifurcation points. Based on line network extraction using polyline processes, [137, 138] derived an automatic artery extraction technique by modeling the coronaries' centerlines as Markov object processes. The method performed well when homogeneous intra-vessel illumination, large contrast ratios between the background and the arteries, and small curvature of the main vessels were encountered. [146] achieved automatic centerline extraction by first preprocessing the angiographic images with coherence enhanced diffusion [260] and Hessian vesselness filtering [72]. Disconnected segments were automatically rejoined by a line-linking operation leveraging their spatial position and orientation. Bone segments and other radiodense artefacts were present in the segmentation result. Predictably, the thinning operation created cyclic centerline segments at larger vessel calibers (typically near the proximal position) and the authors disclosed that their technique would be challenged by areas of low-contrast due to certain pathologies.

[239] first coordinated manually-selected mask and contrast image sets formed using digital subtraction angiography (DSA) into pairs with their *energy of the histogram of the difference* [31] and registered them using B-spline free-form deformation [206]. Under the assumption that vessel and background images are independent signals mixed with the contrast frames,

independent component analysis (ICA) was used to separate the vessels from the background. The method produced good overlap scores with manually segmented references compared to DSA-only and multi-scale line-enhanced filtering results. The technique deteriorated vessel boundaries on some distal segments (prone to large movement), which underlines the difficulty in aligning noisy and motion-rich radiographic images as this issue is likely the result of pre-DSA registration error.

A milestone for appearance-based approaches was the use of the modes of variation of the Hessian matrix to enhance vessel-like structures [151, 211, 72]. A *vesselness* term is formed with a thresholding scheme applied to the ratio of the Hessian’s smallest and largest eigenvalues to highlight, respectively, image points of strong curvature and line direction while attenuating flat areas. Vessels of different diameters are enhanced, but tubular background structures and noise will also be extracted and thus require additional processing, as in [71]. Vesselness was used in [139] to determine seed points from a vessel resemblance function that drives a recursive intra-vessel region growing routine. The primary coronary arteries were well segmented, but the secondary arteries were largely eliminated. This is illustrative of Hessian-based methods’ tendency to produce discontinuities by suppressing branching or overlapping vessel areas as these resemble flat regions. [259] thus proposed a post hoc region-merging test based on histogram information and clustering to establish homogeneity between disconnected segments. Distal branch segmentation and continuity was to some extent improved, but the vessel diameters were affected as some focal areas were shrunk, producing stenosis-looking regions. [213] used the image Hessian to compute directional vector fields to form so-called *discrete streamlines* encoding local vessel connectivity and morphological information to relax vesselness constraints, which prevented the disconnection of branches at bifurcation points. This idea was improved upon in [118], where multiscale vesselness and a more robust direction estimator using the Hessian matrix eigenvectors to drive region growing. Similar approaches include an evolutionary scheme used by [52] to tackle the issue of adequate threshold selection by multi-objective optimization of Hessian vesselness measures and local feature fitting active contours to add robustness to intra-vessel illumination heterogeneity [235].

Model-based techniques explicitly leverage templates or patterns of vessel morphology and/or tree-like structures to aide segmentation [277]. The match-filtering approach by [129] was introduced as a robust technique capable of handling complex vessel geometry and noisy backgrounds. They used a circular sampling operator to match image regions to predefined vessel templates where strong spatial coherence at small, local-scales of the vessels was assumed. Tests on patient images showed dilation and shrinking of some segments, deterioration of the vessel wall, sectioned branches, and disjoint, “floating” artifacts. The performance of model-based methods on pathological segments may be hindered as the morphological complexity

of aneurysms [232] is diverse and unique to every patient.

Steerable filters afford selective control of the orientation and width of the curvilinear structures to be extracted [73] by convolving the input image with a set of rotated and scaled filter kernels known as a *basis bank*. The *curve-image* is then computed as a combination of all the filter responses. Variants of anisotropic steerable filtering are featured prominently in the literature across different imaging modalities [132, 131, 189, 54, 67], but similar to the other methods presented above, steerable filtering frameworks will fail to segment pathological areas as they diverge from a tube-like appearance. However, they present interesting characteristics in terms of computational efficiency [81, 254, 280], and their selective orientation and line-width sensitivity make them particularly interesting to mitigate noise and avoid segmenting non-vessel structures.

The majority of segmentation approaches use a single static frame, thus discarding the rich spatiotemporal information found in the angiographic sequences. Spatiotemporal clustering [165, 123, 109] typically aims to cluster data based on their spatial distance and temporal similarity [104]. Formulations to include spatiotemporal data for clustering have been proposed in trajectory detection using expected maximization and probabilistic regression [75] and extensions to fuzzy c-means, [50, 104, 62, 105]. Applied to vasculature, modeling the coronary tree at each cardiac phase has been used to enhance the segmentation result by inferring its shape information from the spatiotemporal models [78]. Temporal tracking has been used to improve stenosis identification by first tracking the arterial centerline, and then computing the vessel diameters at each time point [48]. Persistent minima identified over many frames were then labeled as stenotic regions. The *Vessel Walker* segmentation method [168] was extended to include a temporal prior that tracks the lumen over sequential frames using landmark and shape matching [169]. Methods that specifically track contrast agent filling are seldom encountered as vessels must be aligned to a stable geometrical configuration prior to isolating its propagation.

The issues complicating high quality vessel extraction compiled from this body of work originate from the dynamic nature of the thoracic region and the variability in vessel appearance between and within patients. Prominent factors contributing to the non-uniform characterization of vessels are intra-image illumination variations, radiographic noise, overlapping bones and organs, heterogeneous vessel contrast, and abnormal vascular regions related to pathology. Most of the reviewed methods present results on small datasets containing largely healthy vessels. Even with manual intervention – which is in itself prohibitively time-consuming and prone to operator variability – most of the approaches encountered issues in their results. Importantly, it is apparent that pathological vessel segments in the form of stenosis,

aneurysms or ectasia hinders the performance of most of these techniques. Thus, it is not surprising that the predominant form of clinical coronary artery analysis is still conducted on hand-selected raw angiographic frames. Of the existing commercial segmentation systems used for diagnostic purposes, most are based on either semi-automatic centerline extraction.

The automatic segmentation framework presented here aims to address the issues highlighted above by integrating robust noise and illumination mitigation ; fast steerable-filtering curvilinear structure extraction ; and novel pathological region detection. Notably, our segmentation framework applies motion compensation and leverages the spatiotemporal propagation of the radiopaque contrast agent through the vascular network during fluoroscopy in order to automatically isolate the targeted arterial tree (considered hereafter as the foreground) from the peripheral non-vessel structures (background) present in the angiographic frames.

5.3 Materials and methods

The main design requirement driving the development of the proposed system is compliance with current selective coronary catheterization protocols to maximize its potential adoption within long-established clinical practices. In addition to requiring high-quality results, this implies its compatibility with the large amount of existing patient angiographic recordings, fast execution time on commodity hardware, and minimal operator intervention.

5.3.1 Angiographic data acquisition

During typical recording sessions, an electrocardiogram (ECG) is used to monitor the patient’s heart activity. A radiodense catheter is guided through large arteries and positioned inside the aorta where the tip is aligned with the coronary arteries’ ostium. The contrast agent is then injected through the catheter while sequential radiographic exposures are acquired at 15 to 30 frames per second. The resulting image series containing several hundred frames primarily shows the tracer’s circulation through the arterial tree, but also records large dynamic components such as bone (ribs and vertebrae) movement following the patient’s respiration, catheter shake from its proximity to the beating heart, and the deformation of the transiently radiodense arteries as the myocardium undergoes contraction and expansion. Besides these physiology-related motion components, it is not uncommon for the clinician to move the patient during fluoroscopy, causing translational shifts of all radiopaque elements in the recorded frames.

5.3.2 Motion compensation

These dynamically-rich scenes necessitate motion mitigation on selective components judged obtrusive to the segmentation objective. Ultimately, a sequence primarily depicting the tracer’s propagation through a stable morphological phase of the arteries is desired. The ECG signal is thus used to extract angiographic frames corresponding to the heart’s end-diastolic (ED) phase, where the ventricles are filled with blood and the corresponding myocardial regions are maximally expanded, which in turn causes the coronary arteries to be at their utmost distended geometric configuration (Figure 5.1a).

However, gating alone may present errors, especially in patients with high heart rates or those with certain pacing pathologies. Respiration and other patient movement is also likely to occur during the recording session, which causes large nonrigid structural deformations between the ED frames. An optical-flow formulation specifically amenable to large displacements [28] was thus used to estimate structural displacement between sequential frames. This formulation couples histograms of oriented gradients (HOG) [55] landmark matching in a coarse-to-fine warping scheme with variational optical flow. The former estimates large displacements, while the latter handles small deformations at a sub-pixel accuracy. As the flow fields between sequential frames are produced, the images are motion-corrected with bicubic interpolation warping. The resulting ED series is thus effectively compensated of respiration and myocardial motion, as shown in Figure 5.1b.

5.3.3 Image preprocessing

Preprocessing the motion-corrected end-diastolic frames prior to curve extraction helps preserve vessel morphology and lowers artifact creation further along the processing chain. In x-ray imaging system, the primary noise component visible in the captured frames is the quantum noise originating from the photons hitting the image intensifier, which can be approximated by a Poisson distribution [155, 198]. This noise is attenuated using a 2D dual-tree complex wavelet transform (DT-CWT) scheme [121], where the image is decomposed by filtering and downsampling into six levels each containing six bandpass subimages of complex coefficients. These coefficients are then soft-thresholded (also-known-as wavelet shrinking) with an automatically determined value using the Donoho method [63]. To restore the filtered image, the inverse wavelet transform is computed. The qualitative performance of this technique is apparent in Figure 5.2b, in which the image’s graininess is eliminated but the high-frequency structural details such as the vessel boundaries and small-caliber distal arteries are conserved. Quantitatively, in this representative example the SNR between the filtered and raw image is 27.04.

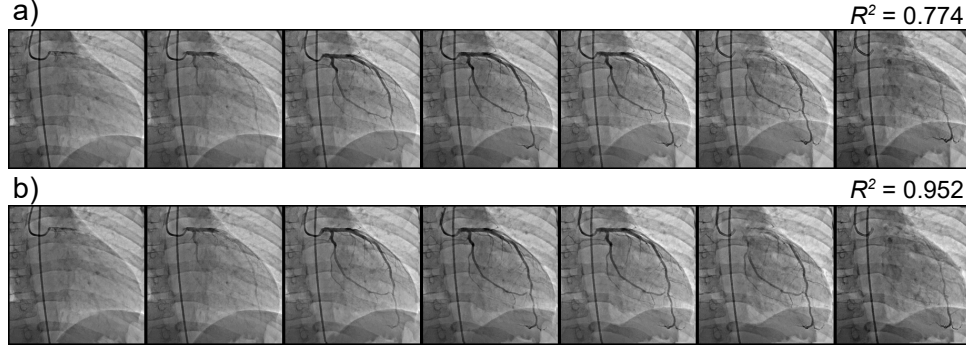


Figure 5.1 Angiogram motion correction : a) Raw end-diastolic sequence, b) Motion-corrected end-diastolic sequence. The mean sequential correlation coefficients are reported in this example as a measure of frame-to-frame alignment.

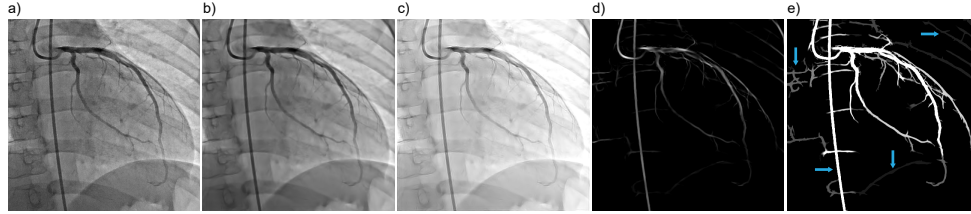


Figure 5.2 Angiographic frame processing : a) Raw, b) DT-CWT filtered, c) Homomorphic filtered, d) Anisotropic curve extracted & rectified, e) Connectivity pruned & tortuosity normalized. Arrows indicate remaining non-vessel structures.

Following noise suppression, the sequence is processed with homomorphic filtering [265] to establish photometric correspondence within and across frames. This normalizes lighting variability by high-pass filtering in the log-intensity domain, which decreases the illumination component of the images while amplifying the high-frequency reflectance component generally associated to the structural information. In angiographic images, this translates to brightening the large areas shaded by soft tissue and bone without significantly affecting the relatively smaller vessels' contrast (Figure 5.2c). The various parameters for this type of filtering were empirically determined.

5.3.4 Curvilinear structure extraction

The arteries and other curvilinear image elements are extracted from the homomorphic-filtered images using a steerable scale-space analysis method based on efficient 2D anisotropic Gaussian filtering [81]. The filter aligned to a varying vessel orientation θ and anisotropic variances σ_u, σ_v (set to a 3 : 2 aspect ratio, empirically determined) is expressed as a convolution in the u and v directions ($u \perp v$) by :

$$g(u, v, \sigma_u, \sigma_v, \theta) = \frac{1}{\sqrt{2\pi}\sigma_u} \exp\left\{-\frac{u^2}{2\sigma_u^2}\right\} * \frac{1}{\sqrt{2\pi}\sigma_v} \exp\left\{-\frac{v^2}{2\sigma_v^2}\right\} \quad (5.1)$$

with

$$u = x \cos \theta + y \sin \theta \quad (5.2)$$

$$v = -x \sin \theta + y \cos \theta \quad (5.3)$$

and $\theta \in [0, 180]$ in 10° increments, variance parameter σ_v set to anatomically plausible vessel widths empirically derived : $\sigma_v \in [^2/3, ^8/3]$ in $^1/3$ increments for 512x512 pixels image dimensions. These values should be scaled proportionally to the output resolution of the imaging equipment used.

It is computationally advantageous to decompose the 2D filters in two separate one-dimensional components [61], where the first is locked on the x -axis and the second is steered along an axis l oriented at ϕ :

$$g(x, y, \sigma_u, \sigma_v, \theta) = \frac{1}{\sqrt{2\pi}\sigma_x} \exp\left\{-\frac{x^2}{2\sigma_x^2}\right\} * \frac{1}{\sqrt{2\pi}\sigma_\phi} \exp\left\{-\frac{l^2}{2\sigma_\phi^2}\right\} \quad (5.4)$$

where

$$\phi = \arctan\left\{\frac{\sigma_v^2 \cos^2 \theta + \sigma_u^2 \sin^2 \theta}{(\sigma_u^2 - \sigma_v^2) \cos \theta \sin \theta}\right\} \quad (5.5)$$

$$l = x \cos \phi + y \sin \phi \quad (5.6)$$

$$\sigma_x = \frac{\sigma_u \sigma_v}{\sqrt{\sigma_v^2 \cos^2 \theta + \sigma_u^2 \sin^2 \theta}} \quad (5.7)$$

$$\sigma_\phi = \frac{\sqrt{\sigma_v^2 \cos^2 \theta + \sigma_u^2 \sin^2 \theta}}{\sin \phi} \quad (5.8)$$

To further lower the processing requirements of the curvilinear structure extraction, (5.4) can be implemented in a recursive form [254, 280]. Doing so lowers the processing load of the filtering to only seven multiplications in both directions, and computational complexity becomes independent of the variances. For each vessel width value and across the whole range of orientations, the maximum filter response is retained at each pixel location and the resulting image is rectified to suppress filtering artifacts neighboring the vessels. Finally,

the maximum response across the whole range of vessel widths is computed to create the curve-extracted frames. As shown in Figure 5.2d, these images contain several non-vessel components such as bony structures and the catheter. Some of these components may not be connected to the vessels and are thus considered “floating” artifacts. Under the assumption that the largest continuous component in these images is the arterial tree, *connectivity pruning* is performed to eliminate both “floating” and loosely connected components, as outlined in Algorithm 1.

Algorithm 1 Morphological connectivity pruning

- 1: Erode the images using a $r = \min \frac{\sigma_v}{2}$ pixel radius disk to disconnects structures linked by weak line artifacts without affecting the smallest anatomically-plausible vessels.
 - 2: Rank each connected component based on their area.
 - 3: Delete all but the largest structure. A single continuous curve structure ostensibly corresponding to the arterial tree remains.
 - 4: Dilate the images with a r pixel radius disk to restore the original vessel dimensions eroded above.
-

Also apparent in Figure 5.2d is the varying intra-vessel intensity not necessarily associated with a vessel-wall pathology. To avoid diagnostic confusion, the arteries’ tortuosity is normalized by applying the H-maxima transform [225] and saturating the minimum and maximum 1% of the images’ intensity histograms to boost contrast. The resulting frames show a near-homogeneous intra-vessel segment appearance (Figure 5.2e). The different shades of gray apparent in some of the branches represent intra-vessel contrast loosely related to the concentration of the radiodense tracer. This shading is conserved as a coarse, but helpful visual indication of tracer’s current propagation state.

5.3.5 Spatiotemporal masking

Although most of the flat, homogeneous background components have been eliminated from the curve-extracted images, as shown in Figure 5.2e, numerous non-vessel elements are present as these are superimposed and linked to parts of the arterial tree and therefore not eliminated by the connectivity pruning. A region of interest (ROI) surrounding the arterial tree is thus necessary to separate it from the background.

We introduce here the concept of motion masking to isolate the vessels by tracking the propagation of the radiopaque tracer across the sequence of curve-extracted, ED frames (Figure 5.3a-top). First, the same optical flow routine used for motion compensation is used to compute the spatial velocity profile of the pixels between each sequential frame. The salient

motion regions correlated with the tracer's flow in the arteries are thus produced as motion maps across the sequence (Figure 5.3a-bottom).

These motion maps primarily depict strong velocities in the arterial tree region, but background structures will also create motion components, albeit at a smaller magnitude. We mitigate these velocity estimates with kernel principal component analysis (kPCA) [258, 214, 171] by reconstructing a new motion map retaining between 70%–80% of the total variance ($d = 2$ principal components are typically sufficient). The n motion map images (each containing m pixels) are first vectorized and stacked in a $n \times m$ dimensional space \mathbf{x} . Given the Gaussian kernel function :

$$k(\mathbf{x}, \mathbf{y}) = \exp \frac{(-\|\mathbf{x} - \mathbf{y}\|^2)}{2\sigma^2} \quad (5.9)$$

the $n \times n$ kernel matrix $\mathbf{K}_{i,j} = k(\mathbf{x}_i, \mathbf{x}_j)$ is used to compute the Gramian matrix :

$$\tilde{\mathbf{K}} = \mathbf{K} - \eta\mathbf{K} - \mathbf{K}\eta + \eta\mathbf{K}\eta \quad (5.10)$$

where η is the $n \times n$ matrix with all elements equal to $1/n$. Solving for vectors \mathbf{a}_i by eigen-decomposition in :

$$\tilde{\mathbf{K}}\mathbf{a}_i = n\lambda_i\mathbf{a}_i \quad (5.11)$$

the kernel principal component projections $y_i(\mathbf{x})$ are then computed with :

$$y_i(\mathbf{x}) = \sum_{j=1}^n a_{ij}k(\mathbf{x}, \mathbf{x}_j), j = 1 \dots d \quad (5.12)$$

Finally, the reconstruction of the motion maps using the kernel principal component projections $y_i(\mathbf{x})$ is approximated in an iterative manner [171] with :

$$\mathbf{z}_{k+1} = \frac{\sum_{i=1}^n \gamma_i \exp(-\|\mathbf{z}_k - \mathbf{x}_i\|^2/2\sigma^2)\mathbf{x}_i}{\sum_{i=1}^n \gamma_i \exp(-\|\mathbf{z}_k - \mathbf{x}_i\|^2/2\sigma^2)} \quad (5.13)$$

where \mathbf{z}_1 is initialized to the mean of the data vectors in \mathbf{x} , and

$$\gamma_i = \sum_{t=1}^n y_t a_{it} \quad (5.14)$$

The reconstruction iterations in (5.13) are halted with stopping criterion : $\|\mathbf{z}_k - \mathbf{z}_{k+1}\|/\|\mathbf{z}_k\| <$

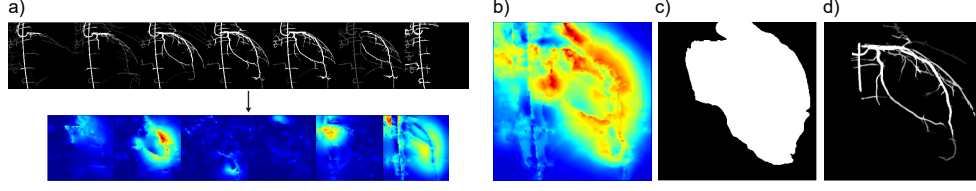


Figure 5.3 Optical flow analysis and motion mask creation : a) Curve-extracted sequence (top) and motion map sequence (bottom, color-graded to velocity magnitude), b) kPCA-computed flow map, c) Binary motion mask, d) Masked peak vessel frame.

α , where $\alpha = 0.1\%$. The resulting dimension-reduced map (Figure 5.3b) has kept most of the salient flow regions and reduced noisy background-related motion. The motion mask is then created by clustering this principal flow map using a graph cuts approach [157], where the algorithm is constrained to compute only two clusters to create a binary motion mask ostensibly corresponding to the foreground and background regions (Figure 5.3c). Finally, the mask is applied to the curve-extracted ED series, producing an isolated arterial tree region (Figure 5.3d). For diagnostic purposes, the frame depicting the whole arterial tree (labeled as the *peak* vessel frame) is identified by computing the foreground area in each image across the series and retaining the one with the maximum value.

Algorithm 2 Appearance-based aneurysm detection.

- 1: Apply the motion mask computed above to the corresponding *peak* homomorphic image as a pathology ROI delimitation, which lessens the risk of falsely detecting non-vessel elements outside the arterial tree.
 - 2: Binarize the image elements contained in the ROI using Otsu's automatic thresholding [190].
 - 3: Erode the resulting blob-like structures with a $r = \min \frac{\sigma_v}{2}$ pixel radius disk structuring element to retain the border profile computed with the curvilinear structure extraction module.
 - 4: Hole-fill the binary blobs to correct for negative areas caused by severe intra-aneurysm tortuosity generated by swirling or slow-filling of the contrast agent. This effect is markedly pronounced in larger aneurysms.
 - 5: Filter the remaining structures based on their percent overlap with the segmented arterial tree to ensure their association with the pathological vessels. The blobs with overlap scores $> 90\%$ are discarded as these correspond to areas nearly completely enclosed in the previously-segmented vasculature, whereas lower scores will indicate a region overlapping the targeted, hollowed structures (Figure 5.4c).
 - 6: Add the remaining positive areas to the image, effectively in-painting the pathological regions in the peak vessel frame.
-

5.3.6 Aneurysm region correction

The steps described above produce adequately “clean” segmentation results on a large range of patients with normal coronary arteries. However, the curve extraction algorithm will fail in segmenting abnormal vessel regions such as aneurysms or ectasia caused by certain pathologies (Figure 5.4a). This problem is inherent to most line segmentation methods as these anomalous structures diverge from typical curvilinear characteristics and will produce hollowed regions (Figure 5.4b). To mitigate this issue, the pathological areas are detected from the pre curve-extracted frames by leveraging their strong, relative contrast with respect to the illumination-normalized background. The procedure is outlined in Algorithm 2. As shown in Figure 5.4c, it is possible that some portions of the detected aneurysms overlap non-hollow vessels. This is inconsequential to the final segmentation result as the in-painting will re-color already filled-in areas, as illustrated in Figure 5.4d.

5.3.7 Automatic diameter computation

The binary nature of the segmented image affords numerous automatic and efficient implementations of metric computations useful for diagnostic purposes [148]. Not the least of which is vessel diameter extraction, which is routinely used to assess conditions associated to ischemic diseases. To demonstrate the potential of the system and to test its quantitative performance, a simple automatic diameter measuring routine using the segmented images is proposed in Algorithm 3.

5.4 Experimental

The performance of the system was evaluated on a dataset of 62 angiographic series acquired on a Toshiba Infinix-CFI Bi-Plane C-Arm. The study cohort was composed of 31 pediatric patients (median age = 9.5 years, range = 2–17 years) undergoing Kawasaki disease screening or heart transplant follow up. A 32nd patient’s two angiographic series were used to tune the various algorithmic parameters. These were not modified during testing on the remaining patients. This project was approved by the Ethics and Scientific Research Committee of the Ste-Justine University Hospital Research Center (Montreal, Canada) and parental consent was obtained for the use of the coronary artery imaging involved in this study. The qualitative performance assessment was conducted by a cardiologist and a medical imaging specialist to evaluate segmented vessel appearance fidelity, branch suppression, and the presence of non-vessel artifacts.

Vessel dimension preservation was evaluated by comparing 862 diameters measured manually,

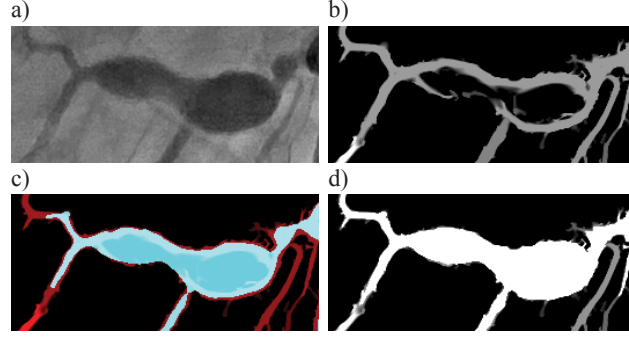


Figure 5.4 Aneurysm detection : a) Raw frame aneurysm, b) Curve-extracted frame, c) Detected aneurysm area (cyan), d) Aneurysm-corrected segmentation.

semi-automatically, and computed automatically at the same positions by the algorithm described in Section 5.3.7. The manual measurements of the coronary segments were conducted by an independent radiology technician. The semi-automatic measures were performed by the manufacturer's (Toshiba of Canada Ltd., Markham, Canada) clinical product specialist. Calibration and measurements were performed using the manufacturer's standards. The manual measures used the commercial software's embedded electronic calipers, and the semi-automatic measures were obtained with the manufacturer's software by placing a start and stop point on the target vessel segment. The selection of segments to be measured were dispersed along the whole coronary artery tree, including proximal and distal branches of various sizes. This evaluation methodology was performed to reflect real-world usage, where vessel diameters are the predominant quantitative measure used for coronary artery pathology diagnosis. We believe the use of this metric as our gold-standard versus hand-drawn segmented arterial trees affords a more robust, efficient, and realistic test as the technicians' expertise and experience are fully leveraged.

5.5 Results

A paired-samples t-test revealed no significant differences between the automatically computed diameters on the segmented images and the manual measures on the raw angiographic frames (Figure 5.5a, mean difference = 0.14 ± 0.52 pixels or 0.02 ± 0.09 mm, $p = 0.241$). Likewise, there was no significant difference between the automatic and the semi-automatic measures (mean difference = 0.10 ± 0.37 pixels or 0.01 ± 0.06 mm, $p = 0.317$). Excellent measurement correlation was found for both smaller and larger segments (Figure 5.5b, $r^2 = 0.964$ between automatic and manual, $r^2 = 0.972$ between automatic and semi-automatic, $p < 0.01$). Computationally, the average non-optimized processing time running in Matlab (Natick,

Algorithm 3 Skeletonization-based automatic diameter computation.

- 1: Skeletonize the vessel images using morphological thinning.
 - 2: At each curve vertex \mathbf{x}_0 (except for branching and end points), identify the two skeletal vertices adjacent to the immediate 8-connected neighbors of \mathbf{x}_0 : $\mathbf{x}_{-2}, \mathbf{x}_2$.
 - 3: Compute the null space of $\mathbf{x}_{-2} - \mathbf{x}_2$ by singular value decomposition to approximate the normal vector at \mathbf{x}_0 .
 - 4: Iteratively grow the vector in both forward and backward directions until it reaches the vessel boundaries (corresponding to a 1-to-0 intensity change).
 - 5: Add both forward and backward vector lengths to compute the vessel diameter at \mathbf{x}_0 .
-

USA) on an Intel (Santa Clara, USA) Core i5 platform was 0.38 ± 0.11 seconds per frame to produce the segmented peak vessel image from the raw angiographic sequences (mean length = 188.14 ± 49.2 frames). Automatically computing diameters at each vessel point across the whole arterial tree within a frame is done in 0.86 ± 0.4 seconds.

From a qualitative perspective, the framework produced connected arterial trees preserving most distal arborisations and the original morphology of the vessels. Curvature, boundary profile, and branching points conserve appearance fidelity with the raw frame vessels. In addition, 18/18 (100%) of the aneurysms and vessel ectasia regions present across the dataset were successfully segmented. Some of the smallest vessels were suppressed and few remnants of non-vessel structures (vertebrae, ribs, and organ outlines) that were both in-closed in the high-motion area and connected to the arterial tree by superposition were not eliminated. The largest non-vessel element present in some of the segmented images is the catheter due to its intrinsic similarity to the arteries' appearance. However, this is of little clinical concern as it is easily identifiable by observation and should have minimal impact in quantitative pathology evaluation as the x-ray imaging configuration selected by the operator during the recording

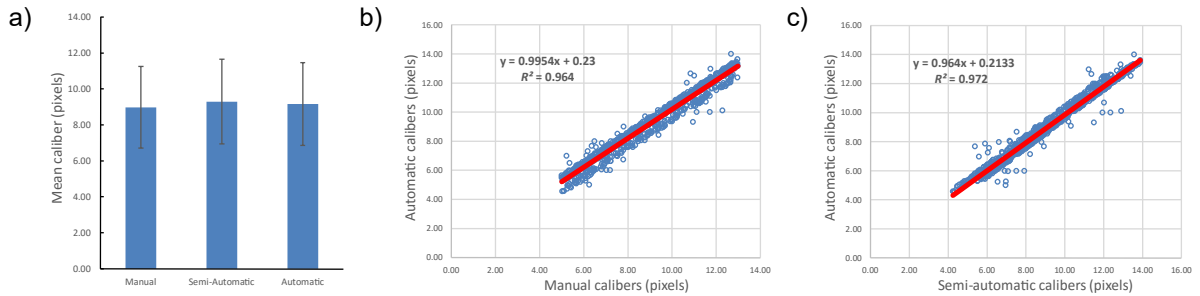


Figure 5.5 Segmentation performance : a) Mean diameter difference (\pm s.d.) between automatic and manually measured vessel diameters, b) Linear regression between automatic and manual diameter measures, c) Enlarged distal regions of raw (top row) and segmented (bottom row) vessels.

session would preclude any overlap between the vessel segments targeted for investigation and the catheter. The automatic segmentation results from various patients and viewing angles are illustrated in Figure 5.6.

5.6 Discussion

The system presented here was designed by normalizing the arteries’ geometric configuration and stabilizing inter-frame mis-alignment with automatic, image-based motion compensation. The main sources of noise hindering curvilinear structure segmentation performance from x-ray angiographic series were mitigated with the combination of DT-CWT and homomorphic filtering. These techniques were proven successful in eliminating image graininess characterized by Poisson-noise and normalizing the illumination profiles of the large background elements, respectively. The resulting curve images produced by the anisotropic curvilinear extraction module contain few artifacts, but can still present some remaining structures associated to bones, catheter, or organ boundaries overlapping the vessels and not eliminated by connectivity pruning. The hallmark of our approach was thus introduced to help delineate the arterial tree by exploiting the spatiotemporal information contained within the cardiac-gated and motion-compensated ED angiographic series as opposed to limiting the processing domain to a single frame. The tracking of the radiodense tracer’s propagation inside the vessels using a formulation of optical flow, the computation of the principal motion components with kernel PCA, and the subsequent construction of a motion mask were shown to effectively delimit the arterial tree from the background. Interestingly, this motion masking approach can benefit from high patient heart rates as more ED frames would be included in the spatiotemporal analysis and in turn increase the precision of the principal motion map. This result is particularly interesting for pediatric patients, who typically present with high basal heart rates [237, 125].

The development of the aneurysm and ectasia detection module is an important innovation capable of correcting for the intrinsic deterioration of these lesioned areas by the curve extraction module. Precluding explicit consideration of this problem – as is common to most vessel segmentation techniques – the system’s adoption in a clinical context would be obviated. This robustness to pathological areas affords better visual tracking over patient follow up sessions and their objective parameterization not possible with previous methods. Our approach’s clinical appeal is further validated by its automatic nature, fast operating time, good qualitative performance in terms of vessel appearance fidelity, and excellent metric correlation with manually measured diameters on a large patient dataset. To the best of our knowledge, this system’s qualitative and quantitative performance on real-world data is

currently unmatched by current coronary artery segmentation methods.

The system’s segmentation does present some weaknesses. Some of the smallest vessels were not extracted by the curve extraction routine, which is likely caused by the combination of their small calibers and their low contrast ratios with the surrounding background. However, the loss of these fine vessels is not considered of clinical significance. Some non-vessel elements with curvilinear characteristics overlapping or at close proximity to the arterial tree were included in the high motion areas and thus present in the final segmentation result.

5.7 Conclusions

This paper described an automatic coronary artery segmentation framework with high vessel morphology fidelity and robustness to pathology not previously possible with existing methods. The notable contributions of this approach are the spatiotemporal analysis to construct arterial tree motion masks and pathological region detection. Designed around strict operational requirements, the system’s quantitative and qualitative performance, coupled with its sub-second-per-frame processing time promotes its further refinement and testing under various clinical conditions.

5.8 Acknowledgment

This work was funded in part by a MEDITIS research scholarship from the Natural Sciences and Engineering Research Council of Canada (NSERC). Finally, we are grateful to Julie Lebrun, Radiology Technician at Ste-Justine University Hospital Center, and Kathleen Lowe, product specialist at Toshiba Medical Corporation for their dedicated time and expertise conducting the manual and semi-automatic measurements of the coronary arteries as well as other technical

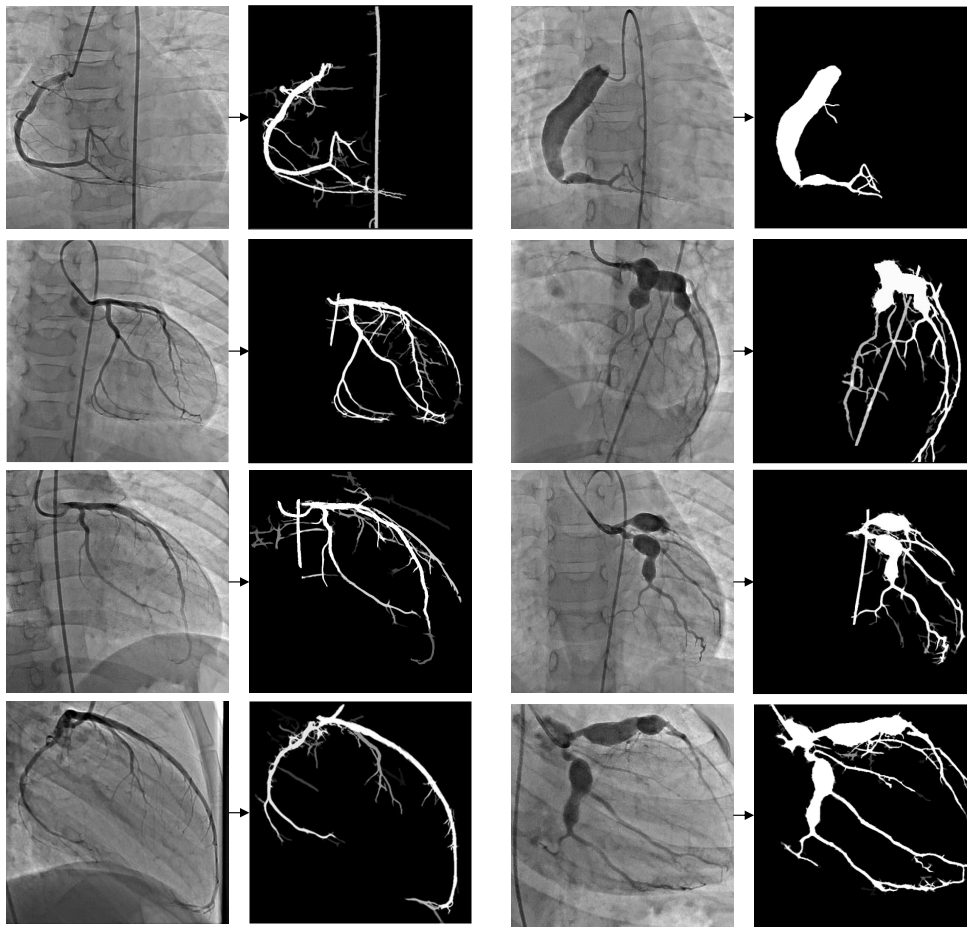


Figure 5.6 Automatic segmentation results. Raw angiographic frames with segmented result pairs. First and second columns : healthy arteries. Third and fourth columns : pathological arteries (Kawasaki disease patients).

CHAPTER 6 MEASURING CORONARY ARTERY DISTENSIBILITY VIA ANGIOGRAPHIC SERIES

6.1 Introduction

As introduced in Section 2.2.1, the alteration of vessel distensibility is a known sequelae of various vascular pathologies. In pediatric patients, KD causes thinning and destruction of the tunica media, the loss of endothelial cells, and the degradation of the vascular smooth muscles and elastic fibers into hyalinized connective tissue [256, 185]. These changes contribute to the alteration of vascular stiffness as demonstrated by intravascular ultrasound [234, 274].

In adult populations, atherosclerosis and its co-morbidities are also associated with vascular wall dysfunction [181]. This change in dynamics may contribute to the pathogenesis of myocardial ischemia [76, 84, 199]. Although routine reperfusion procedures such as angioplasty, stenting, or bypass surgery are shown to improve the outcome of these patients, the therapies themselves can alter the dynamic function of the vessel walls. Of more recent interest is the follow-up of adult patients implanted with bioresorbable stents, where it is hypothesized that natural vasomotion activity such as dilation and constriction may be restored after resorption of the implant, compared to traditional metal devices [187, 219].

The traditional diagnostic tool for both these patient populations is x-ray angiography. This modality is typically used to assess vessel dimensions on a single, static frame even though the sequences contain a wealth of dynamic information. We note the scarcity of clinical tools utilizing this information and as a result, some patients may have normal angiographic evaluations despite deteriorated vessel walls [223, 103]. The medical interest in this context is the magnitude of arterial dilation and subsequent relaxation during a cardiac cycle.

Assessing CA distensibility is typically conducted with IVUS. However, this invasive procedure is not routinely performed and may not be recommended for certain patients. On x-ray angiographic series, distensibility has been investigated in research contexts by manually measuring arterial calibers at only two time points : end-diastolic and end-systolic to encapsulate the overall variation of the diameters [117]. Conversely, the full use of the angiographic sequences – leveraging their complete dynamic spatiotemporal information – can provide the clinician with both morphological and functional vessel characteristics while limiting the number of interventions on the patients. Further, using every frame in a full cardiac cycle permits the fine scale analysis of kinetic measures such as vessel expansion and recoil velocities.

The fully automatic x-ray angiographic CA segmentation system presented in Chapter 5 was thus integrated in a framework to measure arterial distensibility. This tool's full use of angiographic series affords vessel displacement and morphology change tracking of selected arterial segments over the course of a cardiac cycle. As an exploratory study, KD patients with and without a history of aneurysmal lesions were compared with healthy patients [17]. In a follow up study, an expanded cohort of KD patients were assessed to investigate the correlation between vessel wall sequelae measured invasively with OCT and the distensibility computed from the angiographic series [18]. These two preliminary studies are presented in the following sections.

6.2 Distensibility assessment via segmentation and spatiotemporal tracking

The CA distensibility processing pipeline is depicted in Figure 6.1. Briefly summarized, the operator is prompted to draw a rectangular ROI on the vascular region targeted for analysis. The CA segmentation framework is then initiated and will segment the arterial tree, as presented in Section 5.3. The pixels corresponding to the walls of the segmented vessel within the ROI are then tracked from frame-to-frame over a full cardiac cycle using HOG point tracking.

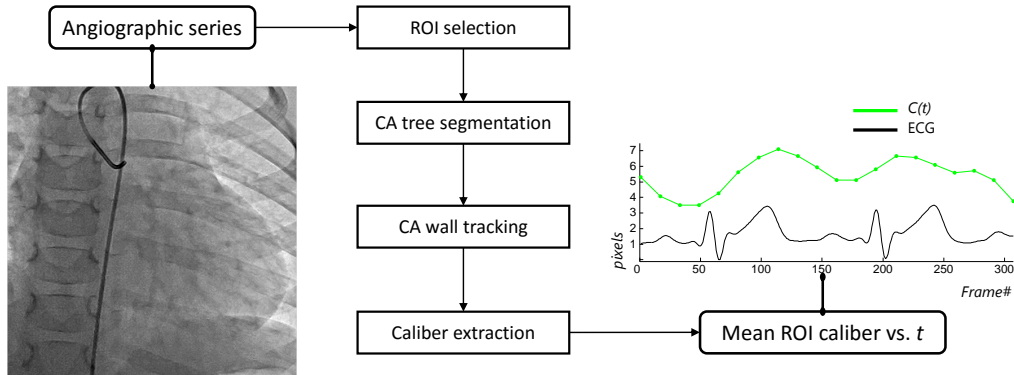


Figure 6.1 Distensibility assessment pipeline. Segmented CA wall pixels are tracked over the angiographic series, producing the caliber vs. time curve $C(t)$ shown at right.

The caliber vs. time curve $C(t)$ produced by the distensibility assessment framework on a KD patient shown in Figure 6.2a corroborates the influence of vascular pressure and mechanical function of the heart (Figure 6.2b). During the systolic phase, myocardial resistance and aortic pressure is high, causing coronary filling and their expansion. During diastole, myocardial resistance is relaxed and blood perfuses the muscular tissue, which results in coronary

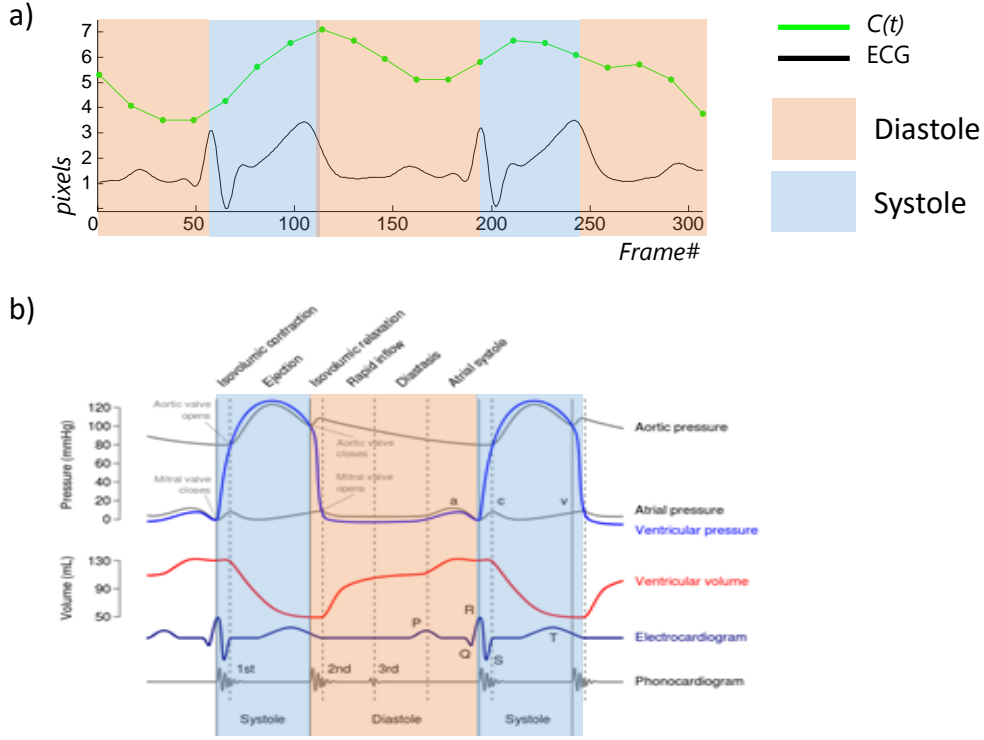


Figure 6.2 Caliber variations and pressure dynamics : a) the measured caliber vs. time curve produced by the proposed distensibility assessment framework on a proximal segment of a KD patient ; b) the prototypical pressure dynamics of the heart and surrounding vasculature during systolic and diastolic phases.

emptying and the decrease in their lumen area. The distensibility metrics computed from the $C(t)$ curve include :

The mean constriction velocity :

$$MCV = \text{mean}\left(\frac{d(C(t))}{dt} < 0\right) \quad (6.1)$$

The mean recuperation velocity :

$$MRV = \text{mean}\left(\frac{d(C(t))}{dt} > 0\right) \quad (6.2)$$

Caliber standard deviation :

$$CSD = SD(C(t)) \quad (6.3)$$

CSD mean pressure modulus :

$$CSD_MPM = \frac{MeanBP - LVEndDiastolicPressure}{CSD} \quad (6.4)$$

CSD pulse pressure modulus :

$$CSD_PPM = \frac{PulsePressure - LVEndDiastolicPressure}{CSD} \quad (6.5)$$

6.2.1 Pilot clinical studies

Two preliminary studies were conducted in order to assess the discrimination capabilities of the distensibility metrics computed from the angiographic series. In the first trial, a group of KD patients with and without a history of aneurysmal lesions were compared to a group of healthy subjects. We hypothesized detrimental distensibility measures for the KD patients compared to the healthy controls and possible stratification between the KD groups. In the second trial, a larger cohort of KD patients who underwent both standard selective angiography and OCT investigations were studied. The OCT imaging was used to identify specific arterial wall lesions and it was hypothesized that the presence of multiple types of lesions would contribute to a proportional increase in arterial stiffness, as measured by the proposed angiogram-based system.

Methods

Trial I Proximal and distal left CA angiograms were automatically segmented and vessel walls were tracked over a cardiac cycle from a cohort of 23 pediatric patients (51 total angiograms). The cohort included five healthy controls (CTL) without history of KD, hypertension, immune disease, or heart transplant. The 18 KD patients were classified with respect to positive angiographic findings of aneurysms (KDAN+, 13 patients) or negative presence of dilations (KDAN-, five patients). At each frame, CA centerlines were extracted from operator-selected ROIs and the mean segment caliber was computed from diameters sampled at every two pixels along their length. The distensibility metrics presented above were then computed. Statistical significance testing were conducted with the Mann-Whitney non-parametric U-Test.

Trial II A KD cohort of 27 patients (54 total angiographic series) with and without history of coronary aneurysms were studied. Each patient was attributed an OCT score formed by accumulating the binary findings of intimal hyperplasia, media destruction, fibrosis, and

calcification. The score thus varied from zero to four. These observations were performed independently by a physician. CA centerlines were automatically extracted from operator-selected ROIs and vessel calibers were computed at each two pixels along their length on each frame during a full cardiac cycle. The distensibility metrics from the CA calibers following KD were compared blindly to the OCT-based scoring. Pearson's correlation and Mann-Whitney U-Test were used as statistical measures.

Results

Trial I The distensibility results are shown in Figure 6.3. Data are represented as mean \pm SD in normalized pixels (npx). *CSD* was significantly reduced ($p < 0.01$) in KDAN+ ($0.25 \pm 0.05 \text{ npx}$) and KDAN- (0.27 ± 0.04) npx vs. CTL (0.38 ± 0.07) npx. The mean constriction velocity was significantly reduced ($p < 0.05$) in KDAN+ vs. CTL, with *MCV* 3.50 ± 0.67 vs. 4.59 ± 1.94 npx/sec. The mean recuperation velocity did not show significant differences. Pressure-modulated stiffness characteristics were atypical as *CSD_PPM* showed a proportional stratification, increasing from 63.87 ± 23.71 mmHg for CTL to 94.99 ± 17.68 mmHg for KDAN- to 110.03 ± 59.07 mmHg for KDAN+. In this case, both KD groups showed statistically significant results compared to CTL ($p < 0.01$). *CSD_MPM* showed a similar trend, but only CTL vs. KDAN+ (209.30 ± 80.36 vs. 275.75 ± 77.90 mmHg) was significantly different ($p < 0.05$).

Trial II Stiffness metrics correlated negatively with increased OCT scores ($r = -0.64$ for *CSD*, $r = -0.58$ for *MEV*, and $r = -0.71$ for *MCV*; $p < 0.01$ for each). Patients with OCT scores 2-4 exhibited significantly increased wall stiffness (Figure 6.4), including higher pressure-dependent elastic moduli. *CSD* results showed a linear trend with respect to OCT scores, whereas the velocity measures demonstrated a plateau effect for scores > 2 .

Pressure-modulated metrics produced less significant stratifications, but nonetheless showed a trend of increase stiffness proportional to the accumulation of lesion findings. Patients with all four types of lesions showed strikingly deteriorated distensibility compared to patients with scores ≤ 1 .

6.2.2 Discussion

In the first pilot study, the proposed distensibility assessment framework was shown to be sufficiently sensitive to differentiate between arterial stiffness of known vascular pathologies in a pediatric cohort of KD and healthy patients. The expected result of increased stiffness was found in the KD cohort, and stratification was further measured for those with and

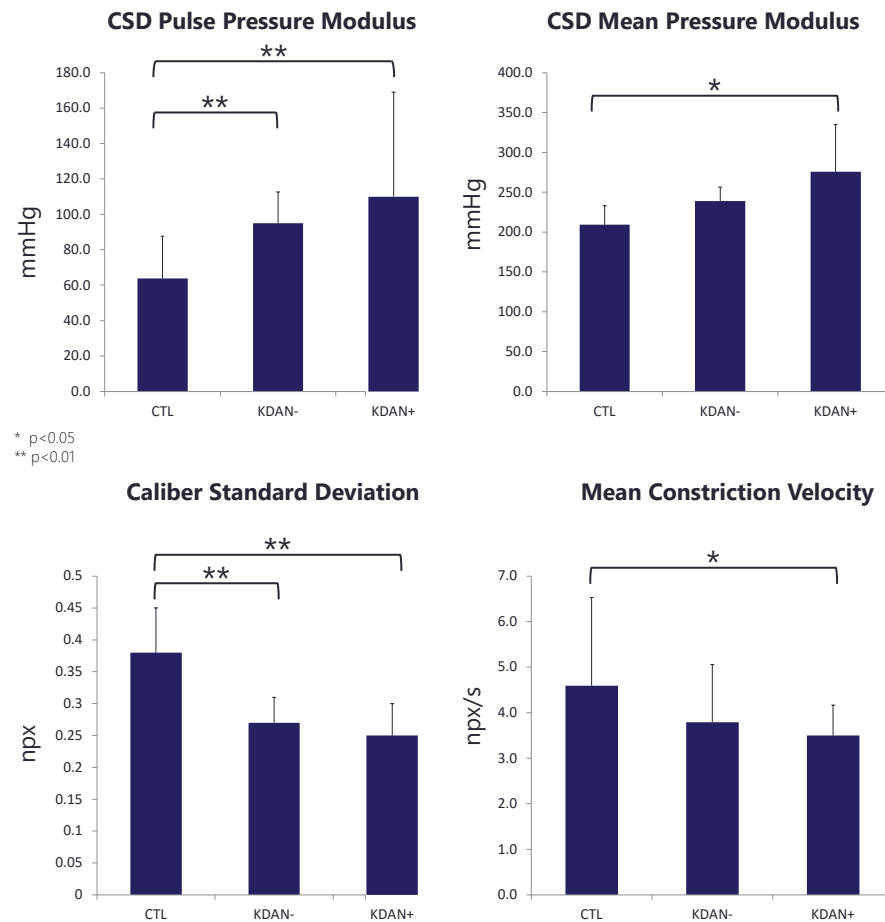


Figure 6.3 Distensibility metrics of healthy (CTL) and KD patients with (KDAN+) and without (KDAN-) history of aneurysmal lesions.

without aneurysmal history. These results concur with previous studies using invasive probes [234, 274]. The findings of deteriorated vascular walls in the KDAN- group is particularly important as these typically present with patent angiographic findings, which may instill a sense of false-confidence in patient, parents, and treating physician. In this situation, the distensibility metrics may thus eventually provide valuable information to guide long-term therapeutic plans, follow-up frequency, and general lifestyle recommendations to the patient.

The extended follow-up study was designed to relate direct OCT observations of vascular wall sequelae with the computed distensibility metrics. As such, the stiffness results point to a accumulating stiffness effect with the number of observed lesions, notably when the patient presents with two or more types of OCT findings. The observed plateauing of the velocity results for scores > 2 may be related to the mechanical limits of vessel dynamics. As a whole, these results further solidify the applicability of the proposed angiographic-based coronary

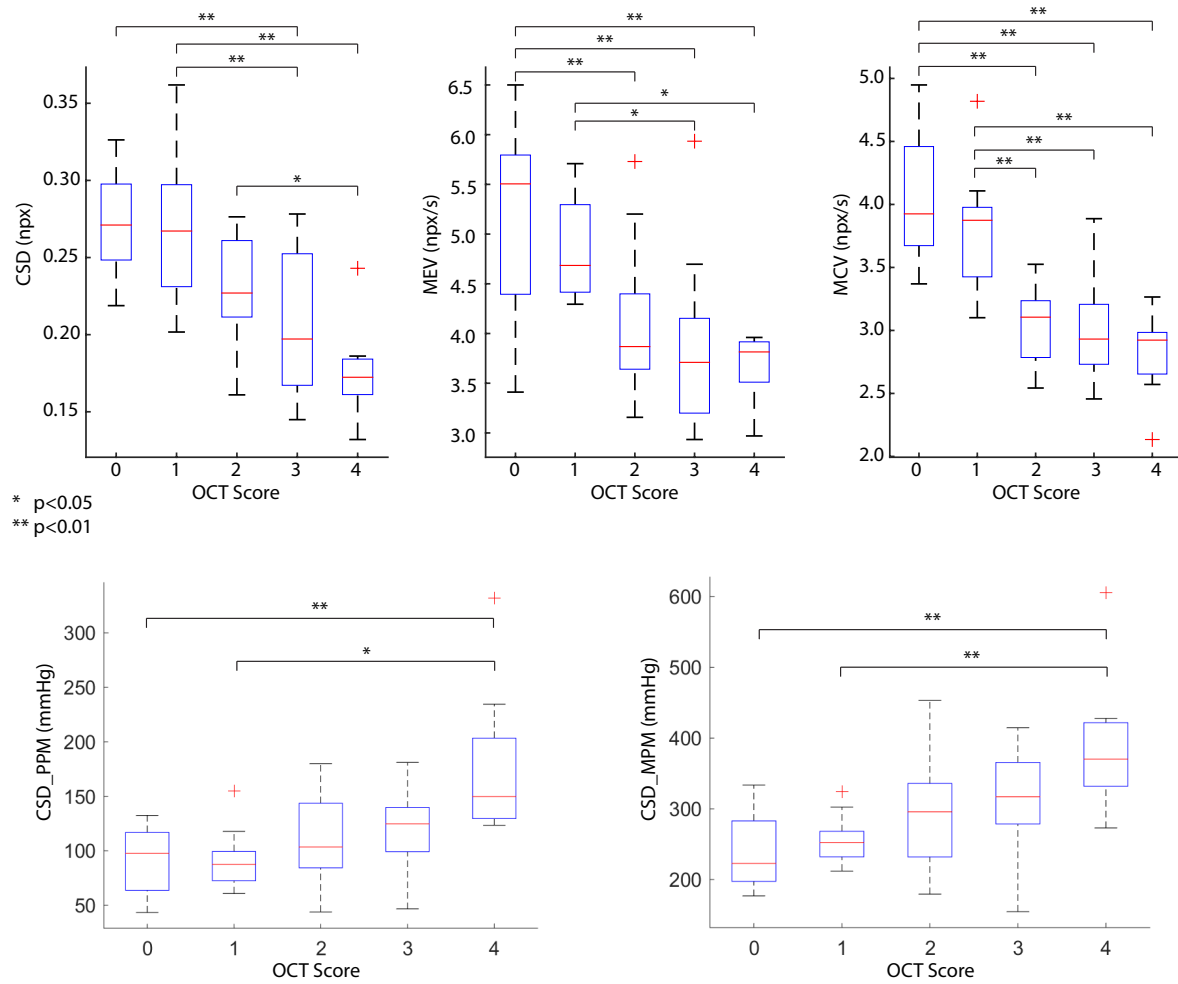


Figure 6.4 Distensibility metrics of KD patients according to their OCT score indicating the cumulative presence of observed arterial wall lesions.

distensibility assessment tool in expanded clinical investigations.

CHAPTER 7 GENERAL DISCUSSION

The general objectives of this thesis were to improve the diagnostic quality, potential, and ergonomics of cardiac images acquired with both well-established and state-of-the-art clinical imaging modalities. The issues tackled were primarily related to the spatiotemporal nature of the data and the manual, subjectivity of the measurements routinely performed with CMR perfusion and x-ray angiographic imaging by automating motion compensation and registration of auxiliary series types in the former and CA segmentation in the latter. Importantly, the motion compensation developed for CMR perfusion imaging was used to aide the segmentation process using x-ray angiography. Finally, the proposed segmentation approach’s qualitative and quantitative performance, coupled with spatiotemporal tracking of the arterial walls, enabled the development of an efficient CA distensibility assessment tool to provide potentially insightful clinical markers to the physician. These realizations are discussed in the following sections.

7.0.1 Motion compensation and registration of CMR perfusion series

An universal nonrigid motion compensation framework for CMR perfusion imaging was first proposed. At its core is the LDOF formulation, which we hypothesized would be a valid construct to estimate the wide-ranging types of motion in the various CMR perfusion sequences used in many clinical sites. Preceding motion estimate, however, required preprocessing of the CMR images. The general approach was to *simplify* the appearance of anatomical structures by reducing the dynamic range of the images. This effectively reduced textural information variability unrelated to structural motion during bolus perfusion. As such, the LDOF engine is left with salient information where its HOG-based landmark detection scheme effectively identified structural components undergoing large deformations, while the variational component handled fine-scale displacements.

The robustness to large-scale nonrigid estimation was critical in both breath-hold and free-breathing paradigms. Perhaps non-intuitively, this issue is even more important in the former. For many patients in breath-hold studies, the series may be relatively motion-free at the start of the acquisition, but towards late perfusion, the physiological and mental stress of apnea becomes too much to bear and striking breathing gasps often occur. In these situations, the magnitude of the displacements are far larger than in free-breathing cases. Furthermore, when apnea fails, the recording may have to be restarted, further increasing the burden on both the patient and clinical resources. Free-breathing studies are thus easier for both patient

and clinician, but motion compensation is naturally a necessity. Other than breathing-related movement, non-voluntary motion (e.g. : ECG gating errors, guttural muscles, etc.) is also prevalent. Despite many displacement sources found in the series, the proposed approach was able to estimate and compensate motion throughout the whole frame and, importantly, in the myocardial region to a degree surpassing a current commercial solution for all types of sequences. Importantly, one of the key quantitative perfusion metric used for diagnosis, namely sectoral perfusion dynamics, was not significantly affected by the MOCO due to the LDOF’s permissibility of varying pixel intensity fluctuations and the post-hoc exact histogram specification step. This highlights the interpolation warping scheme’s weakness as signal intensities were attenuated in the MOCO series with relatively large motion prior to the histogram matching correction step.

The framework was also able to handle the low-resolution, high-dynamic range AIF auxiliary series, which subsequently permitted the development of an automatic AIF signal measurement process using ICA [106]. In that method, the stationary position of the LV in the MOCO series allows its automatic detection and segmentation to track the cavity’s signal variation during bolus transit. This framework is currently being extended to detect the RV and myocardial tissue as well, both possible because of the MOCO preprocessing step. These are critical innovations to fully automate quantitative perfusion analysis to produce high-resolution pixel maps.

The proposed MOCO system was also extended to register PD images to the perfusion T1 series, which precludes MR bias-field normalization. For this application, the hypothesized reduction-to-unimodality-inspired approach using proxy images was necessary to bridge both series together. These were constructed to enhance gradient information and match photometric distributions. Although the LDOF engine was able to register PD images to T1 series without this step in certain configurations during informal testing, the proxy image formulation normalizes the appearances regardless of the sequence types that are continuously being refined. This essentially guarantees compatibility to future CMR image types and continuously refined sequence parameters.

Overall, the proposed MOCO system attained its stated requirements in terms of clinical applicability and operational ergonomics. Its validation on a large patient cohort encompassing a wide range of acquisition parameters further solidifies its clinical appeal. As such, the system was integrated in the diagnosis pipeline for research-level studies at the National Heart, Lung, and Blood Institute at the National Health Institutes’ main clinical center (Bethesda, Maryland, USA).

The MOCO framework presents some limitations. Foremost, the quality of the compensation

is directly related to the precision of the deformation estimations by the LDOF engine. Although the proposed formulation was shown to significantly reduce frame-to-frame motion, some residual movement of diffuse, structure-poor regions is still present, notably in areas peripheral to the myocardium. Although these regions are of no consequence to perfusion analysis, their persistent motion is a noteworthy issue that may hinder MOCO in certain modalities such as US series, where structural information is relatively poor.

Another issue is the optimization of the various parameters controlling the quality of the motion estimates. We have used an automatic grid-search approach to find globally optimal combinations of the parameters, but this step is time-consuming and dependent on the variability of the data used for training. Re-estimation as newer CMR sequence types are developed may be needed. The approach of global optimization on whole series is also an area ripe for improvement. In its current state, the parameters are searched to find the best combination of values that do not create distortions in the flow fields over the full series. With this approach, a contentious pair of images that requires less aggressive LDOF settings will dictate the parameter values for the whole series. In other words, the parameters are only as good as the ones required for the “weakest” pair. This step could be refined by considering a locally-adaptive optimization scheme where the parameters are tuned *on-the-fly* for each sequential image pair. This approach would add a significant computational load that could, however, be mitigated by offloading processing to massively-parallel architectures such as graphical processing units (GPU).

7.0.2 Automatic coronary artery segmentation

The term *universal* used above is further justified as the MOCO framework was successfully applied to x-ray angiographic series. This resulted in motion compensated end-diastolic images that contained frame-to-frame deformations primarily related to respiration, myocardial movement, and ECG gating errors. The performance of the nonrigid MOCO system is particularly apparent in certain series where ECG gating failed to capture the arteries at the same cardiac phase. In these cases, the MOCO effectively *uncoiled* the vessels to match their structural geometry from one frame to another.

The alignment of the arteries throughout the end-diastolic series led to the precise tracking of the propagation of the contrast agent to isolate the arterial tree region from the frame’s background. We labeled this process *motion masking* and it was shown to eliminate background artefacts such as bones and opaque organ regions still present after curvilinear structure extraction using a fast formulation of steerable anisotropic Gaussian filters. The performance of this filtering scheme was aided by adequate preprocessing to mitigate image graininess

with a wavelet-based filtering scheme tuned to tackle the Poisson distribution of the noise. This step was shown to boost SNR, which is increasingly important as low-dose exposures are increasingly favored in clinical protocols. Intra-region illumination normalization was also performed to remove apparent vessel tortuosity and shading from soft-tissue superposition. Finally, diseased regions dissimilar to tubular structures such as aneurysms and ectasic vessels were naturally ill-segmented and thus required the development of a pathological area filling routine. This post-hoc processing step successfully completed the segmentation result on every lesion present in the testing cohort.

As one of the main stated goals of this thesis is to objectify metric extraction used for diagnosis, an automatic caliber measurement routine was developed using the segmentation result. We evaluated the precision of the segmentation by comparing vessel calibers measured manually with commercial electronic calipers, semi-automatically with a commercial region-growing based system, and automatically by the proposed approach. No statistically significant discrepancies were noted and excellent metric agreement was found between our system and the two commercial platforms. Further, processing and caliber computation times were generally an order of magnitude faster than the operator-dependent measurements.

The main issue related to this framework is qualitative, as some non-vessel structures are still present in the final segmentation result. The combination of a vessel-like appearance and enclosure in the motion mask results in the inclusion of the catheter and other tube-like structures in certain cases. Although these artefacts are easily identifiable by visual inspection, they are nonetheless an unwanted presence in terms of future development such as 3D arterial tree reconstruction (presented in Section 8.1.3).

Furthermore, as with the case for the MOCO system, many parameters are needed to control various efficiency and quality aspects of the system. These were determined empirically on a small subset of series and automatic parameter selection strategies as used above may be implemented.

7.0.3 Coronary artery distensibility assessment via angiographic series

The precise and automatic nature of the CA segmentation approach led to the hypothesis that this framework could be used as a precursory step to measure the temporal variations of vessel calibers over a cardiac cycle. Our CA distensibility assessment system was thus developed by using the segmentation result in an operator-selected region and tracking vessel boundary points from frame-to-frame using HOG landmark matching similar to the implementation used in the LDOF engine. Here again, the spatiotemporal information found in the angiographic series is leveraged to ultimately provide clinically relevant information related

to vascular health.

Indeed, the two pilot studies utilizing this tool have shown its diagnostic potential. In the first study, the system was able to identify and, furthermore, stratify arterial wall sequelae in a cohort of healthy and KD patients with and without aneurysmal history. Our hypothesis were verified in terms of increased vessel stiffness for KD patients and exacerbated rigidity for those with a history of aneurysmal lesions. These results concur with invasive modalities of previous studies and motivated the expansion of our testing to a larger cohort of KD patients who underwent OCT imaging. Here, the number of observed, expert-rated lesions correlated significantly with the distensibility metrics measured independently using the proposed approach.

The physiologically-expected results obtained in these two preliminary studies compel an expanded evaluation of this tool to other vascular pathologies such as atherosclerosis in adult patients. Vascular stiffness assessment may thus be used conjointly with traditional obstruction quantification, but its potential may be further distinguished as it may elucidate early onset of pathology in patients with normal-looking arteries.

An important limitation of this approach is related to the characteristics of the angiographic series under study. The targeted vascular segment must fully contain contrast agent during a whole cardiac cycle. This may pose a problem for dilated vessels, where the contrast fluid may maximally fill the targeted region for too few frames or none at all. However, this issue may be mitigated prospectively if the physician adjusts bolus administration quantity during acquisition. In addition, issues may be encountered if vessels overlap each other during the cardiac cycle time window. In this case, the HOG-based tracking may fail. This too, however, may be mitigated if the angular acquisition parameters are adjusted appropriately during recording.

Another issue is related to the geometry of the arterial segments under study. Although it is sensible to assume circular or elliptical cross-sections of healthy vessels where expansion and recoil will occur pseudo-uniformly over a large, diffuse portion of the vascular wall, pathological segments affected by dilations or atherosclerosis will invariably cause non-uniform, focal zones of varying elastic properties and luminal geometry. In these cases, the 2D nature of the angiographic projections may not correctly estimate the non-uniform dynamics of the vessel wall. Mitigation of this issue may be accomplished by reconstructing the 3D geometry of the segment under study using multiple 2D projections acquired under different angular imaging configurations, as described in Section 8.1.3. The caliber variations measured from each 2D view may then be integrated in the 3D reconstruction of the arteries to provide a more insightful and complete assessment of the distensibility.

The manual step of region selection is also problematic as the operator is essentially “blindly” placing the ROI where distensibility may be affected. As such, concerning vessel segments may be missed. This is admittedly an important weakness of the system as it counters this thesis’ paradigm of operator-free metric extraction. Nonetheless, the early and exploratory nature of this tool justified this design decision and the encouraging results have motivated the correction of this limitation by tracking the caliber variability on the whole arterial tree.

Finally, the preliminary state of this system presents fundamental physiology-metric issues. The distensibility measures we have obtained in the two studies were analyzed in a relative mode. That is, the different groups in our cohorts were compared exclusively between each other in a very specific and closed manner. As such, we do not know what are absolute values for healthy or pathological distensibility results. Many more patients from multiple centers need to be studied to start formulating population-wide ranges for the various stiffness metrics we have proposed.

CHAPTER 8 CONCLUSION

The underlying approach presented in this thesis is directed to the application of the engineering practice to better the diagnosis of CAD via spatiotemporal information management and integration to ultimately enhance cardiac imaging and extract objective, clinically-relevant metrics. We believe the tools developed here will contribute to limit operator subjectivity, increase analysis efficiency, and stem into other projects with the common singular goal of improving the outcome of sick people.

Specifically, in the case of CMR perfusion imaging, the proposed MOCO system is a critical precursor to fully automatic quantitative perfusion analysis, but ancillary to this, and perhaps generally more relatable, is the system’s robustness to patient breathing and reasonable movement during acquisition. The implications of this is not only increased patient comfort, but the potential to limit or rationalize sedation typically required for pediatric patients undergoing MRI.

For the automatic segmentation framework, the approach consisted of utilizing information usually discarded, but nonetheless acquired at the cost of radiological patient exposure. The translation of the motion compensation pipeline developed for CMR perfusion imaging, coupled with spatiotemporal bolus tracking in the end-diastole frames of the angiographic series and post-hoc aneurysm detection was shown to be a valid method to produce accurate CA segmentation results robust to pathology.

The capstone and last translational development phase of this work is the integration of the CA segmentation algorithm with, again, spatiotemporal analysis in the form of arterial wall tracking to extract apparent vessel stiffness metrics potentially valuable in diagnosis.

8.1 Future developments

We believe the methods, tools, and paradigms developed in this thesis may be expanded to other promising applications, modalities and domains. Some ideas are proposed in the following sections for each theme of this thesis.

8.1.1 Motion compensation and registration

The MOCO system was shown to be adaptable to two different cardiac imaging applications, but may be also used in other study types such as tumor perfusion in the liver, prostate, or lungs, for example. In terms of classical image registration, the system may also be tested in

other multimodal applications where nonrigid deformations are present. CT to MRI registration of the heart, where large elastic deformations may be present would potentially benefit from the capabilities of the MOCO system. At a finer scale, it may be clinically valuable to register 3D reconstructions of the CA between these two modalities. Here, one could imagine the fusion of arterial calcification detected by the CT data with the high resolution structural data provided by MRI.

At a higher operational level, we believe the system can be used to alleviate patient stress by permitting free-breathing and reasonable movement during image acquisition. Anecdotally, this was the wish of many MRI technicians we've worked with during this project. As mentioned earlier, movement constraints are taxing for patients and incur a considerable burden on clinical resources. This issue is particularly interesting for pediatric patients, where pre-scan sedation may be rationalized and perhaps eliminated.

Finally, we postulate that the MOCO framework may be used outside of the medical domain. Indeed, informal experimentations were conducted on astronomical image of planetary time-lapse series where telescope gantry movement and large optical aberrations caused by the long focal length lenses distorted surface features. The MOCO system was able to effectively compensate for these issues and may thus be expanded to this field. In other tests, hand-held videos captured by cellphones were reduced of camera shake.

8.1.2 Extended distensibility analysis

The adult portion of CAD is largely related to atherosclerosis. However, as presented earlier, accrued arterial stiffness may be present despite patent visual angiographic findings. In these situations, the proposed tool could be used as an indicator and perhaps a predictor of early onset atherosclerosis. In addition, for patients who underwent interventional therapy, distensibility assessment is an important metric to evaluate the relatively new class of reabsorbable vascular implants [218], where their clinical allure lies in the promise of recovered vessel elasticity following scaffold absorption. The presented framework may thus be used longitudinally during patient follow-up, where angiograms are routinely performed.

8.1.3 3D reconstruction of the coronary tree

As presented in this thesis, current diagnostic guidelines rely largely on anatomy-based measures from the 2D projections of x-ray angiographic series. For example, in the assessment of stenosis severity or to stratify the risk of complications when aneurysms are present. Three-dimensional reconstructions are a complete, navigable metric representation affording greater

diagnostic potential. The reconstruction can be used to encapsulate computational fluid dynamics (CFD) simulations of blood flow by integrating the dynamic features empirically extracted from the propagation of the contrast agent. Aside from diagnostic purposes, in the context of interventional procedures such as angioplasty or stenting, accurate volumetric, orientation, and absolute cross-sectional vessel information is crucial for both planning and maneuvering. This data is inherently difficult to estimate from 2D projections and would thus benefit from the 3D reconstruction of the CA.

By combining the vessel segmentation results associated with different geometric configurations of the radiographic imaging system, 3D reconstruction of the arterial tree is feasible using self-calibration [38] and a sequential space carving algorithms. Concomitant to this technique, temporal and spacial adjustment using both the ECG and the MOCO system could be used to align the morphological phase of the arterial trees between each views.

The basics of the space-carving approach borrows from the computer vision technique named Shape from Silhouette (SFS) [14, 140]. The fundamental idea is to compute the intersecting volume obtained from the volumetric projection cones of the elements of interest captured from varying views around an object. Applied to coronary artery reconstruction, the rotational acquisition nature of the angiograms captured with C-arm imaging platforms theoretically lends well to this type of reconstruction and was attempted by [90] from the LIV4D laboratory at Polytechnique Montreal. They first reconstructed an arterial tree using simulated 2D silhouettes and ideal imaging parameters to achieve impressive and fast 3D reconstructions (typically sub-minute renderings). However, using real patient data and a Frangi-based CA segmentation (presented in Section 2.4.2), the renderings were noisy and ultimately unusable. This was largely due to the poor segmentation quality and mis-alignment errors. The methods proposed in this thesis may help in these two critical areas, namely the motion-phase synchronization of the vessels across the multiple views and the precise segmentation of the CA, including pathological regions.

On the issue of persistent non-vessel artefacts in the segmentation results of the proposed framework, the 3D reconstruction using the SFS technique may be useful in improving the 2D segmentation results. For example, the presence of the catheter in one segmented image may not be present in the segmentation result of a different angular view. As such, the space carving step would eliminate the artefact in the 3D rendering. The model may then be re-projected to the 2D frames, where only intersecting re-projected voxels and image pixels would be conserved. Used in the SFS framework, the multiple 2D images of the segmented arterial tree captured around the patient thus serve as *mutual disambiguation* data to improve the segmentation result.

Rheological analysis

The use of CFD applied to blood flow can be used to investigate the role of hemodynamic forces in the formation of atherosclerosis in the coronary and carotid arteries [176, 130], to identify flow patterns in aortic aneurysms [243, 244], for pre-operative planing [242, 245], and to elucidate the results of endovascular therapies [147, 83, 85]. As mentioned earlier, in the context of vascular disease, hemodynamic factors can potentially help elucidate the cardiac outcome of patients.

We postulate that thrombogenesis risk can be better predicted by the simulation and analysis of blood flow dynamics using the 3D reconstruction of a patient’s arterial tree and bolus bolus tracking. A data-driven approach that combines both patient-specific anatomy from SFS rendering and blood dynamics from the angiograms could thus be envisioned.

8.2 Recommendations and perspectives

In fluoroscopic imaging, rationalizing patient exposure by triggering acquisition at only end-diastolic time points may be recommended as 1) calibers are typically manually measured on an end-diastolic frame; and 2) fully automatic and high quality CA segmentation can be realized using only end-diastolic images.

The distensibility assessment tool could also be used to study other vascular regions prone to wall pathology or aneurysmal development. These could include, for example, the aorta, cerebral, or renal arteries. As mentioned in Section 6.1, the tool could also be extended to study recovering vessel segments following interventional procedures in both children and adult populations.

At a higher level, an important design recommendation is the development of generalizable frameworks, as was the case for the proposed MOCO system, where it was successfully applied to the angiographic data to facilitate spatiotemporal analysis and ultimately enhance the segmentation result. Lastly, as a general perspective of my experience of this doctoral work, I may put forth that although the development and incremental improvement of fundamental algorithms is capitally important, they are ultimately of little worth if they are not translated into real-world applications. I believe a biomedical engineering doctoral project should strive to have clinical impact. As such, the culmination of the proposed algorithms in this thesis resulted in the CA distensibility assessment tool and two preliminary clinical studies. This last phase, with potentially interesting real-world applicability was, on a personal level, the most rewarding of all.

BIBLIOGRAPHY

- [1] N. A. Ablitt, J. Gao, J. Keegan, L. Stegger, D. N. Firmin, et G.-Z. Yang, “Predictive cardiac motion modeling and correction with partial least squares regression”, *Medical Imaging, IEEE Transactions on*, vol. 23, no. 10, pp. 1315–1324, 2004.
- [2] G. Adluru, E. V. DiBella, et M. C. Schabel, “Model-based registration for dynamic cardiac perfusion mri”, *Journal of Magnetic Resonance Imaging*, vol. 24, no. 5, pp. 1062–1070, 2006.
- [3] L. Ait-Ali, M. G. Andreassi, I. Foffa, I. Spadoni, E. Vano, et E. Picano, “Cumulative patient effective dose and acute radiation-induced chromosomal dna damage in children with congenital heart disease”, *Heart*, vol. 96, no. 4, pp. 269–274, 2010.
- [4] Y. Amit, “Graphical shape templates for automatic anatomy detection with applications to mri brain scans”, *Medical Imaging, IEEE Transactions on*, vol. 16, no. 1, pp. 28–40, 1997.
- [5] M. G. Andreassi, “Radiation risk from pediatric cardiac catheterization friendly fire on children with congenital heart disease”, *Circulation*, vol. 120, no. 19, pp. 1847–1849, 2009.
- [6] M. G. Andreassi, A. Cioppa, S. Manfredi, C. Palmieri, N. Botto, et E. Picano, “Acute chromosomal dna damage in human lymphocytes after radiation exposure in invasive cardiovascular procedures”, *European heart journal*, 2007.
- [7] D. Atkinson, D. Burstein, et R. Edelman, “First-pass cardiac perfusion : evaluation with ultrafast mr imaging.” *Radiology*, vol. 174, no. 3, pp. 757–762, 1990.
- [8] M. A. Audette, F. P. Ferrie, et T. M. Peters, “An algorithmic overview of surface registration techniques for medical imaging”, *Medical image analysis*, vol. 4, no. 3, pp. 201–217, 2000.
- [9] F. Auricchio, M. Conti, C. Ferrazzano, et G. A. Sgueglia, “A simple framework to generate 3d patient-specific model of coronary artery bifurcation from single-plane angiographic images”, *Computers in Biology and Medicine*, vol. 44, no. 0, pp. 97 – 109, 2014.

- [10] S. R. Aylward et E. Bullitt, “Initialization, noise, singularities, and scale in height ridge traversal for tubular object centerline extraction”, *Medical Imaging, IEEE Transactions on*, vol. 21, no. 2, pp. 61–75, 2002.
- [11] R. Bajcsy, R. Lieberman, et M. Reivich, “A computerized system for the elastic matching of deformed radiographic images to idealized atlas images.” *Journal of computer assisted tomography*, vol. 7, no. 4, pp. 618–625, 1983.
- [12] S. Baker, D. Scharstein, J. Lewis, S. Roth, M. J. Black, et R. Szeliski, “A database and evaluation methodology for optical flow”, *International Journal of Computer Vision*, vol. 92, no. 1, pp. 1–31, 2011.
- [13] R. H. Bamberger et M. J. Smith, “A filter bank for the directional decomposition of images : Theory and design”, *Signal Processing, IEEE Transactions on*, vol. 40, no. 4, pp. 882–893, 1992.
- [14] B. G. Baumgart, “Geometric modeling for computer vision.” DTIC Document, Rapp. tech., 1974.
- [15] H. Bay, A. Ess, T. Tuytelaars, et L. Van Gool, “Speeded-up robust features (surf)”, *Computer vision and image understanding*, vol. 110, no. 3, pp. 346–359, 2008.
- [16] N. Begent et G. Born, “Growth rate in vivo of platelet thrombi, produced by iontophoresis of adp, as a function of mean blood flow velocity”, *Nature*, vol. 227, pp. 926–930, 1970.
- [17] M. Benovoy, M. Jacobs, F. Cheriet, N. Dahdah, A. E. Arai, et L.-Y. Hsu, “Automatic nonrigid motion correction for quantitative first-pass cardiac mr perfusion imaging”, dans *Biomedical Imaging (ISBI), 2015 IEEE 12th International Symposium on*. IEEE, 2015, pp. 1588–1591.
- [18] M. Benovoy, A. Dionne, F. Cheriet, R. L. Maurice, et N. Dahdah, “Correlation between automatic angio-based coronary artery stiffness assessment and visual oct pathology scoring”, *Journal of the American College of Cardiology*, vol. 67, no. 13_S, pp. 1672–1672, 2016.
- [19] A. C. Berg, T. L. Berg, et J. Malik, “Shape matching and object recognition using low distortion correspondences”, dans *Computer Vision and Pattern Recognition, 2005. CVPR 2005. IEEE Computer Society Conference on*, vol. 1. IEEE, 2005, pp. 26–33.

- [20] L. M. Bidaut et J.-P. Vallée, “Automated registration of dynamic mr images for the quantification of myocardial perfusion”, *Journal of magnetic resonance imaging*, vol. 13, no. 4, pp. 648–655, 2001.
- [21] D. Bluestein, M. Dewanjee, L. Niu, et R. Schoepfoerster, “Steady flow in an aneurysm model : correlation between fluid dynamics and blood platelet deposition”, *Journal of biomechanical engineering*, vol. 118, no. 3, pp. 280–286, 1996.
- [22] F. L. Bookstein, “Principal warps : Thin-plate splines and the decomposition of deformations”, *IEEE Transactions on Pattern Analysis & Machine Intelligence*, no. 6, pp. 567–585, 1989.
- [23] R. Bordawekar, U. Bondhugula, et R. Rao, “Can cpus match gpus on performance with productivity ? : experiences with optimizing a flop-intensive application on cpus and gpu”, *Res. rep. RC25033, IBM TJ Watson Research Center*, 2010.
- [24] L. Bracoud, F. Vincent, C. Pachai, E. Canet, P. Croisille, et D. Revel, “Automatic registration of mr first-pass myocardial perfusion images”, dans *Functional Imaging and Modeling of the Heart*. Springer, 2003, pp. 215–223.
- [25] R. C. Brasch, W.-R. Press, et G. E. Wesbey, “Characteristics of gadolinium-dtpa complex : A potential nmr contrast agent”, *Classic Papers in Modern Diagnostic Radiology*, p. 417, 2004.
- [26] W. R. Brody, “Digital subtraction angiography”, *Nuclear Science, IEEE Transactions on*, vol. 29, no. 3, pp. 1176–1180, 1982.
- [27] M. M. Bronstein, A. M. Bronstein, F. Michel, et N. Paragios, “Data fusion through cross-modality metric learning using similarity-sensitive hashing”, 2010.
- [28] T. Brox et J. Malik, “Large displacement optical flow : descriptor matching in variational motion estimation”, *Pattern Analysis and Machine Intelligence, IEEE Transactions on*, vol. 33, no. 3, pp. 500–513, 2011.
- [29] T. Brox, A. Bruhn, N. Papenberg, et J. Weickert, “High accuracy optical flow estimation based on a theory for warping”, dans *Computer Vision-ECCV 2004*. Springer, 2004, pp. 25–36.
- [30] T. Butz et J.-P. Thiran, “Affine registration with feature space mutual information”, dans *Medical Image Computing and Computer-Assisted Intervention-MICCAI 2001*. Springer, 2001, pp. 549–556.

- [31] T. M. Buzug et J. Weese, “Voxel-based similarity measures for medical image registration in radiological diagnosis and image guided surgery”, *CIT. Journal of computing and information technology*, vol. 6, no. 2, pp. 165–179, 1998.
- [32] P. Cachier, E. Bardinet, D. Dormont, X. Pennec, et N. Ayache, “Iconic feature based nonrigid registration : the pasha algorithm”, *Computer vision and image understanding*, vol. 89, no. 2, pp. 272–298, 2003.
- [33] F. Cademartiri, L. La Grutta, A. Palumbo, P. Malagutti, F. Pugliese, W. B. Meijboom, T. Baks, N. R. Mollet, N. Bruining, R. Hamers *et al.*, “Non-invasive visualization of coronary atherosclerosis : state-of-art”, *Journal of Cardiovascular Medicine*, vol. 8, no. 3, pp. 129–137, 2007.
- [34] A. Can, C. V. Stewart, B. Roysam, et H. L. Tanenbaum, “A feature-based, robust, hierarchical algorithm for registering pairs of images of the curved human retina”, *Pattern Analysis and Machine Intelligence, IEEE Transactions on*, vol. 24, no. 3, pp. 347–364, 2002.
- [35] C. G. Caro, *The mechanics of the circulation*. Cambridge University Press, 2012.
- [36] V. Caselles, R. Kimmel, et G. Sapiro, “Geodesic active contours”, *International journal of computer vision*, vol. 22, no. 1, pp. 61–79, 1997.
- [37] H. Chen et J. Hale, “An algorithm for mr angiography image enhancement”, *Magnetic resonance in medicine*, vol. 33, no. 4, pp. 534–540, 1995.
- [38] F. Cheriet et J. Meunier, “Self-calibration of a biplane x-ray imaging system for an optimal three dimensional reconstruction”, *Computerized medical imaging and graphics*, vol. 23, no. 3, pp. 133–141, 1999.
- [39] W. Chilcote, M. Modic, W. Pavlicek, J. Little, A. Furlan, P. Duchesneau, et M. Weinstein, “Digital subtraction angiography of the carotid arteries : a comparative study in 100 patients.” *Radiology*, vol. 139, no. 2, pp. 287–295, 1981.
- [40] G. E. Christensen, B. Carlson, K. C. Chao, P. Yin, P. W. Grigsby, K. Nguyen, J. F. Dempsey, F. A. Lerma, K. T. Bae, M. W. Vannier *et al.*, “Image-based dose planning of intracavitary brachytherapy : registration of serial-imaging studies using deformable anatomic templates”, *International Journal of Radiation Oncology* Biology* Physics*, vol. 51, no. 1, pp. 227–243, 2001.

- [41] G. E. Christensen, X. Geng, J. G. Kuhl, J. Bruss, T. J. Grabowski, I. A. Pirwani, M. W. Vannier, J. S. Allen, et H. Damasio, “Introduction to the non-rigid image registration evaluation project (nirep)”, *Lecture Notes in Computer Science*, vol. 4057, pp. 128–135, 2006.
- [42] H. Chui et A. Rangarajan, “A new point matching algorithm for non-rigid registration”, *Computer Vision and Image Understanding*, vol. 89, no. 2, pp. 114–141, 2003.
- [43] A. C. Chung, W. M. Wells III, A. Norbash, et W. E. L. Grimson, “Multi-modal image registration by minimising kullback-leibler distance”, dans *Medical Image Computing and Computer-Assisted Intervention—MICCAI 2002*. Springer, 2002, pp. 525–532.
- [44] O. R. Coelho-Filho, C. Rickers, R. Y. Kwong, et M. Jerosch-Herold, “Mr myocardial perfusion imaging”, *Radiology*, vol. 266, no. 3, pp. 701–715, 2013.
- [45] A. Collignon, F. Maes, D. Delaere, D. Vandermeulen, P. Suetens, et G. Marchal, “Automated multi-modality image registration based on information theory”, dans *Information processing in medical imaging*, vol. 3, no. 6, 1995, pp. 263–274.
- [46] A. Colombo, P. Hall, S. Nakamura, Y. Almagor, L. Maiello, G. Martini, A. Gaglione, S. L. Goldberg, et J. M. Tobis, “Intracoronary stenting without anticoagulation accomplished with intravascular ultrasound guidance”, *Circulation*, vol. 91, no. 6, pp. 1676–1688, 1995.
- [47] D. Coltuc, P. Bolon, et J.-M. Chassery, “Exact histogram specification”, *Image Processing, IEEE Transactions on*, vol. 15, no. 5, pp. 1143–1152, 2006.
- [48] C. B. Compas, T. Syeda-Mahmood, P. McNeillie, et D. Beymer, “Automatic detection of coronary stenosis in x-ray angiography through spatio-temporal tracking”, dans *Biomedical Imaging (ISBI), 2014 IEEE 11th International Symposium on*. IEEE, 2014, pp. 1299–1302.
- [49] A. Comte, A. Lalande, S. Aho, P. M. Walker, et F. Brunotte, “Realignment of myocardial first-pass mr perfusion images using an automatic detection of the heart-lung interface”, *Magnetic resonance imaging*, vol. 22, no. 7, pp. 1001–1009, 2004.
- [50] R. Coppi, P. D’Urso, et P. Giordani, “A fuzzy clustering model for multivariate spatial time series”, *Journal of Classification*, vol. 27, no. 1, pp. 54–88, 2010.
- [51] T. Craven, J. Ryu, M. Espeland, F. Kahl, W. McKinney, J. Toole, M. McMahan, C. Thompson, G. Heiss, et J. Crouse, “Evaluation of the associations between carotid

- artery atherosclerosis and coronary artery stenosis. a case-control study.” *Circulation*, vol. 82, no. 4, pp. 1230–1242, 1990.
- [52] I. Cruz-Aceves et A. Hernández-Aguirre, “Segmentation of coronary angiograms using a vesselness measure and evolutionary thresholding”, dans *Design of Intelligent Systems Based on Fuzzy Logic, Neural Networks and Nature-Inspired Optimization*. Springer, 2015, pp. 269–289.
 - [53] R. N. Czerwinski, D. L. Jones, et W. D. O’Brien Jr, “An approach to boundary detection in ultrasound imaging”, dans *Ultrasonics Symposium, 1993. Proceedings., IEEE 1993*. IEEE, 1993, pp. 951–955.
 - [54] R. N. Czerwinski, D. L. Jones, et W. O’Brien, “Detection of lines and boundaries in speckle images-application to medical ultrasound”, *Medical Imaging, IEEE Transactions on*, vol. 18, no. 2, pp. 126–136, 1999.
 - [55] N. Dalal et B. Triggs, “Histograms of oriented gradients for human detection”, dans *Computer Vision and Pattern Recognition, 2005. CVPR 2005. IEEE Computer Society Conference on*, vol. 1. IEEE, 2005, pp. 886–893.
 - [56] F. Dallaire et N. Dahdah, “New equations and a critical appraisal of coronary artery z scores in healthy children”, *Journal of the American Society of Echocardiography*, vol. 24, no. 1, pp. 60–74, 2011.
 - [57] L. B. Daniels, J. B. Gordon, et J. C. Burns, “Kawasaki disease : late cardiovascular sequelae”, *Current opinion in cardiology*, vol. 27, no. 6, pp. 572–577, 2012.
 - [58] M. H. Davis, A. Khotanzad, D. P. Flamig, et S. E. Harms, “A physics-based coordinate transformation for 3-d image matching”, *Medical Imaging, IEEE Transactions on*, vol. 16, no. 3, pp. 317–328, 1997.
 - [59] M. Díaz-Zamudio, U. Bacilio-Pérez, M. C. Herrera-Zarza, A. Meave-González, E. Alexanderson-Rosas, G. F. Zambrana-Balta, et E. T. Kimura-Hayama, “Coronary artery aneurysms and ectasia : Role of coronary ct angiography”, *RadioGraphics*, vol. 29, no. 7, pp. 1939–1954, 2009. DOI : 10.1148/rg.297095048
 - [60] M. T. Dehkordi, S. Sadri, et A. Doosthoseini, “A review of coronary vessel segmentation algorithms”, *Journal of medical signals and sensors*, vol. 1, no. 1, p. 49, 2011.
 - [61] R. Deriche, “Fast algorithms for low-level vision”, *Pattern Analysis and Machine Intelligence, IEEE Transactions on*, vol. 12, no. 1, pp. 78–87, 1990.

- [62] F. Di Martino, S. Sessa, U. E. Barillari, et M. R. Barillari, “Spatio-temporal hotspots and application on a disease analysis case via gis”, *Soft Computing*, vol. 18, no. 12, pp. 2377–2384, 2014.
- [63] D. L. Donoho, “De-noising by soft-thresholding”, *Information Theory, IEEE Transactions on*, vol. 41, no. 3, pp. 613–627, 1995.
- [64] C. Dornier, M. K. Ivancevic, P. Thevenaz, et J.-P. Vallée, “Improvement in the quantification of myocardial perfusion using an automatic spline-based registration algorithm”, *Journal of Magnetic Resonance Imaging*, vol. 18, no. 2, pp. 160–168, 2003.
- [65] L. Dougherty, J. C. Asmuth, et W. B. Gefter, “Alignment of ct lung volumes with an optical flow method”, *Academic radiology*, vol. 10, no. 3, pp. 249–254, 2003.
- [66] P. S. Douglas, M. R. Patel, S. R. Bailey, D. Dai, L. Kaltenbach, R. G. Brindis, J. Messenger, et E. D. Peterson, “Hospital variability in the rate of finding obstructive coronary artery disease at elective, diagnostic coronary angiography”, *Journal of the American College of Cardiology*, vol. 58, no. 8, pp. 801–809, 2011.
- [67] Y. P. Du et D. L. Parker, “Vessel enhancement filtering in three-dimensional mr angiograms using long-range signal correlation”, *Journal of Magnetic Resonance Imaging*, vol. 7, no. 2, pp. 447–450, 1997.
- [68] Y. P. Du, D. L. Parker, et W. L. Davis, “Vessel enhancement filtering in three-dimensional mr angiography”, *Journal of Magnetic Resonance Imaging*, vol. 5, no. 3, pp. 353–359, 1995.
- [69] A. J. Einstein et J. Knuuti, “Cardiac imaging : does radiation matter ?” *European heart journal*, vol. 33, no. 5, pp. 573–578, 2012.
- [70] A. C. Evans, S. Marrett, J. Torrescorzo, S. Ku, et L. Collins, “Mri-pet correlation in three dimensions using a volume-of-interest (voi) atlas”, *Journal of Cerebral Blood Flow & Metabolism*, vol. 11, no. 1 suppl, pp. A69–A78, 1991.
- [71] H. Fazlali, N. Karimi, S. Soroushmehr, S. Sinha, S. Samavi, B. Nallamothu, et K. Najarian, “Vessel region detection in coronary x-ray angiograms”, dans *Image Processing (ICIP), 2015 IEEE International Conference on*. IEEE, 2015, pp. 1493–1497.
- [72] A. F. Frangi, W. J. Niessen, R. M. Hoogeveen, T. Van Walsum, et M. A. Viergever, “Model-based quantitation of 3-d magnetic resonance angiographic images”, *Medical Imaging, IEEE Transactions on*, vol. 18, no. 10, pp. 946–956, 1999.

- [73] W. T. Freeman et E. H. Adelson, “The design and use of steerable filters”, *IEEE Transactions on Pattern analysis and machine intelligence*, vol. 13, no. 9, pp. 891–906, 1991.
- [74] H. Fujiwara et Y. Hamashima, “Pathology of the heart in kawasaki disease”, *Pediatrics*, vol. 61, no. 1, pp. 100–107, 1978.
- [75] S. Gaffney et P. Smyth, “Trajectory clustering with mixtures of regression models”, dans *Proceedings of the fifth ACM SIGKDD international conference on Knowledge discovery and data mining*. ACM, 1999, pp. 63–72.
- [76] J. E. Gage, O. Hess, T. Murakami, M. Ritter, J. Grimm, et H. Krayenbuehl, “Vasoconstriction of stenotic coronary arteries during dynamic exercise in patients with classic angina pectoris : reversibility by nitroglycerin.” *Circulation*, vol. 73, no. 5, pp. 865–876, 1986.
- [77] K. P. Gall, L. J. Verhey, et M. Wagner, “Computer-assisted positioning of radiotherapy patients using implanted radiopaque fiducials”, *Medical physics*, vol. 20, no. 4, pp. 1153–1159, 1993.
- [78] Y. Gao et H. Sundar, “Coronary arteries motion modeling on 2d x-ray images”, dans *SPIE Medical Imaging*. International Society for Optics and Photonics, 2012, pp. 83 161A–83 161A.
- [79] P. D. Gatehouse, A. G. Elkinson, N. A. Ablitt, G.-Z. Yang, D. J. Pennell, et D. N. Firmin, “Accurate assessment of the arterial input function during high-dose myocardial perfusion cardiovascular magnetic resonance”, *Journal of Magnetic Resonance Imaging*, vol. 20, no. 1, pp. 39–45, 2004.
- [80] B. L. Gerber, S. V. Raman, K. Nayak, F. H. Epstein, P. Ferreira, L. Axel, et D. L. Kraitchman, “Myocardial first-pass perfusion cardiovascular magnetic resonance : history, theory, and current state of the art”, *Journal of Cardiovascular Magnetic Resonance*, vol. 10, no. 1, p. 18, 2008.
- [81] J.-M. Geusebroek, A. W. Smeulders, et J. Van De Weijer, “Fast anisotropic gauss filtering”, *Image Processing, IEEE Transactions on*, vol. 12, no. 8, pp. 938–943, 2003.
- [82] A. S. Go, D. Mozaffarian, V. L. Roger, E. J. Benjamin, J. D. Berry, W. B. Borden, D. M. Bravata, S. Dai, E. S. Ford, C. S. Fox *et al.*, “Heart disease and stroke statistics—2013

- update a report from the american heart association”, *Circulation*, vol. 127, no. 1, pp. e6–e245, 2013.
- [83] Y. Gobin, J. Counord, P. Flaud, et J. Duffaux, “In vitro study of haemodynamics in a giant saccular aneurysm model : influence of flow dynamics in the parent vessel and effects of coil embolisation”, *Neuroradiology*, vol. 36, no. 7, pp. 530–536, 1994.
- [84] J. Gordon, P. Ganz, E. Nabel, R. Fish, J. Zebede, G. Mudge, R. Alexander, et A. Selwyn, “Atherosclerosis influences the vasomotor response of epicardial coronary arteries to exercise.” *Journal of Clinical Investigation*, vol. 83, no. 6, p. 1946, 1989.
- [85] V. B. Graves, C. M. Strother, C. R. Partington, et A. Rappe, “Flow dynamics of lateral carotid artery aneurysms and their effects on coils and balloons : an experimental study in dogs.” *American journal of neuroradiology*, vol. 13, no. 1, pp. 189–196, 1992.
- [86] S. E. Grigorescu, N. Petkov, et P. Kruizinga, “Comparison of texture features based on gabor filters”, *Image Processing, IEEE Transactions on*, vol. 11, no. 10, pp. 1160–1167, 2002.
- [87] S. N. Gupta, M. Solaiyappan, G. M. Beache, A. E. Arai, et T. K. Foo, “Fast method for correcting image misregistration due to organ motion in time-series mri data”, *Magnetic Resonance in Medicine*, vol. 49, no. 3, pp. 506–514, 2003.
- [88] V. Gupta, H. A. Kirişli, E. A. Hendriks, R. J. van der Geest, M. van de Giessen, W. Niessen, J. H. Reiber, et B. P. Lelieveldt, “Cardiac mr perfusion image processing techniques : A survey”, *Medical Image Analysis*, vol. 16, no. 4, pp. 767–785, 2012.
- [89] E. Haber, J. Modersitzki *et al.*, “Intensity gradient based registration and fusion of multi-modal images”, *Methods of information in medicine*, vol. 46, no. 3, pp. 292–299, 2007.
- [90] S. Habert, N. Dahdah, et F. Cheriet, “A novel method for an automatic 3d reconstruction of coronary arteries from angiographic images”, dans *Information Science, Signal Processing and their Applications (ISSPA), 2012 11th International Conference on*. IEEE, 2012, pp. 484–489.
- [91] S. Hamrouni, N. Rougon, et F. Prêteux, “Multi-feature information-theoretic image registration : application to groupwise registration of perfusion mri exams”, dans *Biomedical Imaging : From Nano to Macro, 2011 IEEE International Symposium on*. IEEE, 2011, pp. 574–577.

- [92] C. Harris et M. Stephens, “A combined corner and edge detector.” dans *Alvey vision conference*, vol. 15. Citeseer, 1988, p. 50.
- [93] M. P. Heinrich, M. Jenkinson, M. Bhushan, T. Martin, F. V. Gleeson, M. Brady, et J. A. Schnabel, “Mind : Modality independent neighbourhood descriptor for multi-modal deformable registration”, *Medical Image Analysis*, vol. 16, no. 7, pp. 1423–1435, 2012.
- [94] F. Heitger, L. Rosenthaler, R. Von Der Heydt, E. Peterhans, et O. Kübler, “Simulation of neural contour mechanisms : from simple to end-stopped cells”, *Vision research*, vol. 32, no. 5, pp. 963–981, 1992.
- [95] P. Hellier et C. Barillot, “Coupling dense and landmark-based approaches for nonrigid registration”, *Medical Imaging, IEEE Transactions on*, vol. 22, no. 2, pp. 217–227, 2003.
- [96] A. Hennemuth, A. Seeger, O. Friman, S. Miller, B. Klumpp, S. Oeltze, et H.-O. Peitgen, “A comprehensive approach to the analysis of contrast enhanced cardiac mr images”, *Medical Imaging, IEEE Transactions on*, vol. 27, no. 11, pp. 1592–1610, 2008.
- [97] D. M. Herrington, M. Siebes, D. K. Sokol, C. O. Siu, et G. D. Walford, “Variability in measures of coronary lumen dimensions using quantitative coronary angiography”, *Journal of the American College of Cardiology*, vol. 22, no. 4, pp. 1068–1074, 1993.
- [98] H. M. H. D. Hill DL, Batchelor PG, “Medical image registration”, *Phys. Med. Biol.*, vol. 46, no. 3, pp. 1–45, 2001.
- [99] B. K. Horn et B. G. Schunck, “Determining optical flow”, dans *1981 Technical symposium east*. International Society for Optics and Photonics, 1981, pp. 319–331.
- [100] L.-y. Hsu, K. L. Rhoads, A. H. Aletras, et A. E. Arai, “Surface coil intensity correction and non-linear intensity normalization improve pixel-resolution parametric maps of myocardial mri perfusion”, dans *Medical Image Computing and Computer-Assisted Intervention-MICCAI 2003*. Springer, 2003, pp. 975–976.
- [101] L.-Y. Hsu, D. W. Groves, A. H. Aletras, P. Kellman, et A. E. Arai, “A quantitative pixel-wise measurement of myocardial blood flow by contrast-enhanced first-pass cmr perfusion imaging : microsphere validation in dogs and feasibility study in humans”, *JACC : Cardiovascular Imaging*, vol. 5, no. 2, pp. 154–166, 2012.
- [102] W. M. Hsu, J. F. Hughes, et H. Kaufman, “Direct manipulation of free-form deformations”, dans *ACM Siggraph Computer Graphics*, vol. 26, no. 2. ACM, 1992, pp.

177–184.

- [103] M. Iemura, M. Ishii, T. Sugimura, T. Akagi, et H. Kato, “Long term consequences of regressed coronary aneurysms after kawasaki disease : vascular wall morphology and function”, *Heart*, vol. 83, no. 3, pp. 307–311, 2000.
- [104] H. Izakian, W. Pedrycz, et I. Jamal, “Clustering spatiotemporal data : An augmented fuzzy c-means”, *Fuzzy Systems, IEEE Transactions on*, vol. 21, no. 5, pp. 855–868, 2013.
- [105] —, “Fuzzy clustering of time series data using dynamic time warping distance”, *Engineering Applications of Artificial Intelligence*, vol. 39, pp. 235–244, 2015.
- [106] M. Jacobs, M. Gorbachev, M. Benovoy, L.-C. Chang, A. E. Arai, et L.-Y. Hsu, “Automated measurement of arterial input function in first-pass myocardial perfusion magnetic resonance images using independent component analysis”, dans *Biomedical Imaging (ISBI), 2015 IEEE 12th International Symposium on*. IEEE, 2015, pp. 1332–1335.
- [107] A. R. Jayaweera, K. Wei, M. Coggins, J. P. Bin, C. Goodman, et S. Kaul, “Role of capillaries in determining cbf reserve : new insights using myocardial contrast echocardiography”, *American Journal of Physiology-Heart and Circulatory Physiology*, vol. 277, no. 6, pp. H2363–H2372, 1999.
- [108] B. Jian, B. C. Vemuri, et J. L. Marroquin, “Robust nonrigid multimodal image registration using local frequency maps”, dans *Information Processing in Medical Imaging*. Springer, 2005, pp. 504–515.
- [109] H. Jiang, G. Zhang, H. Wang, et H. Bao, “Spatio-temporal video segmentation of static scenes and its applications”, *Multimedia, IEEE Transactions on*, vol. 17, no. 1, pp. 3–15, 2015.
- [110] L. Juan et O. Gwun, “A comparison of sift, pca-sift and surf”, *International Journal of Image Processing (IJIP)*, vol. 3, no. 4, pp. 143–152, 2009.
- [111] C. Kang, S. Xiang, S. Liao, C. Xu, et C. Pan, “Learning consistent feature representation for cross-modal multimedia retrieval”, *Multimedia, IEEE Transactions on*, vol. 17, no. 3, pp. 370–381, 2015.
- [112] M. Kass, A. Witkin, et D. Terzopoulos, “Snakes : Active contour models”, *International journal of computer vision*, vol. 1, no. 4, pp. 321–331, 1988.

- [113] H. Kato, E. Ichinose, F. Yoshioka, T. Takechi, S. Matsunaga, K. Suzuki, et N. Rikitake, “Fate of coronary aneurysms in kawasaki disease : serial coronary angiography and long-term follow-up study”, *The American journal of cardiology*, vol. 49, no. 7, pp. 1758–1766, 1982.
- [114] H. Kato, E. Ichinose, et T. Kawasaki, “Myocardial infarction in kawasaki disease : clinical analyses in 195 cases”, *The Journal of pediatrics*, vol. 108, no. 6, pp. 923–927, 1986.
- [115] H. Kato, T. Sugimura, T. Akagi, N. Sato, K. Hashino, Y. Maeno, T. Kazue, G. Eto, et R. Yamakawa, “Long-term consequences of kawasaki disease a 10-to 21-year follow-up study of 594 patients”, *Circulation*, vol. 94, no. 6, pp. 1379–1385, 1996.
- [116] Y. Ke et R. Sukthankar, “Pca-sift : A more distinctive representation for local image descriptors”, dans *Computer Vision and Pattern Recognition, 2004. CVPR 2004. Proceedings of the 2004 IEEE Computer Society Conference on*, vol. 2. IEEE, 2004, pp. II–506.
- [117] S. Kelle, A. G. Hays, G. A. Hirsch, G. Gerstenblith, J. M. Miller, A. M. Steinberg, M. Schär, J. H. Texter, E. Wellnhofer, R. G. Weiss *et al.*, “Coronary artery distensibility assessed by 3.0 tesla coronary magnetic resonance imaging in subjects with and without coronary artery disease”, *The American journal of cardiology*, vol. 108, no. 4, pp. 491–497, 2011.
- [118] A. Kerkeni, A. Benabdallah, A. Manzanera, et M. H. Bedoui, “A coronary artery segmentation method based on multiscale analysis and region growing”, *Computerized Medical Imaging and Graphics*, vol. 48, pp. 49–61, 2016.
- [119] F. Khalifa, G. M. Beache, A. Firjani, K. C. Welch, G. Gimel’farb, et A. El-Baz, “A new nonrigid registration approach for motion correction of cardiac first-pass perfusion mri”, dans *Image Processing (ICIP), 2012 19th IEEE International Conference on*. IEEE, 2012, pp. 1665–1668.
- [120] F. Khalifa, G. M. Beache, G. Gimel’farb, et A. El-Baz, “A new nonrigid registration framework for improved visualization of transmural perfusion gradients on cardiac first-pass perfusion mri”, dans *Biomedical Imaging (ISBI), 2012 9th IEEE International Symposium on*. IEEE, 2012, pp. 828–831.
- [121] N. Kingsbury, “The dual-tree complex wavelet transform : a new efficient tool for image restoration and enhancement”, dans *Proc. EUSIPCO*, vol. 98, 1998, pp. 319–322.

- [122] C. Kirbas et F. Quek, “A review of vessel extraction techniques and algorithms”, *ACM Computing Surveys (CSUR)*, vol. 36, no. 2, pp. 81–121, 2004.
- [123] S. Kisilevich, F. Mansmann, M. Nanni, et S. Rinzivillo, *Spatio-temporal clustering*. Springer, 2009.
- [124] A. K. Klein, F. Lee, et A. A. Amini, “Quantitative coronary angiography with deformable spline models”, *Medical Imaging, IEEE Transactions on*, vol. 16, no. 5, pp. 468–482, 1997.
- [125] R. Kliegman, R. Behrman, H. Jenson, B. Stanton, B. Zitelli, et H. Davis, *Nelson Textbook of Pediatrics E-dition, 18th Edition and Atlas of Pediatric Physical Diagnosis, 5th Edition Package*. Elsevier Science Health Science Division, 2007.
- [126] H. Knutsson et M. Andersson, “Morphons : Segmentation using elastic canvas and paint on priors”, dans *Image Processing, 2005. ICIP 2005. IEEE International Conference on*, vol. 2. IEEE, 2005, pp. II–1226.
- [127] J. J. Koenderink et A. Van Doorn, “Receptive field families”, *Biological cybernetics*, vol. 63, no. 4, pp. 291–297, 1990.
- [128] J. Kohlrausch, K. Rohr, et H. S. Stiehl, “A new class of elastic body splines for nonrigid registration of medical images”, *Journal of Mathematical Imaging and Vision*, vol. 23, no. 3, pp. 253–280, 2005.
- [129] C. Kose et C. Ikibas, “Segmentation of coronary vessel structures in x-ray angiogram images by using spatial pattern matching method”, dans *Computer and Information Sciences, 2008. ISCIS’08. 23rd International Symposium on*. IEEE, 2008, pp. 1–6.
- [130] R. Krams, J. Wentzel, J. Oomen, R. Vinke, J. Schuurbiers, P. De Feyter, P. Serruys, et C. Slager, “Evaluation of endothelial shear stress and 3d geometry as factors determining the development of atherosclerosis and remodeling in human coronary arteries in vivo combining 3d reconstruction from angiography and ivus (angus) with computational fluid dynamics”, *Arteriosclerosis, thrombosis, and vascular biology*, vol. 17, no. 10, pp. 2061–2065, 1997.
- [131] K. Krissian, “Flux-based anisotropic diffusion applied to enhancement of 3-d angiogram”, *Medical Imaging, IEEE Transactions on*, vol. 21, no. 11, pp. 1440–1442, 2002.
- [132] K. Krissian, G. Malandain, et N. Ayache, *Directional anisotropic diffusion applied to segmentation of vessels in 3D images*. Springer, 1997.

- [133] D. Krüger, U. Stierle, G. Herrmann, R. Simon, et A. Sheikhzadeh, “Exercise-induced myocardial ischemia in isolated coronary artery ectasias and aneurysms (“dilated coronaropathy”)”, *Journal of the American College of Cardiology*, vol. 34, no. 5, pp. 1461–1470, 1999.
- [134] D. Krüger, N. E. Al Mokhtari, A. Wieckhorst, T. Rausche, G. Simon-Herrmann, et R. Simon, “Evidence of pathological coronary flow patterns in patients with isolated coronary artery aneurysms”, *Coronary artery disease*, vol. 19, no. 4, pp. 249–255, 2008.
- [135] Y. Kuramochi, T. Ohkubo, N. Takechi, D. Fukumi, Y. Uchikoba, et S. Ogawa, “Hemodynamic factors of thrombus formation in coronary aneurysms associated with kawasaki disease”, *Pediatrics International*, vol. 42, no. 5, pp. 470–475, 2000.
- [136] J. Kybic et M. Unser, “Fast parametric elastic image registration”, *Image Processing, IEEE Transactions on*, vol. 12, no. 11, pp. 1427–1442, 2003.
- [137] C. Lacoste, X. Descombes, J. Zerubia, et N. Baghdadi, “Unsupervised line network extraction from remotely sensed images by polyline process”, dans *Proc. EUSIPCO*, 2004.
- [138] C. Lacoste, G. Finet, et I. E. Magnin, “Coronary tree extraction from x-ray angiograms using marked point processes”, dans *Biomedical Imaging : Nano to Macro, 2006. 3rd IEEE International Symposium on*. IEEE, 2006, pp. 157–160.
- [139] D. S. Lara, A. W. Faria, A. de A Araujo, et D. Menotti, “A semi-automatic method for segmentation of the coronary artery tree from angiography”, dans *Computer Graphics and Image Processing (SIBGRAPI), 2009 XXII Brazilian Symposium on*. IEEE, 2009, pp. 194–201.
- [140] A. Laurentini, “The visual hull concept for silhouette-based image understanding”, *Pattern Analysis and Machine Intelligence, IEEE Transactions on*, vol. 16, no. 2, pp. 150–162, 1994.
- [141] D. Lee, M. Hofmann, F. Steinke, Y. Altun, N. D. Cahill, et B. Scholkopf, “Learning similarity measure for multi-modal 3d image registration”, dans *Computer Vision and Pattern Recognition, 2009. CVPR 2009. IEEE Conference on*. IEEE, 2009, pp. 186–193.
- [142] L. Lemieux, N. D. Kitchen, S. W. Hughes, et D. G. Thomas, “Voxel-based localization in frame-based and frameless stereotaxy and its accuracy”, *Medical physics*, vol. 21,

- no. 8, pp. 1301–1310, 1994.
- [143] M. Leordeanu et M. Hebert, “A spectral technique for correspondence problems using pairwise constraints”, dans *Computer Vision, 2005. ICCV 2005. Tenth IEEE International Conference on*, vol. 2. IEEE, 2005, pp. 1482–1489.
 - [144] C. Li, Y. Sun, et P. Chai, “Pseudo ground truth based nonrigid registration of myocardial perfusion mri”, *Medical image analysis*, vol. 15, no. 4, pp. 449–459, 2011.
 - [145] H. Li, B. Manjunath, et S. K. Mitra, “A contour-based approach to multisensor image registration”, *Image Processing, IEEE Transactions on*, vol. 4, no. 3, pp. 320–334, 1995.
 - [146] R. Liao, D. Luc, Y. Sun, et K. Kirchberg, “3-d reconstruction of the coronary artery tree from multiple views of a rotational x-ray angiography”, *The international journal of cardiovascular imaging*, vol. 26, no. 7, pp. 733–749, 2010.
 - [147] B. B. Lieber et M. J. Gounis, “The physics of endoluminal stenting in the treatment of cerebrovascular aneurysms”, *Neurological research*, vol. 24, no. Supplement-1, pp. 33–42, 2002.
 - [148] L. S. Lilly, *Pathophysiology of heart disease : a collaborative project of medical students and faculty*. Wolters Kluwer Health, 2012.
 - [149] J. A. Lima, R. M. Judd, A. Bazille, S. P. Schulman, E. Atalar, et E. A. Zerhouni, “Regional heterogeneity of human myocardial infarcts demonstrated by contrast-enhanced mri potential mechanisms”, *Circulation*, vol. 92, no. 5, pp. 1117–1125, 1995.
 - [150] J. Liu, B. C. Vemuri, et J. L. Marroquin, “Local frequency representations for robust multimodal image registration”, *Medical Imaging, IEEE Transactions on*, vol. 21, no. 5, pp. 462–469, 2002.
 - [151] C. Lorenz, I.-C. Carlsen, T. M. Buzug, C. Fassnacht, et J. Weese, “Multi-scale line segmentation with automatic estimation of width, contrast and tangential direction in 2d and 3d medical images”, dans *CVRMed-MRCAS’97*. Springer, 1997, pp. 233–242.
 - [152] L. M. Lorigo, O. D. Faugeras, W. E. L. Grimson, R. Keriven, R. Kikinis, A. Nabavi, et C.-F. Westin, “Curves : Curve evolution for vessel segmentation”, *Medical Image Analysis*, vol. 5, no. 3, pp. 195–206, 2001.
 - [153] D. G. Lowe, “Distinctive image features from scale-invariant keypoints”, *International journal of computer vision*, vol. 60, no. 2, pp. 91–110, 2004.

- [154] P. L. Ludmer, A. P. Selwyn, T. L. Shook, R. R. Wayne, G. H. Mudge, R. W. Alexander, et P. Ganz, “Paradoxical vasoconstriction induced by acetylcholine in atherosclerotic coronary arteries”, *New England Journal of Medicine*, vol. 315, no. 17, pp. 1046–1051, 1986.
- [155] A. Macovski, *Medical imaging systems*. Prentice-Hall Englewood Cliffs, NJ, 1983, vol. 20.
- [156] F. Maes, A. Collignon, D. Vandermeulen, G. Marchal, et P. Suetens, “Multimodality image registration by maximization of mutual information”, *Medical Imaging, IEEE Transactions on*, vol. 16, no. 2, pp. 187–198, 1997.
- [157] J. Malcolm, Y. Rathi, et A. Tannenbaum, “Graph cut segmentation with nonlinear shape priors”, dans *Image Processing, 2007. ICIP 2007. IEEE International Conference on*, vol. 4. IEEE, 2007, pp. IV–365.
- [158] V. Mani *et al.*, “Survey of medical image registration”, *Journal of Biomedical Engineering and Technology*, vol. 1, no. 2, pp. 8–25, 2013.
- [159] A. Martel, M. Froh, K. Brock, D. Plewes, et D. Barber, “Evaluating an optical-flow-based registration algorithm for contrast-enhanced magnetic resonance imaging of the breast”, *Physics in Medicine and Biology*, vol. 52, no. 13, p. 3803, 2007.
- [160] J. Masci, M. M. Bronstein, A. Bronstein, et J. Schmidhuber, “Multimodal similarity-preserving hashing”, *Pattern Analysis and Machine Intelligence, IEEE Transactions on*, vol. 36, no. 4, pp. 824–830, 2014.
- [161] C. D. Mathers et D. Loncar, “Projections of global mortality and burden of disease from 2002 to 2030”, *PLoS medicine*, vol. 3, no. 11, p. e442, 2006.
- [162] B. W. McCrindle, J. S. Li, L. L. Minich, S. D. Colan, A. M. Atz, M. Takahashi, V. L. Vetter, W. M. Gersony, P. D. Mitchell, J. W. Newburger *et al.*, “Coronary artery involvement in children with kawasaki disease risk factors from analysis of serial normalized measurements”, *Circulation*, vol. 116, no. 2, pp. 174–179, 2007.
- [163] T. McInerney et D. Terzopoulos, “Deformable models in medical image analysis : a survey”, *Medical image analysis*, vol. 1, no. 2, pp. 91–108, 1996.
- [164] ———, “T-snakes : Topology adaptive snakes”, *Medical image analysis*, vol. 4, no. 2, pp. 73–91, 2000.

- [165] R. Megret et D. DeMenthon, “A survey of spatio-temporal grouping techniques”, DTIC Document, Rapp. tech., 2002.
- [166] S. Mendis, P. Puska, B. Norrving *et al.*, *Global atlas on cardiovascular disease prevention and control*. World Health Organization, 2011.
- [167] J. C. Messenger, S. J. Chen, J. D. Carroll, J. Burchenal, K. Kioussopoulos, et B. M. Groves, “3d coronary reconstruction from routine single-plane coronary angiograms : clinical validation and quantitative analysis of the right coronary artery in 100 patients”, *The International Journal of Cardiac Imaging*, vol. 16, no. 6, pp. 413–427, 2000.
- [168] F. M’hiri, L. Duong, C. Desrosiers, et M. Cheriet, “Vesselwalker : Coronary arteries segmentation using random walks and hessian-based vesselness filter”, dans *Biomedical Imaging (ISBI), 2013 IEEE 10th International Symposium on*. IEEE, 2013, pp. 918–921.
- [169] F. M’hiri, T. Le, L. Duong, C. Desrosiers, et M. Cherief, “Hierarchical segmentation and tracking of coronary arteries in 2d x-ray angiography sequences”, dans *Image Processing (ICIP), 2015 IEEE International Conference on*. IEEE, 2015, pp. 1707–1711.
- [170] F. Michel, M. Bronstein, A. Bronstein, et N. Paragios, “Boosted metric learning for 3d multi-modal deformable registration”, dans *Biomedical Imaging : From Nano to Macro, 2011 IEEE International Symposium on*. IEEE, 2011, pp. 1209–1214.
- [171] S. Mika, B. Schölkopf, A. J. Smola, K.-R. Müller, M. Scholz, et G. Rätsch, “Kernel pca and de-noising in feature spaces.” dans *NIPS*, vol. 11, 1998, pp. 536–542.
- [172] K. Mikolajczyk et C. Schmid, “Scale & affine invariant interest point detectors”, *International journal of computer vision*, vol. 60, no. 1, pp. 63–86, 2004.
- [173] —, “A performance evaluation of local descriptors”, *Pattern Analysis and Machine Intelligence, IEEE Transactions on*, vol. 27, no. 10, pp. 1615–1630, 2005.
- [174] C. A. Miller, L.-Y. Hsu, A. Ta, H. Conn, S. Winkler, et A. E. Arai, “Quantitative pixel-wise measurement of myocardial blood flow : The impact of surface coil-related field inhomogeneity and a comparison of methods for its correction”, *Journal of Cardiovascular Magnetic Resonance*, vol. 17, no. 1, p. 11, 2015.
- [175] J. Milles, R. J. van der Geest, M. Jerosch-Herold, J. H. Reiber, et B. P. Lelieveldt, “Fully

- automated motion correction in first-pass myocardial perfusion mr image sequences”, *Medical Imaging, IEEE Transactions on*, vol. 27, no. 11, pp. 1611–1621, 2008.
- [176] J. S. Milner, J. A. Moore, B. K. Rutt, et D. A. Steinman, “Hemodynamics of human carotid artery bifurcations : computational studies with models reconstructed from magnetic resonance imaging of normal subjects”, *Journal of Vascular Surgery*, vol. 28, no. 1, pp. 143–156, 1998.
- [177] F. Mokhtarian et F. Mohanna, “Performance evaluation of corner detectors using consistency and accuracy measures”, *Computer Vision and Image Understanding*, vol. 102, no. 1, pp. 81–94, 2006.
- [178] K. L. Moore, A. F. Dalley, et A. M. Agur, *Clinically oriented anatomy*. Lippincott Williams & Wilkins, 2013.
- [179] J.-M. Morel et G. Yu, “Asift : A new framework for fully affine invariant image comparison”, *SIAM Journal on Imaging Sciences*, vol. 2, no. 2, pp. 438–469, 2009.
- [180] Y. Nakamura, M. Yashiro, R. Uehara, A. Sadakane, S. Tsuboi, Y. Aoyama, K. Kotani, E.-O. Tsogzolbaatar, et H. Yanagawa, “Epidemiologic features of kawasaki disease in japan : results of the 2009-2010 nationwide survey.” *Journal of epidemiology/Japan Epidemiological Association*, vol. 22, no. 3, pp. 216–221, 2011.
- [181] S. Nakatani, M. Yamagishi, J. Tamai, Y. Goto, T. Umeno, A. Kawaguchi, C. Yutani, et K. Miyatake, “Assessment of coronary artery distensibility by intravascular ultrasound application of simultaneous measurements of luminal area and pressure”, *Circulation*, vol. 91, no. 12, pp. 2904–2910, 1995.
- [182] B. K. Nallamothu, J. A. Spertus, A. J. Lansky, D. J. Cohen, P. G. Jones, F. Kureshi, G. J. Dehmer, J. P. Drozda, M. N. Walsh, J. E. Brush, G. C. Koenig, T. F. Waites, D. S. Gantt, G. Kichura, R. A. Chazal, P. K. O’Brien, C. M. Valentine, J. S. Rumsfeld, J. H. Reiber, J. G. Elmore, R. A. Krumholz, W. D. Weaver, et H. M. Krumholz, “Comparison of clinical interpretation with visual assessment and quantitative coronary angiography in patients undergoing percutaneous coronary intervention in contemporary practice : The assessing angiography (a2) project”, *Circulation*, vol. 127, no. 17, pp. 1793–1800, 2013. DOI : 10.1161/CIRCULATIONAHA.113.001952
- [183] J. W. Newburger, M. Takahashi, A. S. Beiser, J. C. Burns, J. Bastian, K. J. Chung, S. D. Colan, C. E. Duffy, D. R. Fulton, M. P. Glode *et al.*, “A single intravenous infusion

- of gamma globulin as compared with four infusions in the treatment of acute kawasaki syndrome”, *New England Journal of Medicine*, vol. 324, no. 23, pp. 1633–1639, 1991.
- [184] J. W. Newburger, M. Takahashi, M. A. Gerber, M. H. Gewitz, L. Y. Tani, J. C. Burns, S. T. Shulman, A. F. Bolger, P. Ferrieri, R. S. Baltimore *et al.*, “Diagnosis, treatment, and long-term management of kawasaki disease a statement for health professionals from the committee on rheumatic fever, endocarditis and kawasaki disease, council on cardiovascular disease in the young, american heart association”, *Circulation*, vol. 110, no. 17, pp. 2747–2771, 2004.
- [185] L. Nichols, S. Lagana, et A. Parwani, “Coronary artery aneurysm : a review and hypothesis regarding etiology”, *Archives of pathology & laboratory medicine*, vol. 132, no. 5, pp. 823–828, 2008.
- [186] S. Nielles-Vallespin, P. Kellman, L.-Y. Hsu, et A. E. Arai, “Flash proton density imaging for improved surface coil intensity correction in quantitative and semi-quantitative ssfp perfusion cardiovascular magnetic resonance”, *Journal of Cardiovascular Magnetic Resonance*, vol. 17, no. 1, p. 16, 2015.
- [187] Y. Onuma et P. W. Serruys, “Bioresorbable scaffold the advent of a new era in percutaneous coronary and peripheral revascularization?” *Circulation*, vol. 123, no. 7, pp. 779–797, 2011.
- [188] J. M. Orenstein, S. T. Shulman, L. M. Fox, S. C. Baker, M. Takahashi, T. R. Bhatti, P. A. Russo, G. W. Mierau, J. P. de Chadarévian, E. J. Perlman *et al.*, “Three linked vasculopathic processes characterize kawasaki disease : a light and transmission electron microscopic study”, *PloS one*, vol. 7, no. 6, p. e38998, 2012.
- [189] M. M. Orkisz, C. Bresson, I. E. Magnin, O. Champin, et P. C. Douek, “Improved vessel visualization in mr angiography by nonlinear anisotropic filtering”, *Magnetic Resonance in Medicine*, vol. 37, no. 6, pp. 914–919, 1997.
- [190] N. Otsu, “A threshold selection method from gray-level histograms”, *Automatica*, vol. 11, no. 285-296, pp. 23–27, 1975.
- [191] Y. Ou, A. Sotiras, N. Paragios, et C. Davatzikos, “Dramms : Deformable registration via attribute matching and mutual-saliency weighting”, *Medical image analysis*, vol. 15, no. 4, pp. 622–639, 2011.

- [192] N. Paragios, Y. Chen, et O. D. Faugeras, *Handbook of mathematical models in computer vision*, 2006.
- [193] P. Perona, “Steerable-scalable kernels for edge detection and junction analysis”, *Image and Vision Computing*, vol. 10, no. 10, pp. 663–672, 1992.
- [194] N. Petrishchev et I. Mikhailova, “Influence of some hydrodynamic factors of thrombus formation in microvessels”, *Microvascular research*, vol. 49, no. 1, pp. 12–16, 1995.
- [195] K. M. Piehler, T. C. Wong, K. S. Punttil, K. M. Zareba, K. Lin, D. M. Harris, C. R. Deible, J. M. Lacomis, F. Czeyda-Pommersheim, S. C. Cook *et al.*, “Free-breathing, motion-corrected late gadolinium enhancement is robust and extends risk stratification to vulnerable patients”, *Circulation : Cardiovascular Imaging*, vol. 6, no. 3, pp. 423–432, 2013.
- [196] J. P. Pluim, J. A. Maintz, et M. A. Viergever, “Mutual-information-based registration of medical images : a survey”, *Medical Imaging, IEEE Transactions on*, vol. 22, no. 8, pp. 986–1004, 2003.
- [197] T. Pock, M. Urschler, C. Zach, R. Beichel, et H. Bischof, “A duality based algorithm for tv-l 1-optical-flow image registration”, dans *Medical Image Computing and Computer-Assisted Intervention–MICCAI 2007*. Springer, 2007, pp. 511–518.
- [198] J. L. Prince et J. M. Links, *Medical imaging signals and systems*. Pearson Prentice Hall Upper Saddle River, NJ, 2006.
- [199] A. A. Quyyumi, N. Dakak, N. P. Andrews, D. M. Gilligan, J. A. Panza, et R. O. Cannon, “Contribution of nitric oxide to metabolic coronary vasodilation in the human heart”, *Circulation*, vol. 92, no. 3, pp. 320–326, 1995.
- [200] S. Rath, Y. Har-Zahav, A. Battler, O. Agranat, Z. Rotstein, B. Rabinowitz, et H. N. Neufeld, “Fate of nonobstructive aneurysmatic coronary artery disease : angiographic and clinical follow-up report”, *American heart journal*, vol. 109, no. 4, pp. 785–791, 1985.
- [201] M. Rochery, I. H. Jermyn, et J. Zerubia, “Higher order active contours”, *International Journal of Computer Vision*, vol. 69, no. 1, pp. 27–42, 2006.
- [202] X. Rodó, R. Curcoll, M. Robinson, J. Ballester, J. C. Burns, D. R. Cayan, W. I. Lipkin, B. L. Williams, M. Couto-Rodriguez, Y. Nakamura *et al.*, “Tropospheric winds from

- northeastern china carry the etiologic agent of kawasaki disease from its source to japan”, *Proceedings of the National Academy of Sciences*, vol. 111, no. 22, pp. 7952–7957, 2014.
- [203] K. Rohr, H. S. Stiehl, R. Sprengel, T. M. Buzug, J. Weese, et M. Kuhn, “Landmark-based elastic registration using approximating thin-plate splines”, *Medical Imaging, IEEE Transactions on*, vol. 20, no. 6, pp. 526–534, 2001.
- [204] A. H. Rowley, S. C. Baker, J. M. Orenstein, et S. T. Shulman, “Searching for the cause of kawasaki disease—cytoplasmic inclusion bodies provide new insight”, *Nature Reviews Microbiology*, vol. 6, no. 5, pp. 394–401, 2008.
- [205] A. H. Rowley, S. C. Baker, S. T. Shulman, F. L. Garcia, L. M. Fox, I. M. Kos, S. E. Crawford, P. A. Russo, R. Hammadeh, K. Takahashi *et al.*, “Rna-containing cytoplasmic inclusion bodies in ciliated bronchial epithelium months to years after acute kawasaki disease”, *PLoS One*, vol. 3, no. 2, p. e1582, 2008.
- [206] D. Rueckert, L. I. Sonoda, C. Hayes, D. L. Hill, M. O. Leach, et D. J. Hawkes, “Nonrigid registration using free-form deformations : application to breast mr images”, *Medical Imaging, IEEE Transactions on*, vol. 18, no. 8, pp. 712–721, 1999.
- [207] Z. M. Ruggeri, “Mechanisms of shear-induced platelet adhesion and aggregation.” *Thrombosis and haemostasis*, vol. 70, no. 1, p. 119, 1993.
- [208] D. B. Russakoff, T. Rohlfing, J. R. Adler, et C. R. Maurer, “Intensity-based 2d-3d spine image registration incorporating a single fiducial marker 1”, *Academic radiology*, vol. 12, no. 1, pp. 37–50, 2005.
- [209] K. Samada, H. Shiraishi, A. Sato, et M. Y. Momoi, “Grown-up kawasaki disease patients who have giant coronary aneurysms”, *World Journal of Pediatrics*, vol. 6, no. 1, pp. 38–42, 2010.
- [210] Y. Sasaguri et H. Kato, “Regression of aneurysms in kawasaki disease : a pathological study”, *The Journal of pediatrics*, vol. 100, no. 2, pp. 225–231, 1982.
- [211] Y. Sato, S. Nakajima, N. Shiraga, H. Atsumi, S. Yoshida, T. Koller, G. Gerig, et R. Kikinis, “Three-dimensional multi-scale line filter for segmentation and visualization of curvilinear structures in medical images”, *Medical image analysis*, vol. 2, no. 2, pp. 143–168, 1998.

- [212] C. Schmid, R. Mohr, et C. Bauckhage, “Evaluation of interest point detectors”, *International Journal of computer vision*, vol. 37, no. 2, pp. 151–172, 2000.
- [213] M. Schneider et H. Sundar, “Automatic global vessel segmentation and catheter removal using local geometry information and vector field integration”, dans *Biomedical Imaging : From Nano to Macro, 2010 IEEE International Symposium on*. IEEE, 2010, pp. 45–48.
- [214] B. Schölkopf, A. Smola, et K.-R. Müller, “Nonlinear component analysis as a kernel eigenvalue problem”, *Neural computation*, vol. 10, no. 5, pp. 1299–1319, 1998.
- [215] A. D. Scott, J. Keegan, et D. N. Firmin, “Motion in cardiovascular mr imaging 1”, *Radiology*, vol. 250, no. 2, pp. 331–351, 2009.
- [216] T. W. Sederberg et S. R. Parry, “Free-form deformation of solid geometric models”, *ACM SIGGRAPH computer graphics*, vol. 20, no. 4, pp. 151–160, 1986.
- [217] D. Sengupta, A. Kahn, J. Burns, S. Sankaran, S. Shadden, et A. Marsden, “Image-based modeling of hemodynamics in coronary artery aneurysms caused by kawasaki disease”, *Biomechanics and Modeling in Mechanobiology*, vol. 11, no. 6, pp. 915–932, 2012. DOI : 10.1007/s10237-011-0361-8
- [218] P. W. Serruys, J. A. Ormiston, Y. Onuma, E. Regar, N. Gonzalo, H. M. Garcia-Garcia, K. Nieman, N. Bruining, C. Dorange, K. Miquel-Hébert *et al.*, “A bioabsorbable everolimus-eluting coronary stent system (absorb) : 2-year outcomes and results from multiple imaging methods”, *The Lancet*, vol. 373, no. 9667, pp. 897–910, 2009.
- [219] P. W. Serruys, Y. Onuma, H. M. Garcia-Garcia, T. Muramatsu, R.-J. van Geuns, B. de Bruyne, D. Dudek, L. Thuesen, P. C. Smits, B. Chevalier *et al.*, “Dynamics of vessel wall changes following the implantation of the absorb everolimus-eluting bioresorbable vascular scaffold : a multi-imaging modality study at 6, 12, 24 and 36 months.” *EuroIntervention : journal of EuroPCR in collaboration with the Working Group on Interventional Cardiology of the European Society of Cardiology*, vol. 9, no. 11, pp. 1271–1284, 2014.
- [220] J. A. Sethian *et al.*, “Level set methods and fast marching methods”, *Journal of Computing and Information Technology*, vol. 11, no. 1, pp. 1–2, 2003.
- [221] J. A. Sethian, *Level set methods and fast marching methods : evolving interfaces in computational geometry, fluid mechanics, computer vision, and materials science*. Cam-

- bridge university press, 1999, vol. 3.
- [222] D. Shen et C. Davatzikos, “Hammer : hierarchical attribute matching mechanism for elastic registration”, *Medical Imaging, IEEE Transactions on*, vol. 21, no. 11, pp. 1421–1439, 2002.
 - [223] T. Shimazu, M. Hori, M. Mishima, A. Kitabatake, K. Kodama, S. Nanto, et M. Inoue, “Clinical assessment of elastic properties of large coronary arteries : pressure-diameter relationship and dynamic incremental elastic modulus”, *International journal of cardiology*, vol. 13, no. 1, pp. 27–45, 1986.
 - [224] G. Sirimarco, P. Amarenco, J. Labreuche, P.-J. Touboul, M. Alberts, S. Goto, J. Rother, J.-L. Mas, D. L. Bhatt, et P. G. Steg, “Carotid atherosclerosis and risk of subsequent coronary event in outpatients with atherothrombosis”, *Stroke*, vol. 44, no. 2, pp. 373–379, 2013.
 - [225] P. Soille, *Morphological image analysis : principles and applications*. Springer-Verlag New York, Inc., 2003.
 - [226] C. Staelin, “Parameter selection for support vector machines”, *Hewlett-Packard Company, Tech. Rep. HPL-2002-354R1*, 2003.
 - [227] M. B. Stegmann, H. Ólafsdóttir, et H. B. Larsson, “Unsupervised motion-compensation of multi-slice cardiac perfusion mri”, *Medical Image Analysis*, vol. 9, no. 4, pp. 394–410, 2005.
 - [228] C. V. Stewart, C.-L. Tsai, et B. Roysam, “The dual-bootstrap iterative closest point algorithm with application to retinal image registration”, *Medical Imaging, IEEE Transactions on*, vol. 22, no. 11, pp. 1379–1394, 2003.
 - [229] C. Studholme, D. L. Hill, et D. J. Hawkes, “An overlap invariant entropy measure of 3d medical image alignment”, *Pattern recognition*, vol. 32, no. 1, pp. 71–86, 1999.
 - [230] Y. Sun, “Automated identification of vessel contours in coronary arteriograms by an adaptive tracking algorithm”, *Medical Imaging, IEEE Transactions on*, vol. 8, no. 1, pp. 78–88, 1989.
 - [231] H. Sundar, D. Shen, G. Biros, C. Xu, et C. Davatzikos, “Robust computation of mutual information using spatially adaptive meshes”, dans *Medical Image Computing and Computer-Assisted Intervention–MICCAI 2007*. Springer, 2007, pp. 950–958.

- [232] B. Sundaram, R. Kreml, et S. Patel, “Imaging of coronary artery anomalies”, *Radiologic Clinics of North America*, vol. 48, no. 4, pp. 711–727, 2010.
- [233] A. Suzuki, K. Tetsuro, Y. Ono, et Y. Kinoshita, “Thrombolysis in the treatment of patients with kawasaki disease”, *Cardiology in the Young*, vol. 3, no. 03, pp. 207–215, 1993.
- [234] A. Suzuki, M. Yamagishi, K. Kimura, H. Sugiyama, Y. Arakaki, T. Kamiya, et K. Miyatake, “Functional behavior and morphology of the coronary artery wall in patients with kawasaki disease assessed by intravascular ultrasound”, *Journal of the American College of Cardiology*, vol. 27, no. 2, pp. 291–296, 1996.
- [235] M. Taghizadeh Dehkordi, A. M. D. Hoseini, S. Sadri, et H. Soltanianzadeh, “Local feature fitting active contour for segmenting vessels in angiograms”, *Computer Vision, IET*, vol. 8, no. 3, pp. 161–170, 2014.
- [236] A. Tambe, M. Demany, H. A. Zimmerman, et E. Mascarenhas, “Angina pectoris and slow flow velocity of dye in coronary arteries—a new angiographic finding”, *American heart journal*, vol. 84, no. 1, pp. 66–71, 1972.
- [237] H. Tanaka, K. D. Monahan, et D. R. Seals, “Age-predicted maximal heart rate revisited”, *Journal of the American College of Cardiology*, vol. 37, no. 1, pp. 153–156, 2001.
- [238] N. Tanaka, S. Naoe, H. Masuda, et T. Ueno, “Pathological study of sequelae of kawasaki disease (mcls) : with special reference to the heart and coronary arterial lesions”, *Pathology International*, vol. 36, no. 10, pp. 1513–1527, 1986.
- [239] S. Tang, Y. Wang, et Y.-W. Chen, “Application of ica to x-ray coronary digital subtraction angiography”, *Neurocomputing*, vol. 79, pp. 168–172, 2012.
- [240] G. Tarroni, A. R. Patel, F. Veronesi, J. Walter, C. Lamberti, R. M. Lang, V. Mor-Avi, et C. Corsi, “Mri-based quantification of myocardial perfusion at rest and stress using automated frame-by-frame segmentation and non-rigid registration”, dans *Computing in Cardiology, 2010. IEEE*, 2010, pp. 1–4.
- [241] L. Tautz, A. Hennemuth, M. Andersson, A. Seeger, H. Knutsson, et O. Friman, “Phase-based non-rigid registration of myocardial perfusion mri image sequences”, dans *Biomedical Imaging : From Nano to Macro, 2010 IEEE International Symposium on*. IEEE, 2010, pp. 516–519.

- [242] C. A. Taylor et M. T. Draney, “Experimental and computational methods in cardiovascular fluid mechanics”, *Annu. Rev. Fluid Mech.*, vol. 36, pp. 197–231, 2004.
- [243] C. A. Taylor, T. J. Hughes, et C. K. Zarins, “Computational investigations in vascular disease”, *Computers in Physics*, vol. 10, no. 3, pp. 224–232, 1996.
- [244] ———, “Finite element modeling of blood flow in arteries”, *Computer methods in applied mechanics and engineering*, vol. 158, no. 1, pp. 155–196, 1998.
- [245] C. A. Taylor, M. T. Draney, J. P. Ku, D. Parker, B. N. Steele, K. Wang, et C. K. Zarins, “Predictive medicine : computational techniques in therapeutic decision-making”, *Computer aided surgery*, vol. 4, no. 5, pp. 231–247, 1999.
- [246] J.-P. Thirion, “Image matching as a diffusion process : an analogy with maxwell’s demons”, *Medical image analysis*, vol. 2, no. 3, pp. 243–260, 1998.
- [247] R. Toledo, X. Orriols, P. Radeva, X. Binefa, J. Vitria, C. Canero, et J. Villanuev, “Eigensnakes for vessel segmentation in angiography”, dans *Pattern Recognition, 2000. Proceedings. 15th International Conference on*, vol. 4. IEEE, 2000, pp. 340–343.
- [248] A. Torabi, M. Najafianrazavi, et G.-A. Bilodeau, “A comparative evaluation of multi-modal dense stereo correspondence measures”, dans *Robotic and Sensors Environments (ROSE), 2011 IEEE International Symposium on*. IEEE, 2011, pp. 143–148.
- [249] L. Torresani, V. Kolmogorov, et C. Rother, “Feature correspondence via graph matching : Models and global optimization”, dans *Computer Vision–ECCV 2008*. Springer, 2008, pp. 596–609.
- [250] B. Triggs, “Detecting keypoints with stable position, orientation, and scale under illumination changes”, dans *Computer Vision–ECCV 2004*. Springer, 2004, pp. 100–113.
- [251] P. T. Truc, M. A. Khan, Y.-K. Lee, S. Lee, et T.-S. Kim, “Vessel enhancement filter using directional filter bank”, *Computer Vision and Image Understanding*, vol. 113, no. 1, pp. 101–112, 2009.
- [252] C. M. van Bommel, L. J. Spreeuwiers, M. A. Viergever, et W. J. Niessen, “Level-set-based artery-vein separation in blood pool agent ce-mr angiograms”, *Medical Imaging, IEEE Transactions on*, vol. 22, no. 10, pp. 1224–1234, 2003.
- [253] P. A. Van den Elsen, E.-J. D. Pol, et M. A. Viergever, “Medical image matching-a review with classification”, *Engineering in Medicine and Biology Magazine, IEEE*,

- vol. 12, no. 1, pp. 26–39, 1993.
- [254] L. J. Van Vliet, I. T. Young, et P. W. Verbeek, “Recursive gaussian derivative filters”, dans *Pattern Recognition, 1998. Proceedings. Fourteenth International Conference on*, vol. 1. IEEE, 1998, pp. 509–514.
 - [255] P. Viola et W. M. Wells III, “Alignment by maximization of mutual information”, *International journal of computer vision*, vol. 24, no. 2, pp. 137–154, 1997.
 - [256] R. Virmani, M. Robinowitz, J. B. Atkinson, M. B. Forman, M. D. Silver, et H. A. McAllister, “Acquired coronary arterial aneurysms : an autopsy study of 52 patients”, *Human pathology*, vol. 17, no. 6, pp. 575–583, 1986.
 - [257] C. Wachinger et N. Navab, “Entropy and laplacian images : Structural representations for multi-modal registration”, *Medical Image Analysis*, vol. 16, no. 1, pp. 1–17, 2012.
 - [258] Q. Wang, “Kernel principal component analysis and its applications in face recognition and active shape models”, *arXiv preprint arXiv :1207.3538*, 2012.
 - [259] S. Wang, B. Li, et S. Zhou, “A segmentation method of coronary angiograms based on multi-scale filtering and region-growing”, dans *Biomedical Engineering and Biotechnology (iCBEB), 2012 International Conference on*. IEEE, 2012, pp. 678–681.
 - [260] J. Weickert, “Coherence-enhancing diffusion filtering”, *International Journal of Computer Vision*, vol. 31, no. 2-3, pp. 111–127, 1999.
 - [261] P. Weinzaepfel, J. Revaud, Z. Harchaoui, et C. Schmid, “DeepFlow : Large displacement optical flow with deep matching”, dans *IEEE Intenational Conference on Computer Vision (ICCV)*, Sydney, Australia, Déc. 2013. En ligne : <http://hal.inria.fr/hal-00873592>
 - [262] W. M. Wells, P. Viola, H. Atsumi, S. Nakajima, et R. Kikinis, “Multi-modal volume registration by maximization of mutual information”, *Medical image analysis*, vol. 1, no. 1, pp. 35–51, 1996.
 - [263] J. West, J. M. Fitzpatrick, M. Y. Wang, B. M. Dawant, C. R. Maurer Jr, R. M. Kessler, R. J. Maciunas, C. Barillot, D. Lemoine, A. Collignon *et al.*, “Comparison and evaluation of retrospective intermodality brain image registration techniques”, *Journal of computer assisted tomography*, vol. 21, no. 4, pp. 554–568, 1997.

- [264] N. M. Wilke, M. Jerosch-Herold, A. Zenovich, et A. E. Stillman, “Magnetic resonance first-pass myocardial perfusion imaging : Clinical validation and future applications”, *Journal of Magnetic Resonance Imaging*, vol. 10, no. 5, pp. 676–685, 1999.
- [265] D. B. Williams et V. Madisetti, *Digital signal processing handbook*. CRC Press, 1999.
- [266] G. Wollny, P. Kellman, A. Santos, et M. J. Ledesma-Carbayo, “Automatic motion compensation of free breathing acquired myocardial perfusion data by using independent component analysis”, *Medical image analysis*, vol. 16, no. 5, pp. 1015–1028, 2012.
- [267] K. Wong, E. Wu, M. Ng, Y. Wu, H. Tse, C. Lau, G. Lo, et E. Yang, “Image registration in myocardial perfusion mri”, dans *Engineering in Medicine and Biology Society, 2005. IEEE-EMBS 2005. 27th Annual International Conference of the*. IEEE, 2006, pp. 453–454.
- [268] N. D. Wong, “Epidemiological studies of chd and the evolution of preventive cardiology”, *Nature Reviews Cardiology*, 2014.
- [269] M. Xia et B. Liu, “Image registration by" super-curves"”, *Image Processing, IEEE Transactions on*, vol. 13, no. 5, pp. 720–732, 2004.
- [270] C. Xu, D. L. Pham, et J. L. Prince, “Image segmentation using deformable models”, *Handbook of medical imaging*, vol. 2, pp. 129–174, 2000.
- [271] Y. Xu, H. Zhang, H. Li, et G. Hu, “An improved algorithm for vessel centerline tracking in coronary angiograms”, *Computer methods and programs in biomedicine*, vol. 88, no. 2, pp. 131–143, 2007.
- [272] H. Xue, S. Zuehlsdorff, P. Kellman, A. Arai, S. Nielles-Vallespin, C. Cheddhote, C. H. Lorenz, et J. Guehring, “Unsupervised inline analysis of cardiac perfusion mri”, dans *Medical Image Computing and Computer-Assisted Intervention–MICCAI 2009*. Springer, 2009, pp. 741–749.
- [273] Z. Xue, D. Shen, et C. Davatzikos, “Determining correspondence in 3-d mr brain images using attribute vectors as morphological signatures of voxels”, *Medical Imaging, IEEE Transactions on*, vol. 23, no. 10, pp. 1276–1291, 2004.
- [274] R. Yamakawa, M. Ishii, T. Sugimura, T. Akagi, G. Eto, M. Iemura, T. Tsutsumi, et H. Kato, “Coronary endothelial dysfunction after kawasaki disease : Evaluation by intracoronary injection of acetylcholine 1”, *Journal of the American College of Cardiology*, vol. 31, no. 5, pp. 1074–1080, 1998.

- [275] M. Yanagisawa, N. Kobayashi, et S. Matsuya, “Myocardial infarction due to coronary thromboarteritis, following acute febrile mucocutaneous lymph node syndrome (mlns) in an infant”, *Pediatrics*, vol. 54, no. 3, pp. 277–281, 1974.
- [276] D. Yang, H. Li, D. A. Low, J. O. Deasy, et I. El Naqa, “A fast inverse consistent deformable image registration method based on symmetric optical flow computation”, *Physics in medicine and biology*, vol. 53, no. 21, p. 6143, 2008.
- [277] J. Yang, S. Ma, W. Tan, Q. Sun, P. P Cao, et D. Zhao, “Mra fuzzy c-means vessel segmentation algorithm based on tubular structure”, *Journal of Medical Imaging and Health Informatics*, vol. 5, no. 8, pp. 1853–1858, 2015.
- [278] X. Yang, Z. Xue, X. Liu, et D. Xiong, “Topology preservation evaluation of compact-support radial basis functions for image registration”, *Pattern Recognition Letters*, vol. 32, no. 8, pp. 1162–1177, 2011.
- [279] M. S. Yasein et P. Agathoklis, “A feature-based image registration technique for images of different scale”, dans *Circuits and Systems, 2008. ISCAS 2008. IEEE International Symposium on*. IEEE, 2008, pp. 3558–3561.
- [280] I. T. Young et L. J. van Vliet, “Recursive implementation of the gaussian filter”, *Signal processing*, vol. 44, no. 2, pp. 139–151, 1995.
- [281] L. Zagorchev et A. Goshtasby, “A comparative study of transformation functions for nonrigid image registration”, *Image Processing, IEEE Transactions on*, vol. 15, no. 3, pp. 529–538, 2006.
- [282] N. Zarinabad, A. Chiribiri, G. L. Hautvast, M. Ishida, A. Schuster, Z. Cvetkovic, P. G. Batchelor, et E. Nagel, “Voxel-wise quantification of myocardial perfusion by cardiac magnetic resonance. feasibility and methods comparison”, *Magnetic resonance in medicine*, vol. 68, no. 6, pp. 1994–2004, 2012.
- [283] N. Zarinabad, A. Chiribiri, et M. Breeuwer, “Myocardial blood flow quantification from mri—an image analysis perspective”, *Current Cardiovascular Imaging Reports*, vol. 7, no. 1, pp. 1–9, 2014.
- [284] B. Zitova et J. Flusser, “Image registration methods : a survey”, *Image and vision computing*, vol. 21, no. 11, pp. 977–1000, 2003.